DESIGN AND CONTROL OF A MICRO/NANO LOAD STAGE FOR IN-SITU AFM

OBSERVATION AND NANOSCALE STRUCTURAL AND MECHANICAL

CHARACTERIZATION OF MWCNT-EPOXY COMPOSITES

A Thesis
Submitted to the Graduate Faculty
of the
North Dakota State University
of Agriculture and Applied Science

By

Wyatt Christopher Leininger

In Partial Fulfillment of the Requirements
for the Degree of
MASTER OF SCIENCE

Major Department:
Mechanical Engineering

December 2016

Fargo, North Dakota

North Dakota State University
Graduate School

Title

DESIGN AND CONTROL OF A MICRO/NANO LOAD STAGE FOR IN-SITU
AFM OBERVATION AND NANOSCALE STRUCTURAL AND
MECHANICAL CHARACTERIZATION OF MWCNT-EPOXY COMPOSITES

By

Wyatt Leininger

The Supervisory Committee certifies that this ***disquisition*** complies with North Dakota

State University's regulations and meets the accepted standards for the degree of

MASTER OF SCIENCE

SUPERVISORY COMMITTEE:

Dr. Annie Tangpong

Chair

Dr. Xinnan Wang

Dr. Majura Selekwa

Dr. Kambiz Farahmand

Approved:

11/17/17	Dr. Alan R. Kallmeyer
Date	Department Chair

ABSTRACT

Nanomaterial composites hold improvement potential for many materials. Improvements arise through known material behaviors and unique nanoscale effects to improve performance in areas including elastic modulus and damping as well as various processes, and products. Review of research spurred development of a load-stage. The load stage could be used independently, or in conjunction with an AFM to investigate bulk and nanoscale material mechanics.

The effect of MWCNT content on structural damping, elastic modulus, toughness, loss modulus, and glass transition temperature was investigated using the load stage, AMF, and DMA. Initial investigation showed elastic modulus increased 23% with 1wt.% MWCNT versus pure epoxy and *in-situ* imaging observed micro/nanoscale deformation.

Dynamic capabilities of the load stage were investigated as a method to achieve higher stress than available through DMA. The system showed energy dissipation across all reinforce levels, with ~480% peak for the 1wt.% MWCNT material vs. the neat epoxy at 1Hz.

Keywords

ACKNOWLEDGMENTS

I would like to thank my wife for all of her support and encouragement throughout graduate school. Without her I would not have started this path or completed it.

My advisors, Dr. Tangpong and Dr. Wang, for all that they have taught me about research, engineering, and life. Committee members, Dr. Selekwa and Dr. Farahmand, for their guidance and support. All of you challenged me, to look into the details, to do better, and see that there is more than one path.

Thank you to all of the faculty and staff in the mechanical engineering department. You do your jobs well, taught me much, and helped me navigate the challenges of higher education.

There are many more that I will not list, but you know who you are, family, friends, and co-workers.

To all of those in my life, whether you provided encouragement to keep going, support when it was lacking, suggestions when I hit a wall, or just a listening ear when I was trying to puzzle out an answer, your contributions are appreciated. Thank you for your help!

TABLE OF CONTENTS

LIST OF TABLES

LIST OF FIGURES

LIST OF ABBREVIATIONS

3D...Three dimensional

AFM...Atomic Force Microscope

CNT..Carbon nanotube

DAQ...Data acquisition system

DC..Direct current

DMA ....Dynamic mechanical analysis

ISS..Interfacial shear stress

MWCNT ....Multi-walled carbon nanotube

RPM ....Revolutions per minute

SEM ....Scanning electron microscope

SWCNT..Single-walled carbon nanotube

THF...Tetrahydrofuran

TEM ....transmission electron microscopy

UI ....User interface

UTS..Ultimate tensile strength

WAXD ....wide angle x-ray diffraction

LIST OF SYMBOLS

α ....Fiber aspect ratio

u_t...Strain energy at failure

ε...Strain

ε_{fiber} ....Strain of the fiber

ε_f...Strain at failure

ξ...Halpin-Tsai shape factor

η...Halpin-Tsai elastic modulus factor

η_1...Screw efficiency

σ...Stress

σ_f...Fiber ultimate strength

σ_{fmax} ....Maximum stress generated within the fiber

σ_m...Matrix tensile strength

τ...Interfacial shear strength

υ...Poisson's ratio

A ....Cross-sectional area of the fiber

D_o ....Fiber outer diameter

D_i...Fiber inner diameter

E ....Elastic modulus

E_{11} ....Elastic modulus of an aligned fiber composite, stressed in alignment with the fibers

E_{22} ....Elastic modulus of an aligned fiber composite, stressed transverse to the fibers

xiv

E_c ....Elastic modulus of a composite with randomly aligned reinforcement

E_f ....Elastic modulus of the fiber

E_m ....Elastic modulus of the matrix

F_a ....Linear force generated by the lead screw

P_h ....Screw lead (distance traveled in one revolution)

T ....Torque

T_g ....Glass transition temperature

V_f ....Volume fraction of fiber in the composite

V_{fo} ....Volume fraction of fiber outer layers in the composite

V_o ....Volume of an MWCNT fibers outer layer

V_T ....Volume of a CNT fiber

d_f ....Diameter of the reinforcement fiber

g ....Hui-Shia geometry-dependent factor of the modeled inclusion

l ....Length of the reinforcement fiber

l_c ....Critical fiber length

1. INTRODUCTION

Nanomaterial composites hold improvement potential for many engineering materials. These improvements arise through a combination of known material behaviors and unique nanoscale effects to provide improved performance and new design functionality. To best utilize these nanoscale effects, they must be understood. Investigation of nanoscale mechanics poses challenges, however. Due to their small size, observation methods for nanomaterial composites are limited, even more so for observation of materials under stress. To facilitate *in-situ* observation of materials at the nanoscale a load stage was designed and built for use with an atomic force microscope (AFM). The following sections in this chapter will introduce how nanomaterial composites improve material performance and functionality through their use, including details on why these materials and their application hold such interest. Important applications will be highlighted, and specific questions for investigation will be presented. This body of information forms the background and motivation for the research. Relevant findings from related research will be reviewed. Details of the current work are outlined in the final section of this chapter.

1.1. Background and Motivation

Engineering advances create new possibilities every day, leading to ever more features and functions vying for inclusion in any given product. Miniaturization, in particular, has opened up many of these new opportunities, especially in the area of nanomaterials. Prospects exist to improve various processes, products, and material such as: nanoscale manufacturing [1], unique nanoscale effects such as giant magnetoresistance [2], increased data storage densities [1-3], and the growing multitude of handheld electronics hitting the market every day [3, 4].

Thanks to miniaturization, more and more of the features these engineering advances create are finding a place in designs. As the parts grow smaller and the supporting structure is hollowed out and optimized to make more room, the safety factor tends to go down. The result is that with a reduced safety factor the structure has less tolerance for vibratory and unexpected stresses. Because of this trend, damping, dissipation of mechanical energy from vibration or impact has particular importance across many products from cellphones to skyscrapers. Applications where damping is important include noise reduction [5], crash/impact protection [6, 7], isolation of sensitive components from nearby excitation sources (such as the rotor vibration of a helicopter [8]), vehicle suspension systems [9], and nanoscale position devices [1, 7]. By dissipating the incoming energy, vibration transfer and peak stresses are reduced, thus restoring some of the safety factor lost due to material removal and protecting nearby components. Methods of increasing system damping vary based on several factors. Selection of a damping method is typically dependent on application requirements. Common factors include, but are not limited to: system size, cost, vibration amplitude, and frequency.

In large stationary systems, such as buildings [10] and wind towers [11], the damping requirement for structural stability often favors implementation methods where damping is provided by a dedicated subsystem, such as a tuned mass damper [10]. A tuned mass damper, also known as a harmonic absorber or active mass damper, is a device mounted within a structure to prevent discomfort, damage, or outright structural failure caused by vibration [12]. One common application is in high rise buildings to reduce sway from wind and reduce the chance of building damage or failure during an earthquake. These dedicated systems tend to be costly, both monetarily and in terms of the total system mass and volume, by adding structural support requirements and reducing usable space. Smaller products, such as handheld electronics,

do not have sufficient space available for inclusion of a dedicated damping subsystem, so other methods are required.

Adding damping onto a structure is another method employed that offers a lower volume and mass option than a dedicated sub system. One such method is the application of viscoelastic tape to structural members [13]. Viscoelastic tape unfortunately poses some alternate problems. For example, the tape's tendency to de-bond from the structural member it is damping, thus the loss of the added damping [14]. Maximizing the utilization of available mass and volume in any given system calls for a different solution than the methods discussed above. The ideal solution would be to incorporate damping into components that are already part of the system. For best results the damping would need to be incorporated without penalty to the material's other properties.

A potential route for incorporation of damping within a common structural material is through the addition of reinforcement materials into a base polymer. Polymers are widely used in industry and present the potential for improvement of their mechanical properties, such as polymers generally low toughness [6] and damping characteristics. Transitioning polymer components to components made from polymer based composites offers a simple and direct route for incorporating properties of the composite reinforcement into the base polymer. The resulting composite will take on properties of both the polymer and reinforcement materials and, in some cases, new properties not present in either material alone. With proper selection, the resulting composite would gain a desired property improvement while maintaining the integrity of the original material it was replacing. One such pairing showing significant improvement potential is the addition of carbon nanotubes (CNTs) to a variety of polymer bases.

CNT polymer composites have been shown to exhibit improved energy dissipation [6, 14-18] versus unreinforced polymers, thereby providing a way to incorporate additional damping into structural members of a systems. Direct incorporation of damping improvement offers distinct advantages over the previously discussed methods for applications where system size and/or weight is a primary concern, as long as the initial properties of the initial material are maintained. This makes polymers an excellent target for damping incorporation. Damping, however, is commonly investigated independently of the material's quasi-static properties [16-21], such as elastic modulus and tensile strength. The disconnection between data on a material's damping and quasi-static properties makes it difficult to readily integrate the two functions. To effectively integrate dual functionality, improved damping, and existing structural functions into a single component, data from both testing routes must to be considered together.

Unfortunately, while experimental results from CNT-polymer composites show some performance improvement for properties such as elastic modulus [22, 23] and intrinsic damping; these composites do not achieve their performance potential [24]. This shortfall is particularly notable for low strain amplitudes where energy dissipation remains near that of the unreinforced polymer [14]. Thus, it is desirable to improve the actual performance of these composites to closer match their potential. A better understanding of the nanoscale mechanics driving the polymer composite properties, such as how the composite constituents interact and deform, should provide insight that can be applied to reduce the gap between experimental and theoretical performance. To improve this understanding, testing and observation using the developed load stage and AFM were used to investigate quasi-static and damping properties as well as investigation of nanoscale mechanics. A review of previous research in this area was used to support and direct the experimental work. The following literature review focuses on

4

polymer composite research and the potential improvement to damping capabilities these materials offer.

1.2.   Literature Review

A review of existing research was conducted as part of this research. This answered questions where data was available, provided background for comparative checks, and provided focus for the unanswered questions. The review starts with a broad background on CNTs and CNT-polymer composites. The board view provides the basis for a detailed look at several existing quasi-static material models and research regarding damping properties of CNT-polymer composites. The final section covers testing methods used in previous publications, as well as the pros and cons of these methods.

1.2.1.   Introduction to CNTs and CNT-Polymer Composites

Polymers provide a combination of established usage and specific property improvement targets needed to expand functionality. This combination of usage and potential makes them a compelling choice for composite matrices [17, 25-29]. Another factor relevant to many products is total mass, as mentioned previously. Resulting component mass is an area where polymers perform well as typical solid polymer densities are between 1 and 2 g/cm^3 [30], compared to 2.8 g/cm^3 and 7.8 g/cm^3 typical of aluminum alloys and iron alloys respectively. The range of potential fillers effect on component mass is even broader as the upper limit of solid material densities exceeds 20 g/cm^3 [31]. Polymers also offer design flexibility through injection molding and other manufacturing methods that facilitate creation of complex geometry. These factors make polymers an excellent choice for use as a composite matrix material.

CNTs are a desirable reinforcement fiber because of their exceptional properties. The tensile strength and elastic modulus have reported values exceeding 60 GPa (8.7 Mpsi) and

5

910 GPa (132 Mpsi) respectively [32, 33]; though it has been shown that the elastic modulus is affected by the nanotube diameter [34] and manufacturing processes [35]. CNTs have a density similar to that of polymers, 2.1 g/cm^3 reported by the manufacturer of the MWCNTs used in this work [36] and 1.3 g/cm^3 reported for a typical single-walled CNT nanorope [34]. This limits the potential material density increase when adding CNTs as the filler in polymer composites, allowing for more flexibility in applications, particularly in products where mass is a primary concern. Composites made using nanoreinforcements as the filler have been shown to outperform micro and macro scale reinforced composites [29, 37], further supporting the use of CNTs as a composite reinforcement. Typical nanoreinforced composites contain 1-3 wt.% reinforcement, though they can contain 10 wt.% or more [6, 14, 16, 38].

Another beneficial property of CNTs is that the structure of an individual CNT layer has been shown to be resistant to defects in the lattice structure [39]. This resistance to defects provides added uniformity and consistency of properties to structures in which it is used. Multi-wall CNTs (MWCNTs) introduce some variability into the properties and effectiveness relative to single walled CNTs (SWCNTs) in exchange for additional properties not found in single walled CNTs. One of the limitations of MWCNTs, for example, is the load transfer between layers. Inter-layer load transfer is reduced in MWCNTs relative to SWCNTs which results in a reduction to the volume of reinforcement that is actually benefiting the composite. Research shows that the inner layers of MWCNT have limited tensile load bearing capabilities [33, 39-41]. This limitation is due to the nature of the interactions between tube layers. The interwall distance is 0.34 nm [32, 34], comparable to the spacing of graphene layers. The limited defect nature of CNT layers causes there to be minimal physical layer interlocking affecting layer-to-layer force transfer [39]. Interactions between layers are predominantly Van der Waals forces [33, 34, 39,

42] which provide weak shear transfer. The best example for quantifying the limited nature of the interlayer force transfer, is work by Cumings and Zettl demonstrating the potential application of MWCNTs as nanoscale bearings [43]. Direct application, such as bonding the test probe to the desired layer at the MWCNTs open end, was found to be the only effective method of tensile force transfer to the inner layers [33]. The ability to transfer load to the ends of innerlayer tubes in compression likely contributes to the increased compressive strength of MWCNTs, reportedly 100-150 GPa [32, 44], when compared to SWCNTs.

Selection of an appropriate matrix-filler combination is important to achieve the desired performance characteristics of the composite, from the class of polymer all the way down to the type of CNT, the manufacturing processes used, and the method used to mix the components. Several factors affect the performance of CNT-polymer composites. These include reinforcement dispersion [14, 16, 24], aspect ratio [14, 24] and interfacial characteristics such as bonding strength [16, 24, 45] and surface area [16, 45]. Some relationships, such as surface area, appear straightforward; increased fiber surface area means increased shear interface area and increased load transfer. Other factors such as dispersion and aspect ratio are more complex in implementation, as increasing one tends to reduce the other. The tendency for ultrasonic mixing to break CNTs while helping to disperse them [46, 47] illustrates this factor well. Conversely, higher CNT aspect ratio coincides with increased clumping, thus poorer dispersion [46-48].

Filler dispersion possesses a significant challenge as the scale of CNTs predisposes them to clumping [38, 49, 50], which makes them difficult to separate. Consequently, SWCNTs, which are smaller in diameter than MWCNTs, have shown the greatest dispersion difficulty. SWCNTs have a strong tendency to group up, forming ropelike bundles that are difficult to

disperse [38, 45]. Dispersion methods are primarily split between mechanical shear processing

and chemical solution processing [24, 27]. Unfortunately, each method has its penalties.

Chemical dispersion, for example, requires multiple additional steps. These multiple

steps begin with dissolving the CNTs in a solvent such as Tetrahydrofuran (THF), occasionally

facilitated by ultrasonication. Next a component of the matrix polymer must be brought into the

suspension. Finally, the solvent must be removed, which is commonly done via evaporation or

use of an additional chemical to precipitate the CNT-polymer mixture [18, 35, 38, 50, 51]. All

these additional steps can lead to greater error as well as incurring continual cost for chemical

purchasing or recovery, handling, and disposal requirements of the process components.

Mechanical shear processing, on the other hand, requires a greater starting investment for

equipment, but offers faster processing potential and lower operational costs as there are few, or

no, consumable components. The penalty of shear processes, such as shear melt mixing or

ultrasonication, is the CNT breakage that these processes cause [46, 47, 52, 53], thereby

lowering the filler's aspect ratio. Each mode of dispersion offers a unique set of pros and cons

for feasibility and their effect on aspect ratio, without providing a clearly superior option.

The effects of aspect ratio are illustrated by experimental comparison of polycarbonate

reinforced with two similar carbon structures varying only in aspect ratio. Comparison of

polycarbonate samples reinforced with SWCNT or spherical fullerenes composed of C_{60}, showed

that aspect ratio plays a significant role in damping [14]. The spherical particles were ineffective

as the 1 wt.% fullerene reinforced material showed negligible improvement over the neat

polycarbonate. The 1 wt.% SWCNT material demonstrated improvement in loss modulus at

strain greater than 0.1%, and greater than 300% improvement in loss modulus when material

strain exceeded 0.75%. Odegard et al. [23] showed through their work with equivalent

continuum modeling that nanotube length, and thereby aspect ratio, had a direct correlation with

the elastic modulus. They also found that increased fiber aspect ratio resulted in an increasingly

linear relationship between weight percentage reinforcement and the longitudinal elastic modulus

for an aligned fiber composite [23]. The experimental results for this study followed the same

trends. They did not, however, perform as well as the models predicted [23]. The Halpin-Tsai

model, which is discussed in greater detail in section 1.2.2, indicates that the composite's elastic

modulus and tensile strength initially increase sharply with fiber aspect ratio before an eventual

plateau [35] as shown in Figure 1. The calculations are for a theoretical composite with 5 vol.%

reinforcement, matrix elastic modulus of 1 GPa and fiber elastic modulus of 1000 GPa.
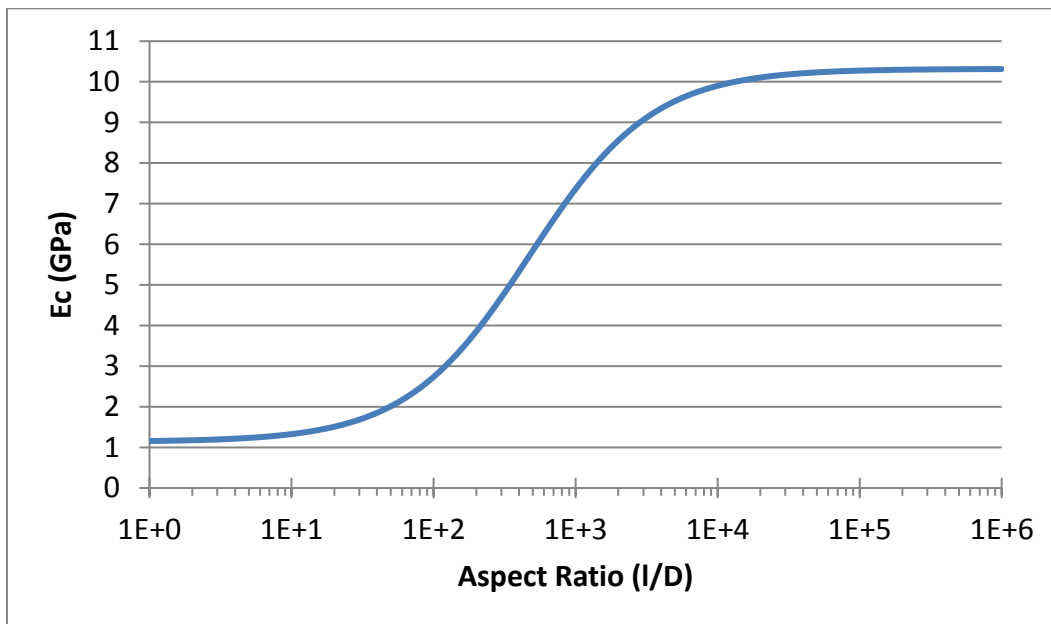
Figure 1. Effects of fiber aspect ratio on composite elastic modulus as estimated using the
Halpin-Tsai model.

The effect of interfacial shear strength (ISS) on quasi-static properties, such as tensile

strength and elastic modulus, was also significant in the SWCNT versus fullerenes research. The

result showed that increased ISS transferred loading to the reinforcement fibers more efficiently,

thus increasing the effects of the reinforcement particles on the quasi-static composite

properties [16, 38, 54]. Research has also shown that under the appropriate conditions, sufficient

bonding can be achieved to cause failure within the surrounding matrix rather than separation at

the polymer-CNT interface [38, 54].

The ISS's effect on composite performance can be shown via the concept of effective

fiber length [38], which estimates the length of the fiber capable of achieving maximum load

transfer. The efficiency of a fiber's reinforcement effect was first examined by Cox [55] who

showed that the fiber's effect on the composites elastic modulus was dependent upon the fiber's

length. To load a fiber, force must be transferred to the fiber through interfacial shear. The force

peaks at the midpoint of the fiber, assuming constant ISS along a straight fiber. There will be a

critical length, l_c, above which sufficient force can be transferred to break the fiber. This critical

length can be calculated [56] by

$$l_c = \frac{\sigma_f D}{2\tau}\left[1 - \frac{D_i^2}{D_o^2}\right]$$ (1)

where σ_f is the fiber's ultimate strength, τ is the interfacial shear strength, D_o is the fiber's outer

diameter and D_i is the fiber's inner diameter. This relationship shows that the ISS is inversely

proportional to the critical length, thus for low shear strengths the length required for a fiber to

reach its maximum potential would be very long. By this relationship, the inner layers of

MWCNTs or inner members of SWCNT ropes, would have an extremely high critical length due

to the weak ISS between SWCNTs. This agrees with the lack of interlayer force transfer during

tensile loading. Additionally, the maximum attainable fiber stress is often less than the fiber

strength due to limitations posed by matrix strain and tensile strength [38]. The effective fiber

length theory expresses this relationship as

$$\sigma_{fmax} = E_f \varepsilon_f \le E_f \frac{\sigma_m}{E_m} \tag{2}$$

where σ_{fmax} is the maximum stress attained within the fiber, σ_m is the matrix tensile strength and E_f and E_m are the fiber and matrix elastic modulus, respectively. This concept, illustrated in Figure 2, shows that as the length of the fiber increases, so does the peak force/stress, until a maximum transfer length is reached. Once this critical length is reached the peak transfer then remains constant as the fiber length increases.
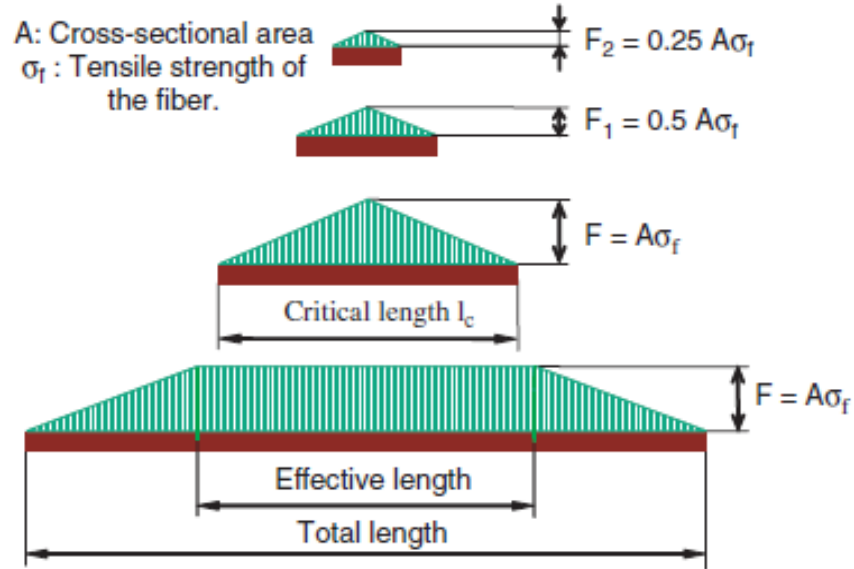
Figure 2. Illustration of the effective fiber length concept and of the relationship between fiber length and load bearing capability. Reproduced from [38].

1.2.2. Quasi-static Material Property Models

CNT reinforced polymer composites exhibit improved structural properties, such as elastic modulus [27, 35, 45, 49], tensile strength [35, 37, 49] and toughness [35, 49]. There are numerous theoretical models focused on estimating the elastic modulus of composites including the Halpin-Tsai, Mori-Tanaka, and Hui-Shia models [23, 57-62].

11

Many of these methods are based on estimating the elastic moduli of a uniaxially aligned fiber composite. The simplification of the system to have uniaxial alignment reduces the mathematical complexity of the modeling. Once the aligned and transverse moduli are estimated, they can be used to form an estimate for a randomly aligned fiber composite. The method of estimation is derived by modeling the randomly oriented composite as a combination of many uniaxially aligned laminate layers, similar to a sheet of plywood. The symmetry of a nanotube simplifies this conceptualization to a 0° to 90° rotation of the tube about a transverse axis. The percentage distribution for how a set of randomly aligned fibers correlated with the 0° to 90° rotational symmetry had to be determined to utilize the symmetry simplification. Finally, the estimation was further simplified by splitting the loads applied to the fibers to the 0° (aligned) and 90° (transverse) components. The result being an equation for the estimation of the elastic modulus of a randomly alignment fiber composite based only on the aligned and transverse elastic moduli of an aligned fiber composite made of the same materials [38].

$$E_c = 0.184E_{11} + 0.816E_{22} \qquad\qquad (3)$$

Where E_c is the elastic modulus of the randomly aligned composite, and E_{11} and E_{22} are respectively, the aligned and transverse elastic moduli of the aligned fiber composite.

The Halpin-Tsai model [35, 38, 45, 57, 58] is one of the aligned fiber models discussed briefly in the previous section. It can be used to estimate E_{11} and E_{22} from the fiber and matrix elastic moduli (E_f and E_m), the volume fraction of fiber in the composite (V_f), and lastly the length (l) and diameter (d) of the fiber.

$$E_{xx} = E_m \frac{1 + \xi_{xx}\eta_{xx}V_f}{1 - \eta_{xx}V_f} \tag{4}$$

$$\eta_{xx} = \frac{(E_f/E_m) - 1}{(E_f/E_m) + \xi_{xx}} \tag{5}$$

$$\xi_{11} = 2\frac{l}{d} \tag{6}$$

$$\xi_{22} = 2 \tag{7}$$

The model was derived beginning with Hill's work [63, 64] solving the stiffness tensor

for the case of a composite modeled as a cylinder embedded with aligned continuous cylindrical

fibers (Figure 3). Each of these materials were assumed to be homogeneous as well as elastically

isotropic in the transverse orientation about the fiber direction [58]. Work done by J J

Hermans [65] advanced the model by solving the relationships between the parameters of Hill's

notation based on a separate set of elastic constants for the fiber and the matrix. Alternatively,

the derivation of the Halpin-Tsai equations can be shown to be an approximate form of

Kerner's [66] spherically reinforced composite modeling work. Work by Hill [63, 64] deriving

relationships for the aligned elastic modulus (E_{11}) and Poisson ratio (v_{12}) was also used in the

development of the Halpin-Tsai model equations.
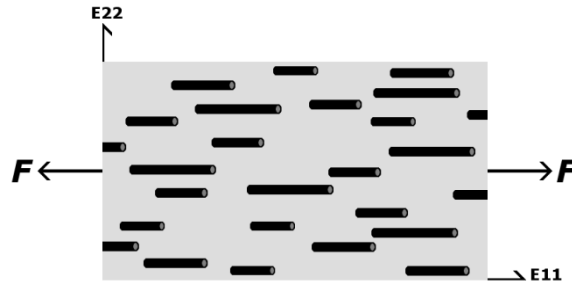
Figure 3. Representation of aligned fibers in matrix used in the derivation of the Halpin-Tsai model. Reprinted with permission [67].

1.2.3. Damping Properties

CNT polymer composites exhibit improved mechanical energy dissipation [6, 14-18] which has potential benefits across applications including noise reduction [5], nanopositioning [1, 7], and many others [6-9]. Experimental evidence indicates the energy dissipation is caused by the stick-slip mechanic that occurs at the CNT-polymer interface [17, 18, 20, 68, 69]. The energy dissipation is affected by properties including the interfacial shear strength [70], fiber aspect ratio [35], and fiber dispersion [14, 16]. The energy dissipation is further influenced by the fact that interfacial slip does not activate uniformly for all interfaces at a given bulk material stress level [18, 20, 68, 71] due to factors including orientation and ISS variation. Therefore, damping continues to be important in product design and development.

The composite's ISS generally exhibits a direct correlation with polymer-CNT composite damping [70] properties. Modeling work by Savvas et al [70] , summarized in Figure 4, found that loss factor increased with ISS while ISS was below the matrix shear stress. The loss factor plateaued when the ISS exceeded the matrix shear strength, and eventually dropped as the ISS went to infinity. The model indicated that a composite with infinite ISS would have a lower loss factor tan the neat polymer. This result was logical based on the lack of interfacial slip to dissipate energy in such a composite, combined with the increased stiffness of the composite

compared to the neat polymer. Their modeling work also indicated that increased CNT waviness

negatively affected the composites loss factor [70].

It has been suggested that a reduction of the material storage modulus during dynamic

testing indicates activation of the interfacial slip, as the fiber then carries less of the elastic

loading [18]. There are several factors that can alter the activation stress by influencing the

effective ISS of the CNT-polymer composite. These factors include
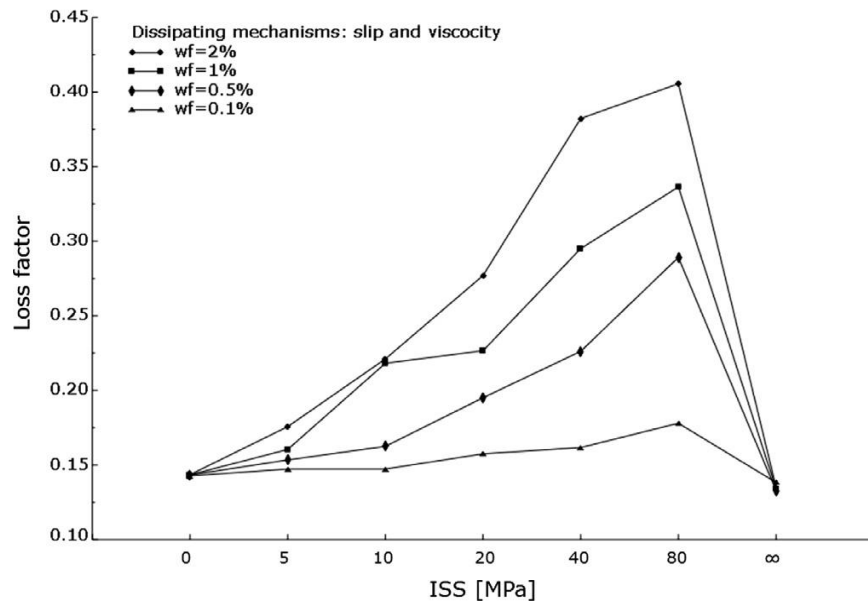
Figure 4. Loss factor computed from the hysteresis loops of CNT reinforced composite representative volume elements considering linear viscoelastic polymer for weight filler = 2, 1, 0.5, 0.1% and ISS = 0, 5, 10, 20, 40, 80 and 1MPa. The polymer shear strength used by the model was 52 MPA. Reproduced from [70].

functionalization [35, 41, 70], CNT dispersion [18, 68], and tube diameter [45, 49, 72]. Some of

the chemical treatments used to functionalize the CNTs surface have been shown to damage the

CNT structure resulting in reduced mechanical performance [46]. Dispersion affected the system

load transfer in part because a portion of the CNT-polymer interfacial area was lost to weaker

CNT-CNT interfaces [68, 73] in composites with clumped reinforcements. Tube diameter has an

inverse correlation with ISS, as the tube diameter decreases the ISS increases [45, 49]. In a

15

theoretical analysis of spherical particle composites, Chen et al. [72] found that a critical particle diameter existed where the composite demonstrated a peak energy dissipation. At this peak, the dominant factor changed from particle surface area to ISS. For particle diameters above the critical point, the surface area dominated the energy dissipation calculations, with increased surface area providing increased energy dissipation. Once the particle size was reduced to the critical diameter, or smaller, the stress required for interfacial slip became too high for the material to achieve. Thus, fewer interfaces activated the slip mechanic, resulting in reduced energy dissipation. As the composites ability to transfer stress to the interface increased, the critical diameter for peak damping was shown to decrease. Alteration of the particle geometry from spherical to cylindrical offers an effective means to increase the interfacial shear transfer as was shown by the effective fiber length theory [38] and experiments investigating the effects of fiber aspect ratio [35]. High aspect ratio fibers offer an ideal mix. Their relatively small diameter in two dimensions creates high interfacial shear strengths and greater length in the third dimension allows sufficient stress transfer to activate interfacial slip. Once the length is sufficient to generate peak stress the fiber begins to slip as the stress transfer exceeds the ISS. This region is termed the effective length as that portion of the reinforcement fiber that is in slip is dissipating energy, thus effectively contributing damping to the composite material. How vibration will affect materials used in damping also needs to be considered.

Materials used in damping applications are, by the nature of vibration, exposed to cyclic stresses. Xu et al. [74] found during investigation of CNT reinforced silicone composites that damping properties for the material were dependent upon both strain amplitude and number of cycles. Over the course of 1000 cycles at 20% strain, the CNTs became roughly aligned. This was similar to their observations of the same material *in-situ* at 100% strain. The storage and loss

16

moduli were reduced by less than 10%. Increasing the cyclic strain amplitude to 100% caused a

sharp initial decay in both the storage and loss moduli during the first 250 cycles. After this

point, the storage modulus continued to decay slowly, and the loss modulus stabilized. Both

properties lost approximately one order of magnitude during the test [74]. These results indicate

vibration damping properties are likely to be affected by fatigue life and that damping

measurements require break in time for measurement stabilization. Alternatively, if the cyclic

loading is high enough, the properties may never stabilize as indicated in the study of Xu et

al. [74]. Lastly, impact protection applications not exposed to cyclic loading, would benefit from

the higher damping factors seen at the start of testing.

1.2.4. Mechanical and Structural Characterization Methods

To predict or improve the behavior of a material, there must be an understanding of what

causes the behavior. Otherwise, research is limited to randomized trial and error

experimentation. The numerous investigative methods are categorized and discussed in the

following subsections. The first subsection will cover bulk mechanical property tests, followed

by localized mechanical testing methods for materials with small scale inhomogeneity including

nanocomposites. The next subsection covers imaging methods for structural investigations. The

final section presents some potential methods for expanding investigative capabilities.

1.2.4.1. Bulk property methods

Bulk mechanical characterization methods investigate the material on a large enough

scale to normalize local effects such as ductility fluctuations between the crystal and grain

boundary regions, or differences in composite constituents. St. Venant's principal, commonly

used in finite element analysis (FEA), explains how largescale results show minimal change

when small features within the larger system are added, changed, or removed [75]. Commonly

used bulk characterization methods for quasi-static testing include tensile [38, 76], three and four point bending, and compression. Other bulk property tests address responses to dynamic conditions such as impact tests, including Charpy and drop impact testing [74], and vibrational testing such as dynamic mechanical analysis (DMA) [77].

Tensile tests are used to determine properties such as elastic modulus, ultimate tensile strength (UTS), yield strength, and many other properties based off of the stress-strain relationship of the material. Flexural and compressive tests provide similar properties for material bending and compression loading modes. Changing the loading of a sample for testing is innately dynamic, though doing so at a low enough, and material dependent, strain rate approximates a static material condition. This is important as a materials stress-strain relationship commonly exhibits a degree of strain rate sensitivity [78-80].

Most applications, even those with moving parts, are designed to keep the materials within their fully elastic region. Once the material response becomes plastic, any deformation is permanent, thus the part will not return to its original shape when the load is removed. This generally limits the application of intentional plastic deformation of an engineered structure to single use systems, such as the impact energy dissipation for vehicle crash protection [80]. Impact tests and data from the plastic region of the quasi-static tests are used in designing deformable systems and in predicting failure behavior of static structures.

Cyclic testing within the elastic region involves systems where, with time, the load is expected to change significantly, and often frequently during the design life of a component. Applications in this category are designed to remain within the elastic region; however, even without plastic deformation of the material, permanent changes, such as crack propagation, can occur or accelerate due to the repeated cycling of the applied loads. Constant cycling of the load

commonly leads to fatigue type material failures [81], reducing the lifespan of the part. At high amplitude or cycling rates these loading variations can induce further complications by causing vibration within the system. This is particularly problematic if the frequency of the load variations is near the system's natural vibration frequency. A system under harmonic excitation, where the drive and natural frequencies align, can build up enough energy to accelerate fatigue failures, or cross over into the plastic deformation region and tear itself apart. This problem increases as the factor of safety (FoS), the ratio between the stresses induced by design intended loading conditions and maximum elastic stress, decreases. Thus, as the FoS decreases, the excess, beyond design intended, force required to cause material yielding is reduced. This can generally be averted by altering the system's natural frequency via changes to its mass, stiffness, or damping characteristics [82].

As mass is one of the minimization goals for many systems, and dynamic stiffness is generally correlated with quasi-static properties of the structure such as elastic modulus, the property targeted for change is often damping. This may be further prioritized by factors, such as impact risk and survivability requirements for a specified impact load, which also benefit from the increased energy dissipation of damping. There are several commonly used methods for characterization of a materials vibration response. These methods can be categorized by excitation method as either free or forced vibration.

In free vibration, the system under investigation is provided an initial excitation energy, commonly an initial displacement, and then allowed to vibrate at its natural frequency while being monitored. The frequency, amplitude and the change over time for vibration response can then be used to calculate system properties. Material tests can be performed in this manner by standardizing the structure and initial excitation. The materials density is also required for the

vibration analysis and characterization. A commonly used form of this method is single

cantilever beam vibration [17, 20] where a sample of known length, cross section, and density is

mounted with one end fixed and the other free. The free end is given an initial displacement,

released, and the resulting tip motion, with respect to time, is recorded and analyzed.

Investigation of frequency dependent effects are limited by the extent to which the structure can

be varied to change the natural frequency of the test specimen.

Forced excitation, driven, vibration analysis methods are similar in many ways, though

they offer a distinct advantage by being able to investigate characteristics across a broad range of

frequencies. There are several methods available to analyze this type of data, though they all

revolve around the stress and strain relationship of the material. One method is to integrate the

area inside the hysteresis loop formed by the stress-strain curve of a loading cycle to find the

dissipated energy and relate that to the peak potential energy stored during the cycle.

Alternatively, using the stress, strain and time data, the stress and strain waveforms can be used

to determine the phase difference between them. This phase shift is known as the loss factor, or

tan δ, and is defined as the ratio of the loss modulus to the storage modulus of the material. The

storage modulus is a measure of the materials elastic behavior under the conditions, and

generally increases with frequency as this causes the material strain rate to increase resulting in

strain hardening effects. The loss modulus is a measure of the energy dissipation, or loss,

capabilities of the material. This is often referred to as the viscous portion, or behavior of the

material; though the energy dissipation in materials such as polymer-CNT composites is due to

coulomb type damping created by the stick-slip mechanic [17, 18, 20, 68, 69], not viscous

effects.

Dynamic testing with controlled temperatures can also be used to find thermally

dependent properties such as the glass transition temperature of a polymer [83, 84]. Temperature

can be an important factor for polymer damping as illustrated by Wang et al [83]. The peak loss

factor of epoxy with respect to temperature varied significantly across the five different epoxy

content resins tested, all using the same curing agent. The results are shown in Figure 5. This can

have significant impact on material as determined by the expected nominal and extremes of

system's operating temperature [85].
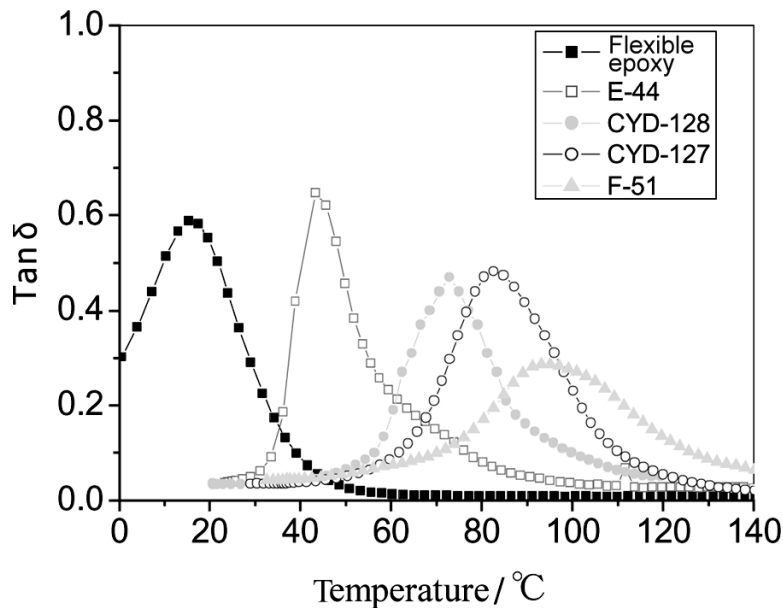
Figure 5. Plot of loss factor versus temperature of different epoxies obtained through DMA
testing in fixed frequency (f = 1 Hz) tensile mode with a 2 °C/min heating rate. Reproduced
from [83]

Loading modes for dynamic testing cover the same spectrum used in quasi-static testing:

tensile [16, 18, 86], compression, flexural [19, 84, 87], torsion [74, 88], and shear modes [85, 89].

Mode selection is influenced by factors including material application, existing sample

geometry, and material stiffness. This can have particular importance for certain materials such

as CNT-polymer composites which require material stresses to exceed the stick-slip activation

stress, as discussed previously, to exhibit maximum damping [17, 18, 20, 68, 69].

1.2.4.2. Localized testing methods

Another investigative route is through localized testing utilizing methods such as nanoindentation [27], nanoscratch [27], fiber pull out [90], and individual CNT [32, 35] testing. These tests provide valuable, but often very specific, information about the materials due to the small scale of the tested area. The value in these methods is the ability to find specific data such as the elastic modulus of a reinforcement fiber to estimate the composites elastic modulus with the Halpin-Tsai model [57, 58] or detailing how PVA crystallization varies around an embedded CNT fiber [38, 54]. Generalizations about bulk material behavior from these types of tests are difficult because of the nonhomogeneous nature of a composite structure and the effect of localized phenomena on observations near the composites constituent length scale. Thus, CNT composites yield nonhomogeneous property values under nanoscale investigation, and it is often difficult to infer accurate bulk behavior from the localized data collected.

1.2.4.3. Imaging

There are many different imaging methods, though they can generally be split into three types: light, electron, and mechanical based imaging. Light imaging uses mechanics such as reflection, refraction, or diffraction of electromagnetic waves, such as visible light or X-rays, to capture an instantaneous image of the whole imaging field [91]. The visible light methods generally focus around direct magnification of details as one's eye would see them [92, 93]. Other methods such as Raman spectroscopy [74, 76] and wide angle X-ray diffraction [76, 94] produce patterns as the waves pass through the material, which must then be interpreted, such as the wide angle x-ray diffraction (WAXD) patterns shown in Figure 6. Different materials produce different radial patterns. Rings indicate a random alignment and short arcs are indicative of structural alignment and their placement shows orientation [94]. The challenge for traditional

light microscopy imaging is the minimum detectable feature size, which is approximately half the wavelength of the light used [91, 95]. Though some new methods can achieve resolutions smaller than 100nm through methods reducing the limitation to 1/5th or 1/10th of the wavelength of the light used, the image can no longer be captured whole but must be scanned point by point as with electron and mechanical imaging methods [91, 95].
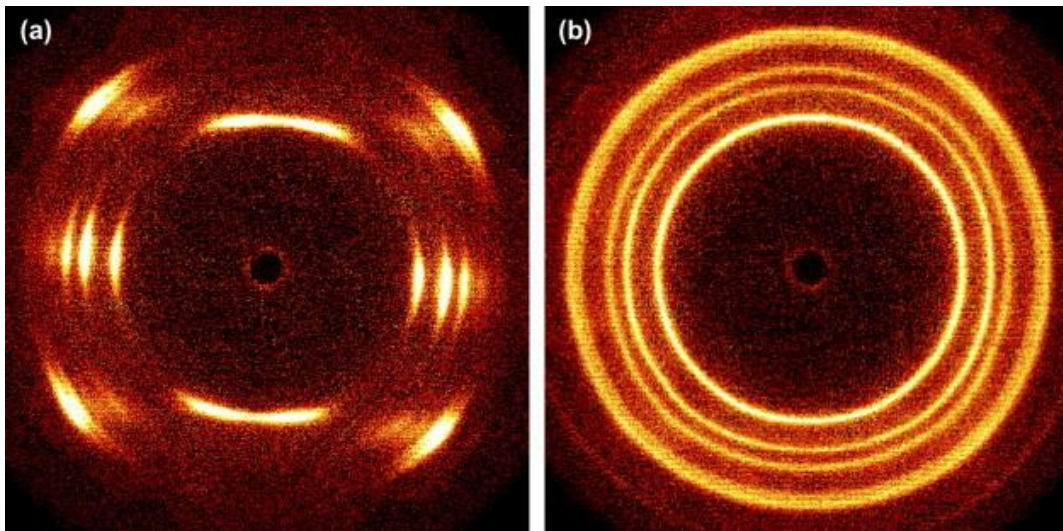
Figure 6. 2D WAXD patterns for a composite of polypropylene and 0.3 wt.% MWCNT produced via (a) dynamic packing injection molding, (b) static packing injection molding. Reproduced from [94].

Electron imaging techniques, which include scanning electron microscopy (SEM) [18, 20, 35, 38] and transmission electron microscopy (TEM) [35, 74, 96], are commonly used in nanoscale investigations. These methods use a beam of electrons as the imaging medium, tracing the beam over the sample in a point by point grid, and capturing data from the electrons interactions with the sample at each point. To facilitate electron microscopy the sample is generally coated with gold, or another element dense enough to interact reliably with the electron beam. The result is a magnified image similar to a visible light image, but with depiction of details smaller than light wavelengths allow. TEM is capable of slightly higher resolution and is often used in tasks such as characterization of CNT wall count, length, diameter, and intertube

structure [74, 96]. SEM is capable of imaging 3D structures and is used commonly in nanomaterial investigations to image material surfaces, such as posttest rupture surfaces [29, 35, 38, 49].

The final category to discuss is mechanical imaging methods. These methods involve mechanically scanning a probe across the imaging area and recording data about the interaction between the probe and the sample surface. Atomic force microscopy (AFM) belongs to this category. There are multiple tip-sample interaction modes based on tip to surface contact, attraction-repulsion forces, and magnetic field effects [97]. For nanocomposites AFM imaging is commonly done using tapping mode [27, 35], in which the sensing tip on the end of a small cantilever beam vibrating near its natural frequency is traced just above the surface of the sample. Due to attraction-repulsion interactions, the vibration amplitude or frequency changes of the cantilever tip can be used to determine how far the tip is above the sample surface. Adjustments are then made to the piezoelectric ceramic controlling the position of the tip, bringing the cantilever vibration back to the target separation distance. The z axis component of the tip location, as well as the tip frequency components can all be graphed to show the surface characteristics of the sample. AFM imaging is sensitive enough to resolve individual atoms as shown in Figure 7.

The power of mechanical methods can be seen in the functionality of AFM, but they also come with limitations. To position the probe tip on the sub nanometer scale requires very fine control which is achieved by the use of a piezoelectric actuator. The tradeoff is the small actuation range of the system. As a result, large x-y image sizes and moderate z axis, height, variations on the surface are not permissible for this type of microscope. This can make locating a specific feature difficult. Additionally, imaging time scales proportionally to image size and

resolution, meaning image collection can be time consuming and effective imaging of dynamic

phenomena is limited. Advances in control systems will continue to reduce these.
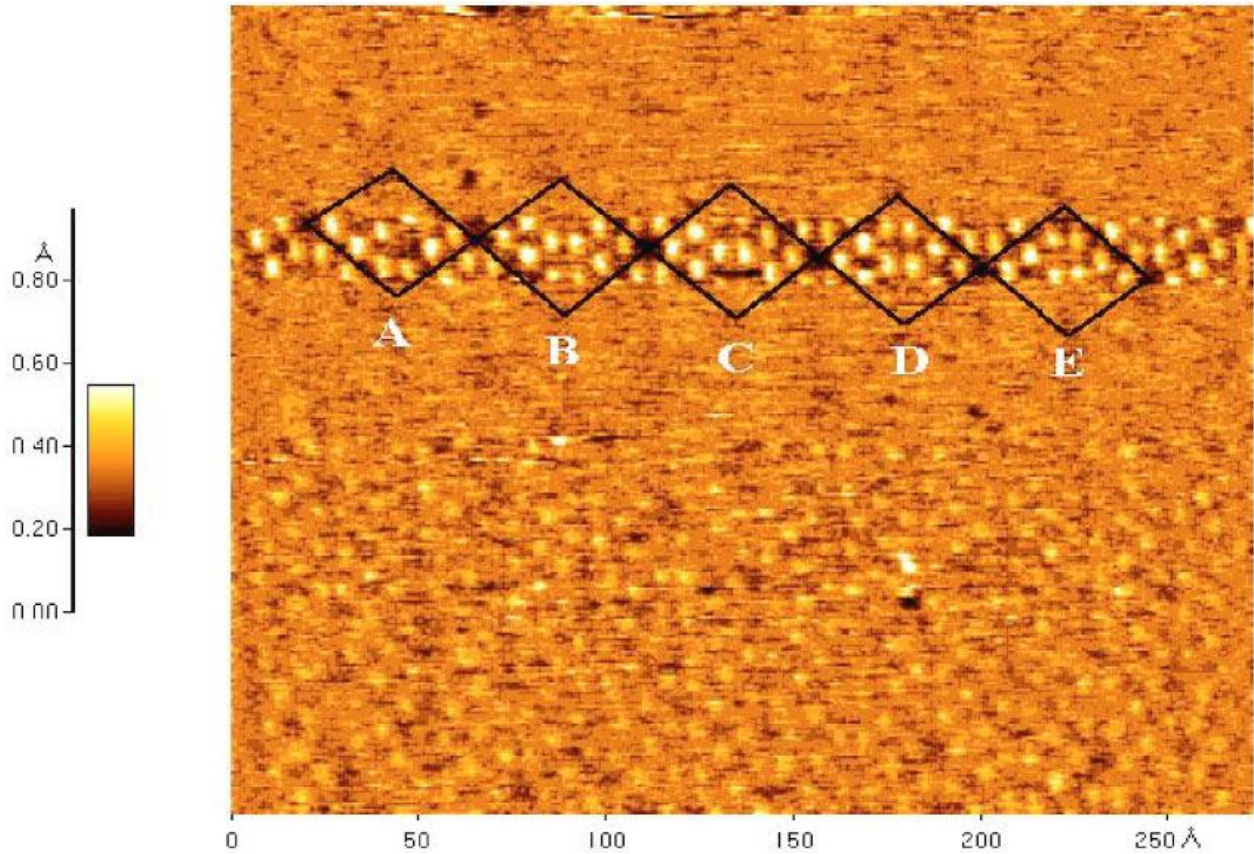
Figure 7. First AFM image of the silicon 7x7 reconstruction with true atomic resolution.
Reproduced from [97].

The myriad types of microscopy provide significant detail about the structure of a

material. Imaging before and after property tests such as tensile or DMA testing provide even

more detail. From these images, permanent material changes can be investigated, yielding partial

insight into the mechanics responsible for the material's behavior. Questions remain, however,

such as what temporary changes occur and how permanent changes progress. The question of in-

process changes is most evident in observation of time dependent phenomena [91]. The primary

tradeoff in selecting a microscopy method for processes such as damping that involve temporally

dynamic structures is resolution versus imaging speed. For nanomaterials, the resolution is

25

paramount as there is no contribution to understanding the material's behavior from any number

of fast images that lack nanometer capability to capture details on the defining scale of the

structure.

1.2.4.4. Imaging/Testing combination

To fully understand the deformation and interaction mechanics of a material, it needs to

be observed during loading. This has long been the case with large bulk sample tests which can

be observed directly during deformation, such as the mechanics of a steel tensile sample. It can

be seen that the steel specimen's elongation and cross sectional area change uniformly until the

onset of necking and finally rupture [98]. *In-situ* imagining is significantly more challenging for

nanomaterials. As discussed previously in the Imaging section, 1.2.4.3, the capable methods

have limitations such as imaging speed, sample size requirements, and minimum observable

feature size. An AFM, for example, cannot simply be aimed at the lab's large hydraulic tensile

tester to produce an image. Through the use of specialized testing equipment however, this

combination of technologies can be implemented. Xu et al. [74] used *in-situ* SEM imaging to

observe the structural changes of CNTs in silicone while stating that TEM was impossible

because of the challenge of preparing thin enough samples with controllable shear strain. They

found that the random CNT dispersion grew increasingly orderly and became aligned at 100%

shear strain, then the CNTs began to clump together as the sample was strained further. Research

has been published using Raman spectroscopy and WAXD to investigate structural changes

under load conditions [76]. The *in-situ* use of microscale loading and various imaging systems

has been employed to study silicon [99] and polyimide films [100] for microelectromechanical

systems (MEMS). Microscale and nanoscale specimens can be exceedingly difficult to

manipulate, however [99, 101, 102]. Many of the potential applications for nanocomposites are

macro scale, thus, it is generally viable to simplify the testing by using a larger specimen size, as noted by Bamberg et al. [103], since the micro/nanoscale interest is structural imaging.

1.3. Research Scope

Research in the area of nanocomposite materials in conjunction with an AFM has been limited. The goals of this work are thus twofold; the development of a load stage capable of working in conjunction with an AFM and to investigate the effects of MWCNT content on the properties of epoxy, including elastic and loss moduli.

The purpose of the load stage development is mechanical characterization of relatively small maximum loads, ranging from 5 to 100 lb, test specimens. This characterization was done both independently and in conjunction with AFM imaging. Imaging of the material structural effects during loading is important to understanding the mechanics driving material behavior. The load stage was designed to fit in the limited sample mounting space of the groups Veeco Dimension 3100 AFM. Additional factors addressed by the design were the positional measurement and control for samples with less than 1 in (25.4 mm) gauge lengths and force measurements on the order of 10^{-2} lb, or less.

Based on these core criteria, a load stage suitable to multiple quasi-static loading modes was designed, built, instrumented and a control program written. A group of initial tests were performed on neat and 1 wt.% MWCNT reinforced epoxy to evaluate the load stage's capabilities. Using tensile loading, the materials elastic moduli were characterized, as well as AFM imaging of sample deformation and crack propagation.

Detailed characterization of materials including UTS, failure strain, glass transition temperature, and loss modulus was performed for epoxy with varied MWCNT content of 0.2, 0.6 and 1 wt.% using the load stage and DMA. A dynamic control program was developed for the

load stage for investigation of higher strain amplitude vibration than available through DMA testing. Dynamic tests performed on the load stage and DMA to gather data for the four sample sets. From these data sets, potential was evaluated, and improvement recommendations were made for the dynamic capability of the load stage as needed.

This paper and research, therefore, is comprised of six chapters. Chapter one introduces the research motivation and covers the necessary background information for understanding of the necessity of the research presented here. Chapter two details the design criteria and solutions for the load stage mechanical, instrumentation and control systems. Chapter three consists of the first journal article published from this work "Nanoscale Structural and Mechanical Characterization of MWCNT-reinforced Polymer Composites"[67]. The latter article covers the investigative capabilities of the load stage with AFM combination to observe nanoscale deformation during sample loading. The first part of chapter four is the second journal paper written from this research. This article covers the quasi-static and dynamic investigation of epoxy and 0.2, 0.6 and 1 wt.% MWCNT reinforced epoxy composites. The particular properties covered are elastic modulus, ultimate tensile strength, failure strain, glass transition temperature and loss modulus of the materials and how the properties are affected by the MWCNT content. The final section of chapter four covers the current dynamic testing capabilities of the load stage, the system requirements for adequate dynamic testing, and suggested methods to implement these requirements. Finally, chapter five will summarize findings of this research, and outline the areas of particular benefit for future works.

2. DESIGN AND CONTROL OF AN AFM COMPATIBLE LOAD STAGE

To better understand the fiber-matrix structural behavior during loading for nanocomposites, such as MWCNT-epoxy, loading must be combined with an appropriate scale microscope. Atomic force microscopy was chosen for this purpose due to its excellent nanoscale imaging capabilities combined with the ability to perform nanoscale mechanical investigations. It was also concluded that stand alone functionality for the load stage should be pursued for testing specimen consistency and overall in-lab investigative capability.

The functionality of this system combination is expected to provide greater insight into the micro/nano scale structural analysis through *in-situ* observation of material behavior. Properties of particular interest to this work are nanostructural deformation and component re-orientation, crack propagation, tensile stress-strain characteristics and damping behaviors. These goals will provide the primary design criteria for the load stage.

This chapter is broken up into two main sections for the hardware and control portions of the system. The hardware section begins with the major design constraints for the load stage followed by component selection, mechanical design and signal acquisition. The control section covers the control principals used as well as the software implementation and interface.

2.1. Mechanical and Electrical Design

2.1.1. Design Constraints

The design constraints can be broken out into several major constraints.

- *Size/Space limitations*
- *Testing flexibility*
- *Load capability*
- *Accuracy*
- *Reliability*

Space was a significantly limiting factor for the load stage design. Since AFMs are

intended for nanoscale interaction, they are generally not designed with large sample staging

areas. The AFM being used here was a Veeco Dimension 3100. This model has a sizable open

area in the x and y-axis directions on the granite positioning surface as shown in Figure 8. The z-

axis was the primary limitation affecting the sample mounting height and total height of the load

stage, as shown in Figure 9A. The AFM tip holder assembly posed additional limitations. The

AFM scanner tip is the lowest point of the sensor head unit, enabling it to be positioned over any

part of a sample held from below. Thus, the vacuum chuck design used to hold the sample from

the side opposite the observed surface by the positioning stage provided standard with this AFM

model. For certain tests, such as tensile loading, the load stage must be able to grip the sample to

provide adequate force transfer to the sample. The tip holder dimensions are shown in Figure 9B.

Any mounting mechanic going over the sample would impact imaging area on the sample,

though minimizing the thickness would reduce the impact on imaging area.
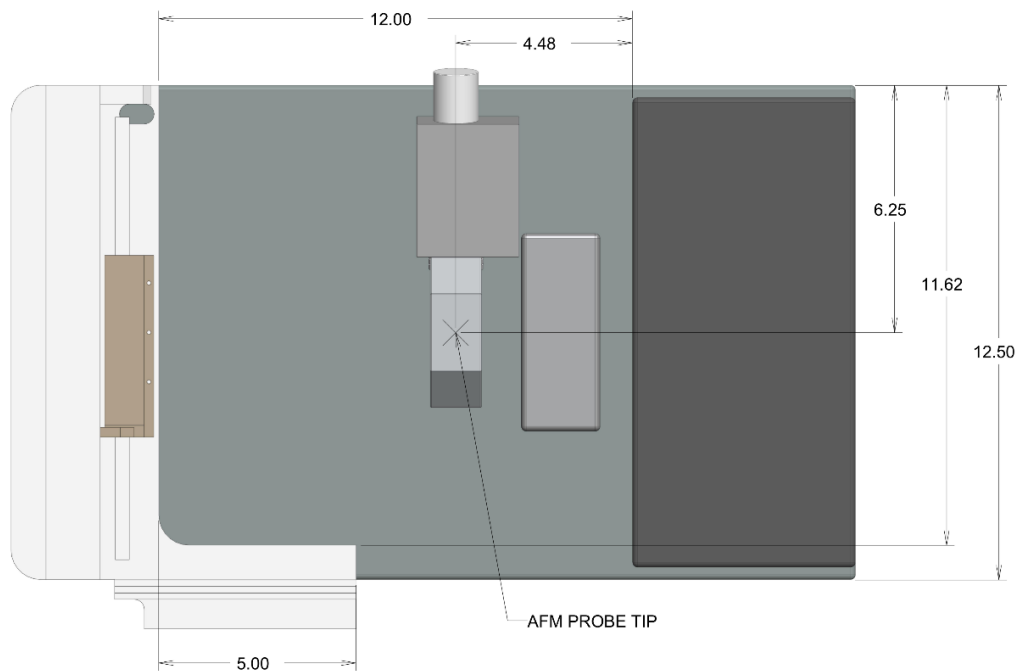
Figure 8. Available space on granite surface of AFM x-y position system (unit: in.).
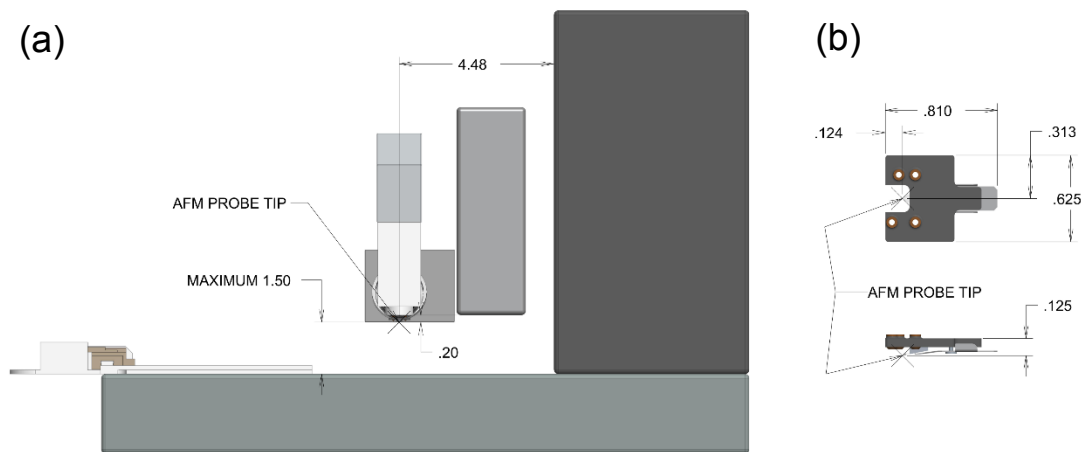
Figure 9. AFM height limitations. A) z axis limit for tip safety and functional measurement range. B) tip-holder dimensions for mounting impact (unit: in.).

Measurement accuracy was also a concern for the system. The samples represent bulk material properties, but due to the space limitations and the materials of interest, the samples must be relatively small. It was important to maintain flexibility in order to maximize the measurement accuracy. The range of force measurements in particular can vary significantly depending on the test material and test specimen size. The ability to vary the measurement range can be used to support the measurement accuracy by matching the measurable range to the forces needed to test the specimen. The tensile force needed for a flax fiber is low compared to the force needed for a steel specimen with a larger relative cross section. Alternative loading mechanics, such as bending tests, would cover a wide range of force measurements as well. For these reasons it was desirable to design the load stage to handle small loads (approximately 1 lb) up to as large as is reasonable. Maximizing the force measurement range was desirable to maintain overall system flexibility to test a greater variety of specimen sizes and material combinations.

It was desirable to incorporate flexibility in other aspects of the load stages testing capabilities, beyond the force measurements previously mentioned. Flexibility was maintained in several ways, particularly in simplifying the mounting connections to allow fixtures for alternative loading mechanics to be used. A basic example of this would be a design allowing tensile test specimens to be clamped or adhesively fixed to the mounts. Adhesive mounting would reduce some of the sample imaging constraints caused by the AFM tip assembly discussed previously, while clamping supports higher loading of the specimen. Bidirectional loading for tensile or compressive applications was another important aspect of flexibility. The final flexibility constraint was the desire to implement dynamic testing capabilities for characterization of vibratory material responses, particularly material energy dissipation.

The final major concern was reliability. The components must be able to provide a reasonable lifespan under normal handling and operating conditions. Sensors capable of high accuracy at low force must be protected from possible overload during sample mounting. The moving parts need to handle repeated use for many tests.

Along with these primary concerns, there were a number of other factors important to the design. The granite surface for x-y positioning under the AFM must be protected to avoid damage from use of the load stage. The load stage needed to use the existing mounting connections to the x-y positioning system to simplify changeout of the load stage and the standard AFM vacuum chuck. Common mounting simplified the system to make changeover easier and minimize the risk of damage to the AFM during the process. Mounting the load stage to the existing x-y positioning system of the AFM, shown in Figure 10, was done to facilitate the small adjustments needed to track a surface point during combined loading and imaging tests.

ITEM	DESCRIPTION
1	AFM Granite Base
2	Y SLIDE
3	X SLIDE
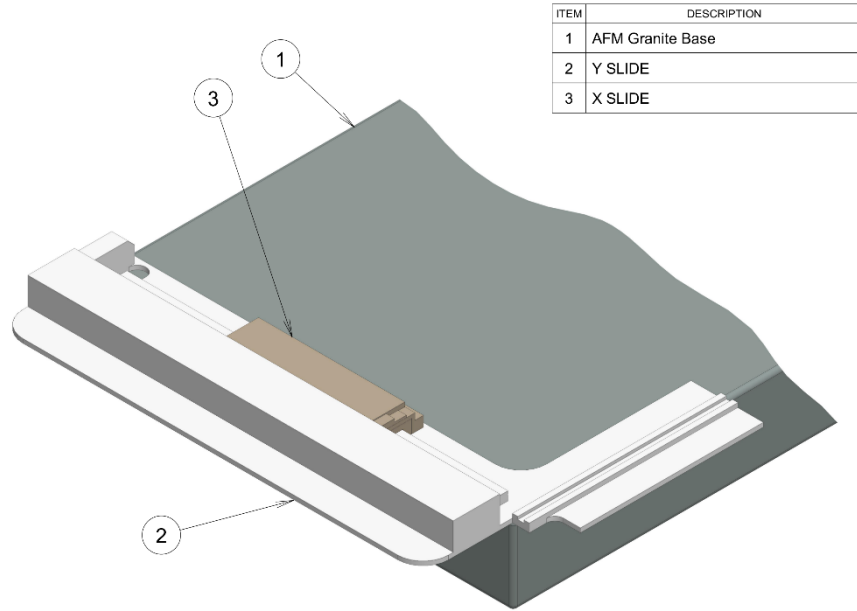
Figure 10. AFM x-y positioning system.

2.1.2. Coarse System Design

Several general designs were devised and evaluated during the initial design phase. Basic component research was also performed throughout this phase as part of the feasibility assessment for the various designs. Several of the preliminary designs that received the most consideration are shown in Figure 11. The twin screw designs were eliminated due to the drive complexity required to maintain even displacement with minimal backlash for cyclic test potential. The complexity was deemed too costly for both time and materials, and was likely to require too much space. Using a linear actuator as the drive would have greatly simplified the drives design requirements, unfortunately the limited space available on the AFM precluded an in-line arrangement unless the x-y positioning system was removed from the AFM. Removal of the positioning system would have significantly increased changeover difficulty between the load stage and the stationary stage, as well as precluded use of the positioning system with the load stage. The offset loading-drive systems, such as the side jaw concept shown in Figure 11C,

added complexity in other ways. The primary concern was that the large moment created by the offset would cause greater static and dynamic friction. The geometry would also amplify wiggle resulting from necessary joint clearances, and increase the effect of structural flexure on the measurements. Thus, evaluation of these initial concepts led to the selection of the concept shown in Figure 11D. The final selection was based on component availability, space limitations, drive simplicity, and proximity of the force alignment for the drive and sample load.

(a)

(b)

(c)

(d)
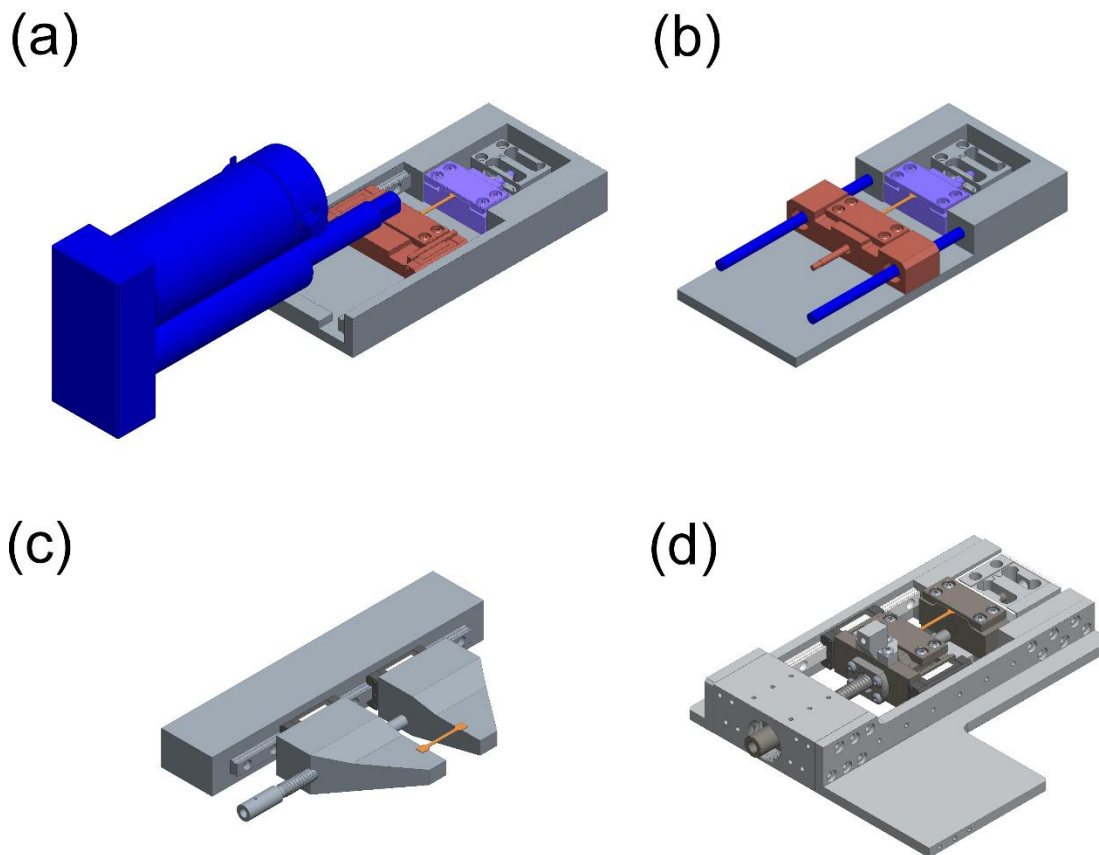
Figure 11. Preliminary design concepts. A) linear actuator, B) cylindrical guide bearings, C) offset jaw, d) centered lead screw (chosen route)

2.1.3. Component Selection

The design started with drive and load cell selections. From a design perspective, the easiest drive solution would have been a linear actuator, typically a pre-constructed lead screw and motor assembly. Unfortunately, space limitations precluded this option. The space limitations were driven by the AFM geometry as well as the desired centerline load stage drive configuration. To minimize flexure within the system it was desirable that the drive force be applied as close as possible to the centerline of the load. The height limit of the AFM tip assembly requires that the drive system fit within 1 inch vertical space, between the granite AFM base and the test specimen, to maintain the centerline alignment. The available length of space on the sample centerline was limited by the cross bar of the x-y positioning system. These factors limited the options to either finding a linear actuator that was less than 4 inches long, or mounting it significantly offset from the centerline. While the available selection of linear actuators on the market was substantial, one could not be located with the required length and viable maximum force and displacement characteristics. A linear actuator of a suitable length would have limited the maximum force to approximately 20 lb and displacement to less than 1 inch. At that point the decision was made to use an independent lead screw and motor design. This allowed the lead screw to attach directly to the moving sample mount near the loading centerline, while freeing the motor to be mounted elsewhere.

Load cell selection posed several difficulties, the first of which was overload protection. Most of the load cells found were designed to handle a percentage overload ranging from 150% to 500%. This method is very effective for a 10,000 lb load cell, but simple handling of a 1 lb, or less, load cell could easily overload the sensor. For a system where the load cell would be permanently mounted and could be protected by the rest of the system this could have been

35

tolerated. To maintain flexibility of the load stage though, the system needed to have interchangeable load cells, which would require handling and remounting by anyone using the machine. This criterion narrowed the possible options to the LSM250 and LSM300 product lines manufactured by FUTEK Inc. The 1 lb or less load cells in the LSM250 line offered 50 lb overload protection, and the greater of 200 lb or 200% of rated load for the LSM300 line. This product line also satisfied the requirement for interchangeability as both models use the same mounting configuration, offering peak load sensing capacity ranging from ¼ lb to 500 lb capacity. These load cells also offered a height, ½ inch total, suitable to the design space, high measurement accuracy, and bidirectional loading capability. Based on these factors, the FUTEK sensors were selected for the design.

The selected load cell functions by measuring the strain at four points in a parallelogram structure as shown in Figure 12. The strain gauges are placed at the thinnest parts of the structure as labeled and the load is applied to the center beam. Measurements of the material strain are taken and converted to force measurements through known material properties and calibration data. This design provides its high overload protection by limiting the deflection of the center beam. Before the load exceeds the elastic limit of the material, which would permanently deform and damage the load cell, the beam hits the stops and changes the load bearing geometry of the structure. This change allows the load cell to withstand sufficient overloading to protect it during installation and sample mounting.

Having the drive mechanic and the load cells selected allowed for a basic design mechanic to be chosen. The result was a design placing the low profile of the load cell and its sample mount in the 'back', under the AFM tip assembly, and a single lead screw to drive the

'front' sample mount between a pair of guide rails. This basic layout is illustrated by the portion

of the completed design shown in Figure 13.
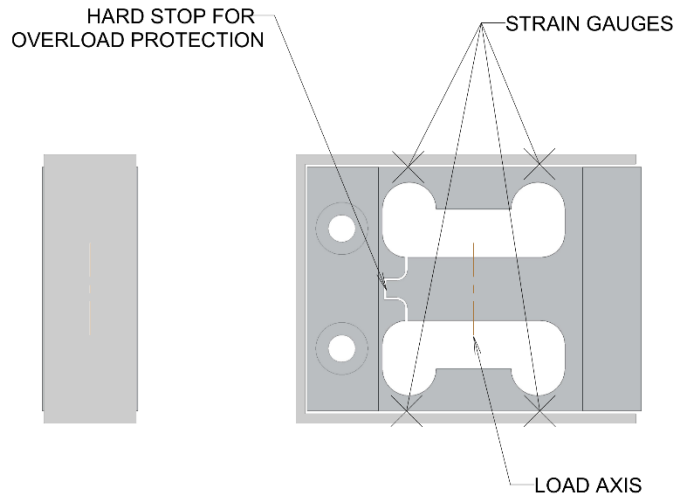
Figure 12. FUTEK parallelogram load cell
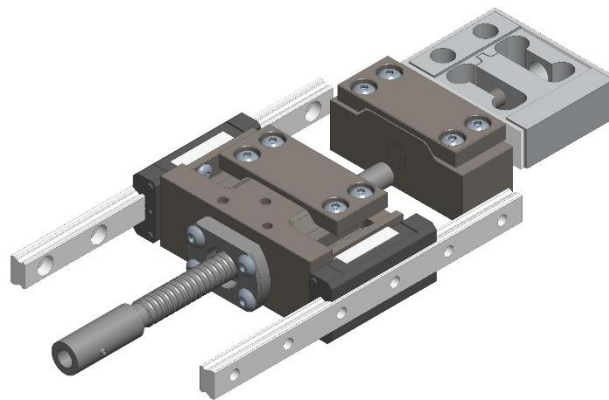
Figure 13. Basic load stage design layout: sample mounts, load cell, lead screw, and guide rails.

Selecting the appropriate lead screw was dependent primarily on maintaining as much of

the load cell force range as possible while conforming to the space limitations. To maintain long

life, low required motor torque, and minimal thread backlash the selection was narrowed to ball

nut lead screw assemblies. The penalty for this choice was the size of the ball nut. Rather than

simply threading the mobile mount to drive it with the lead screw, a specialized ball bearing nut

was required. The available ball nuts found at the time generally doubled the diameter of the lead

screw assembly. This limited the standard options to 5/16 inch (8 mm) maximum thread

diameter to ensure the total assembly stayed safely under the 1 inch height limit of the AFM. A

lower thread pitch was desirable because micro-positional control and reduction of motor torque

were more important than a high displacement rate. Thread pitch tolerance was also important to

minimize control system adjustments needed to maintain a consistent displacement rate. Based

on the discussed criteria a ball nut lead screw assembly manufactured by THK with an 8 mm

diameter was selected. The lead screw was able to handle quasi-static loads up to 250 lb and a

dynamic life of approximately 10,000 cycles[1] with a 200 lb load. The lead screw also offered

minimal backlash which was desirable for continuous movement during load reversals occurring

as part of certain dynamic testing modes. Images from the 3D model of the as received lead

screw assembly are shown in Figure 14.
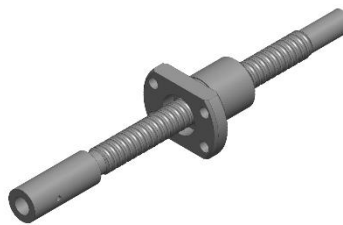
Figure 14. THK ball lead screw assembly

The next major component affecting load capability, and many other aspects of the load

stage, was the motor. The motor selected needed to be suitable for the space available, operate at

a safe and manageable voltage, and be capable of sufficient torque to generate the desired test

---

[1] Cycle life calculated based on manufacturer data [104].

force when combined with the already selected lead screw. The torque, T, required to generate a given load can be calculated by [104]

$$T = \frac{P_h F_a}{2\pi\eta_1} \tag{8}$$

where F_a is the linear force generated by the lead screw, P_h is the screw lead or distance traveled in one revolution, and η_1 is the screw efficiency. Based on application of the manufacturer's reported thread pitch and a conservative efficiency value from the range of listed applications for the lead screw, equation (8) simplifies to

$$T = 0.362 F_a \tag{9}$$

where the units for T are in N·mm and F_a are in N. Alternate calculation based on ideal estimates reduced the torque requirement by less than 10%, indicating variation in application efficiency would not excessively affect the required drive torque. An initial value for F_a can be estimated as the maximum force capability of the load stage plus an allowance for friction and other forces experienced by the mobile mount. The lead screw force is also limited by the material capabilities. To maintain a suitable component life these estimates resulted in a maximum dynamic force, F_a, of 1050 kN (236 lb). This limits the maximum lead screw torque requirement to 380 N·mm (53.8 oz·in). Initial design considerations also indicated selection of a motor with encoder feedback for use in the feedback control loop. The final aspect of motor selection was the ability to maintain a load bearing position to allow time for AFM imaging of the sample. By nature of their drive mechanic, stepper type motors require higher force to turn than other motor types when in the off state, and will exert force to hold their position when in the active state. Based on these criteria a stepper motor, with encoder, from Quicksilver Controls, Inc. was

selected. The motor is capable of significantly more torque than required across a broad range of RPM.

With the lead screw and motor selected, the next step was how to connect the motor to drive the lead screw. The selection was initially limited to options with a direct connection which eliminated non-toothed belt drives because of slippage. This was done to maintain the option for known positional displacement of the mobile mount based on feedback from the motors rotation as measured by the encoder on the motor. Due to space limitations, backlash concerns, and component availability, gear and chain drives were also eliminated as options. A toothed belt drive provided the greatest flexibility to offset the motor axis from the lead screw axis by minimizing the previously discussed concerns. The offset distance could be increased without adding complexity, simply using a longer belt. Components were readily available, and belt designs with fiber reinforcement limited belt stretch which would manifest as backlash during directional changes. Thus, the choice was made to use a toothed belt system to connect the lead screw and the motor. The system selected from Sterling Instruments provided sufficient torque transfer, minimal backlash and belt stretch, and sufficient component selection to support a sufficient reduction ratio within the space limitations of the final design.

Figure 15. Lead screw belt drive components

Determining the position of the mobile mount based on encoder counts from the motor was viable based on the components selected, but not ideal. There was no way to account for slip

in the drive system, tolerance variations in the lead screw, for positional changes that occur while

the system is not running, or control system errors. Connecting an absolute position
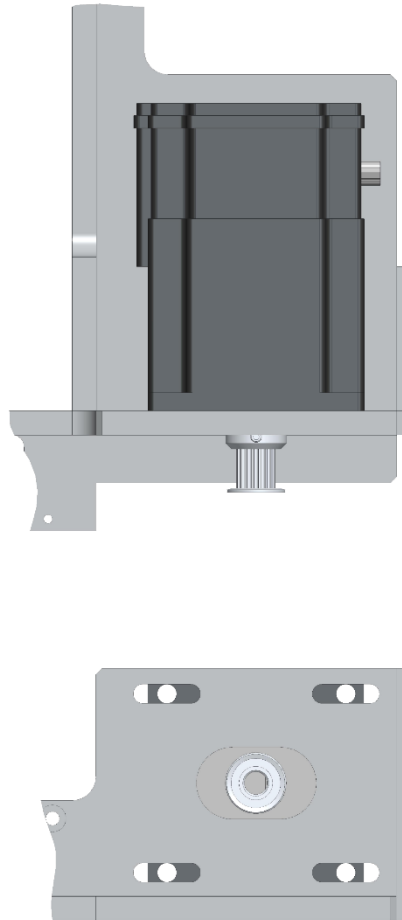
Figure 16. Motor mounting with adjustment slots for belt tension.

measurement sensor directly to the mobile mount eliminates these problems. Several types are

available including encoder, inductive, and resistive. A resistive type linear potentiometer does

not require any record of previous positions to determine the current position as an encoder type

would. Inductive type sensors were not well suited to the low voltage DC power supply required

by other selected components. This lead to the selection of a resistive type linear potentiometer.

The sensor provides a pair of resistances based on the sensors position. Measurement of the

voltage change across the two resistances could then be used to determine the position. A

41

resistive linear position transducer from Duncan Electronics, Inc. was selected for this

application based on the size, electrical requirements, and accuracy of the product[2].

The final remaining components were the bearings; linear bearings for the mobile mount

guides, and axial and thrust bearings for the lead screw. The primary concern for these

components was size because it was the most limiting selection factor. Durability, friction, and

load handling capabilities also factored into the selections. Linear bearings from THK were

selected for their combination of size, accuracy, and friction to facilitate even, smooth motion of
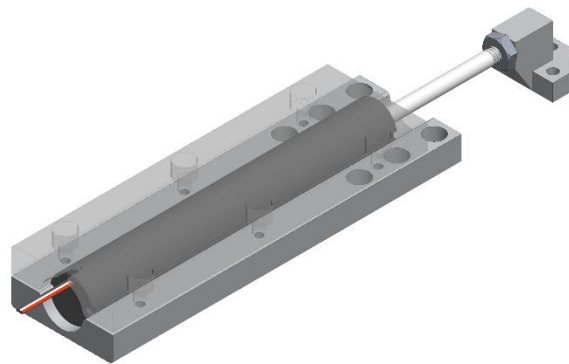
Figure 17. Linear potentiometer mounting and jaw connection. Top mount shown
semitransparent for clarity.

the mobile specimen mount. Options for the axial and thrust bearings were broader as much of

the performance, such as clearance and friction, can be altered through variation of the mating

component designs. Components for these needs were selected from those readily available

through McMaster-Carr as the design progressed. Figure 18 and Figure 19 show the design

solutions for the bearings needed.

---

[2] A complete data sheet is included in Appendix A on page 124.

ITEM	DESCRIPTION
1	Axil Needl Bearing
2	Seal Ring
3	Stub Shaft
4	Hardened Washer
5	Roller Thrust Bearing
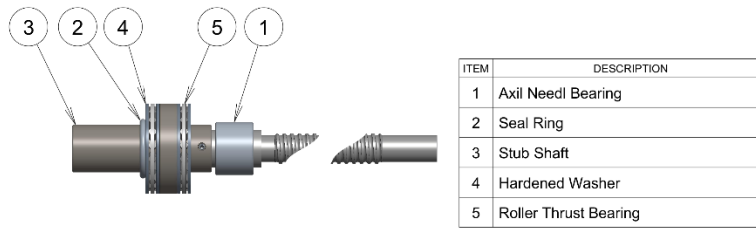
Figure 18. Lead screw bearing assembly.
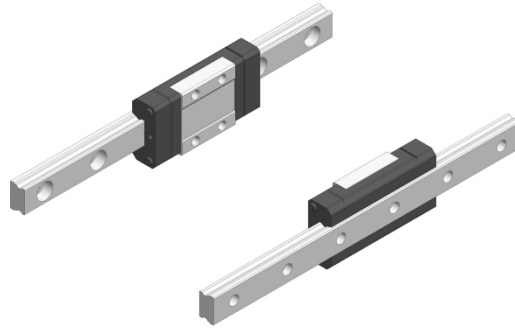
Figure 19. Mobile jaw guide rails (linear bearings).

2.1.4. Final System Design

Through the process of component selection, a basic design layout was developed. From there details were added to complete the design to its final state. Many of these tasks were straightforward, such as mounting of the load cell, as the component manufacturers provided detailed application information. Others, such as the lead screw bearings were more complicated, as a method for resisting thrust in both tension and compression had to be designed. Figure 20 shows an isometric view of the completed 3D CAD model with the major components labeled.

To support the lead screw an axial bearing and a pair of thrust bearings were mounted in the 'front' portion of the load stage frame. The axial load is supported by a needle bearing pressed into the front block. The end of the lead screw was turned down slightly to provide a running fit with the bearing, the hardened surface of the lead screw acting as the bearing race. A flanged stub shaft was fitted over the end of the lead screw to provide a contact surface for the

43

ITEM	DESCRIPTION
1	Test Sample
2	Load Cell
3	Linear Potentiometer
4	Sample Mount - Sensor Side
5	Sample Mount - Mobile Side
6	Stepper Motor
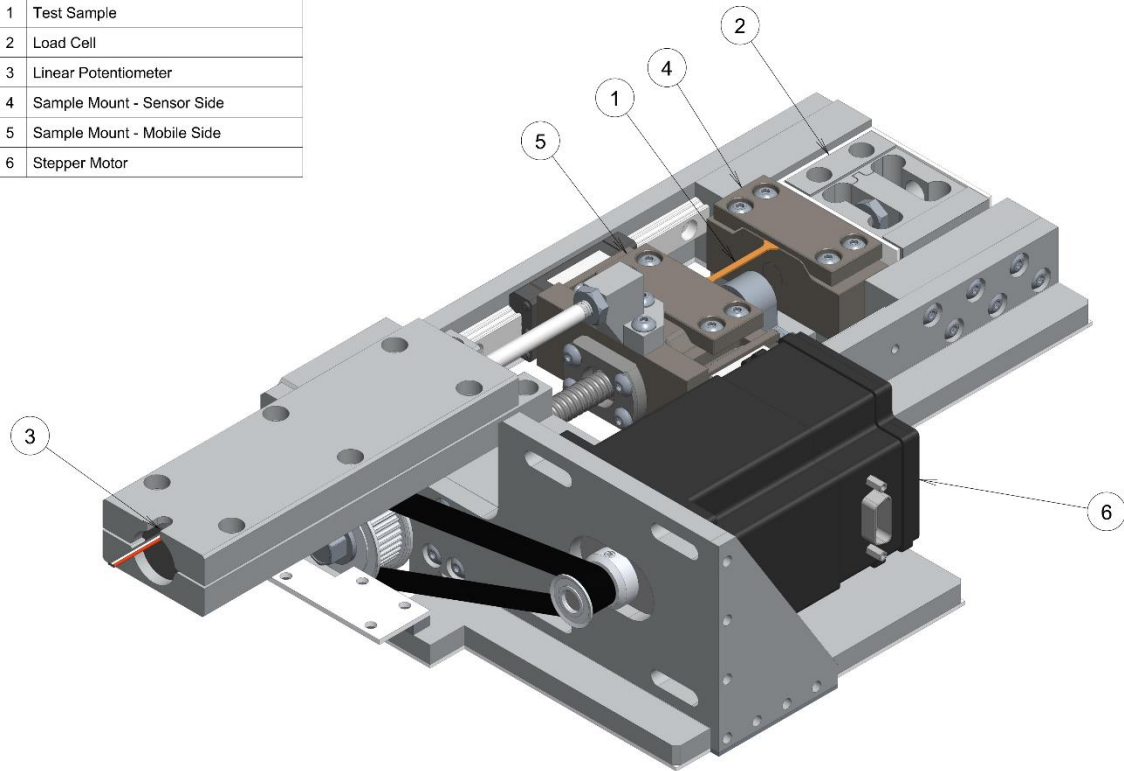
Figure 20. Complete load stage design with major components labeled.

thrust loads. Two roller thrust bearings with hardened washers were fitted to either side of the

thrust flange and nested into the front block. The tensile load bearing presses against the front

block. The compression load bearing is supported by the housing nut, which can be adjusted to

set the bearing preload. Insufficient preload leaves clearance in the bearing allowing undesirable

linear motion of the lead screw, while excessive preload leads to higher drive torque and

increased component wear. The drive end of the stub shaft fits up with one of the timing belt

pulleys, and the shaft assembly is fastened together with a bolt running through the pulley and

stub shaft into the lead screw. The bearing housing included seals on both ends so the bearings

could be packed with grease at assembly. The load cell was mounted in the 'back' of the load

stage, recessed into the frame to minimize its exposure to wear and impact during handling. The

sensor end sample mount was connected to load cell by a shaft that was permanently pressed into

44

the mounting block to provide a solid and easy to manufacture connection. The shaft screwed into the load cell and was locked in place by a jam nut. Figure 21 shows a cross section of the of the load stage vertically through the centerline to illustrate these design details.
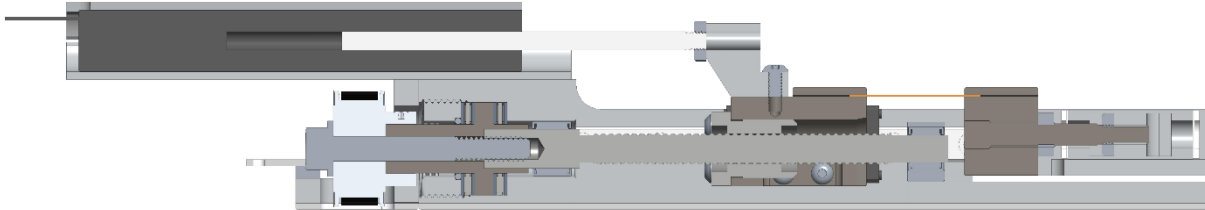
Figure 21. Cross section cut vertically through the load stage centerline.

The linear potentiometer was mounted above the lead screw, allowing it to hang over the x-y positioning system. Since the potentiometer would be sticking out past the main portion of the load stage frame, it was mounted inside of a full length two-piece housing for protection. The mobile specimen mount was notably the most complex geometry among the manufactured components as it connected many of the core system components: the test specimen, linear guide bearings, lead screw nut, and the linear potentiometer. Once all of the core components were placed and fitted the final details fell into place. The motor fit easily alongside the test bed, and slotted mounting holes made it easy to adjust the belt tension. The final detail was Teflon sheet on the bottom side of the load stage to prevent any sharp metal corners from contacting the granite AFM stage, and help the load stage slide smoothly once in place.

Figure 22 through Figure 25 show the final load stage 3D CAD model and fit-up with the AFM. Figure 26 shows the completed load stage sitting in the AFM during the initial testing stages of the project.
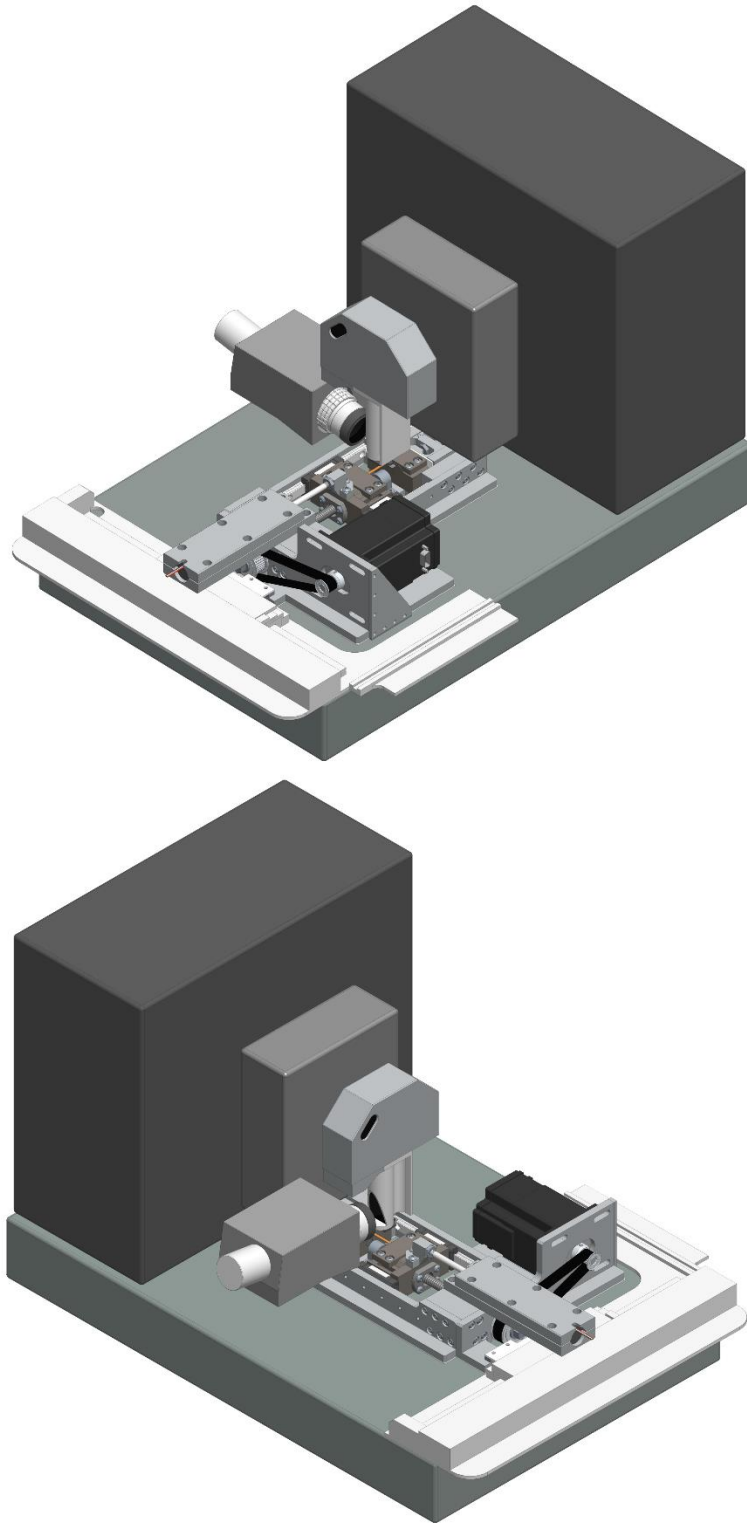
Figure 22. Load stage on AFM. Top: Front right, Bottom: front left ISO views

ITEM	DESCRIPTION
1	Test Sample
2	Load Stage
3	AFM Scanner Head
4	Optical Camera
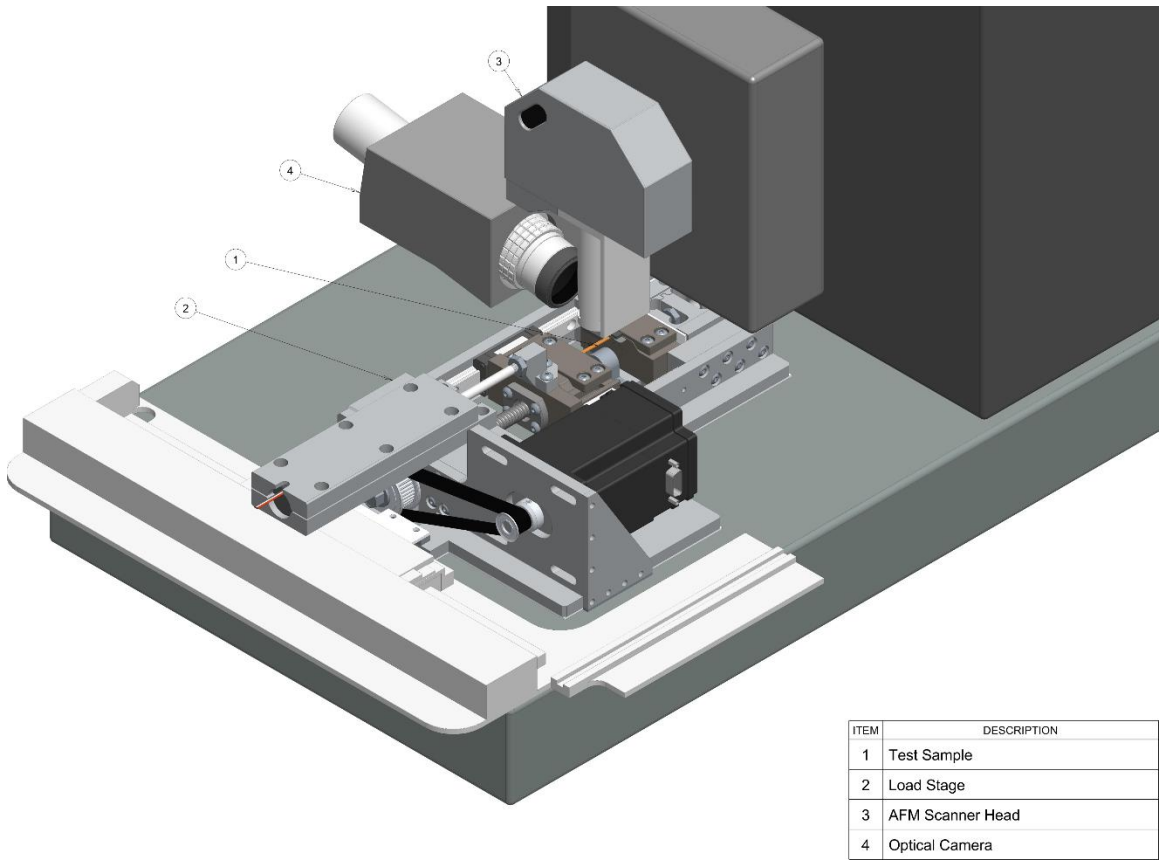
Figure 23. Load stage on AFM, close-up ISO view with labeled components.
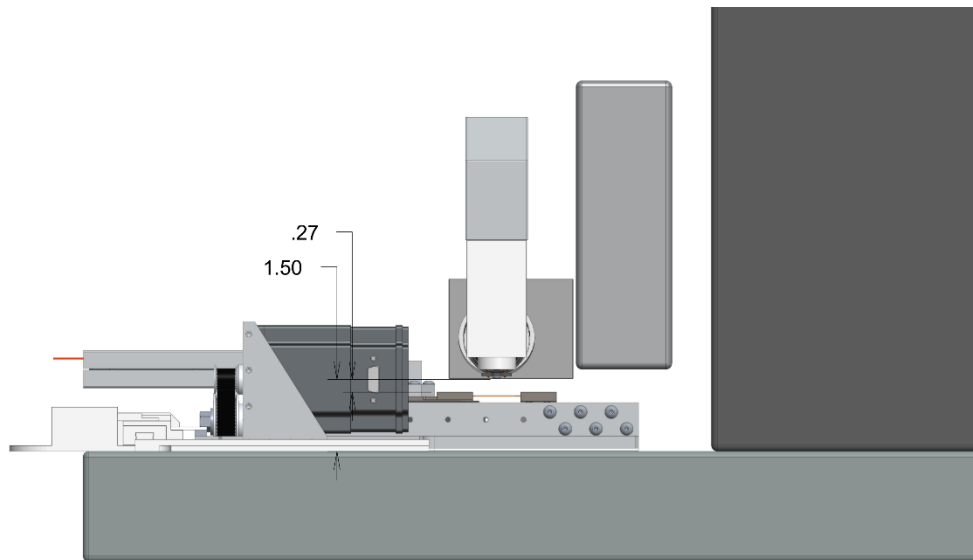
Figure 24. AFM tip clearance vs. load stage, side view
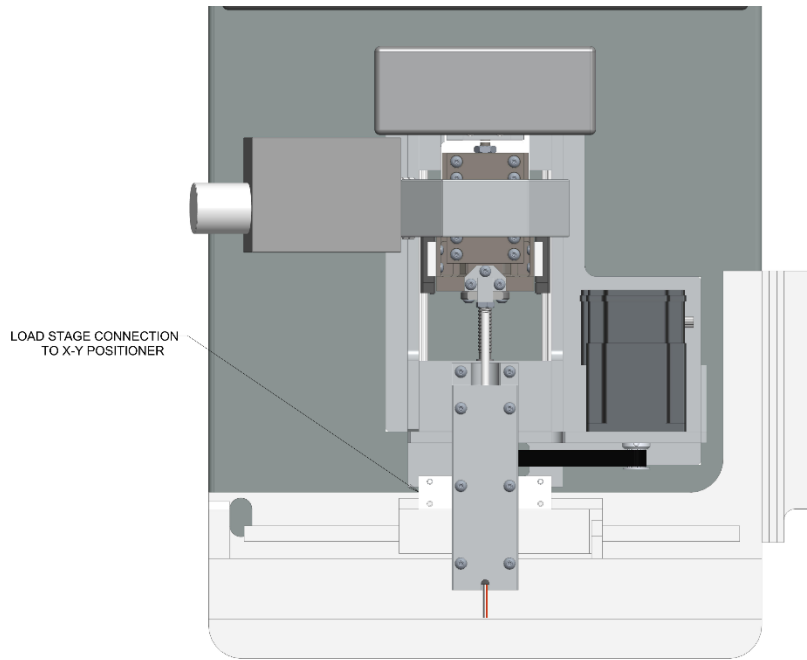
Figure 25. Load stage-AFM mounting/combination
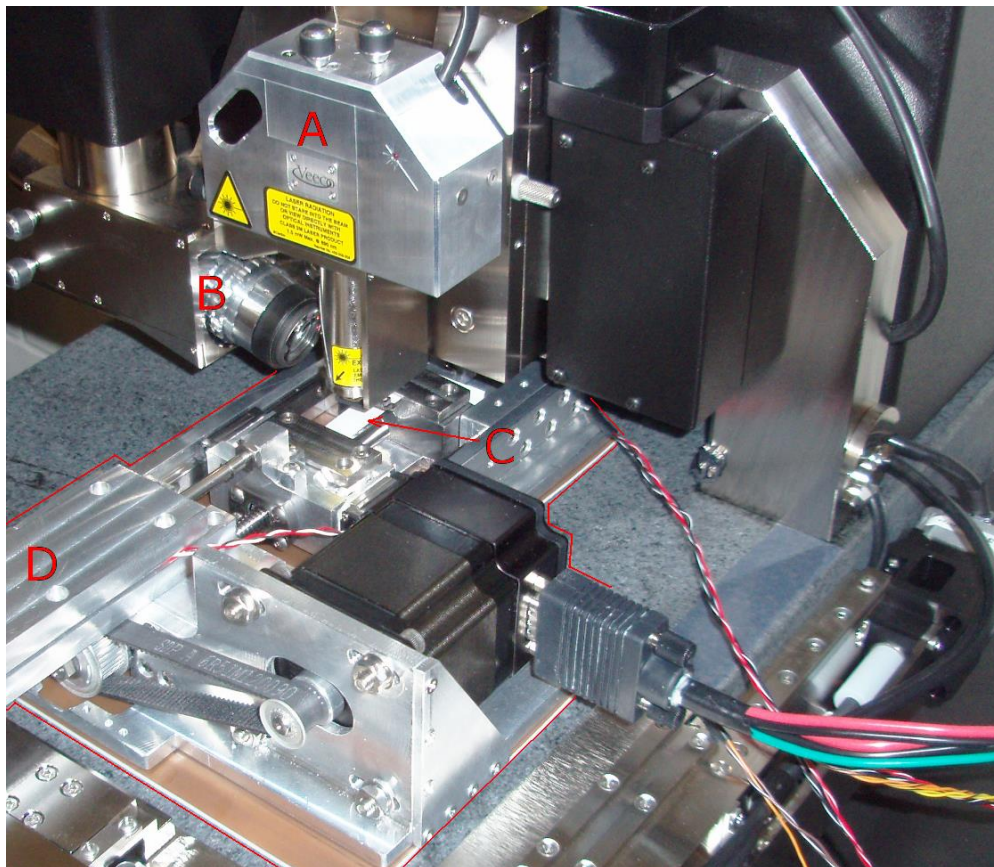
Figure 26. Completed load stage. A) AFM scanner head, B) AFM optical camera, C) test specimen, D) load stage.

2.1.5. Electrical Interface/Data Acquisition

Once the load stage was built, the electrical system was required to get it running. Most of these components were purchased, including the stepper motor driver, a pulse generator to control the motor speed, and a data acquisition system (DAQ) to interface these components with the computer. The analog sensor circuitry was designed and tuned specifically for the components selected.

To get a clear measurement signal the design started with a power supply filter. Based on the low current 5V DC system needs and design simplicity an RC power supply filter was selected. Capacitors and resistors values were initially estimated. The components were then fine-tuned by recording voltage readings through the DAQ and calculating the spread of the readings over time. This was repeated through several iterations for varying capacitor values, keeping the best performing options. The optimized values were identified when changes in either direction, increasing or decreasing capacitance, caused the voltage fluctuation to increase. The finalized power supply circuit diagram is shown in Figure 27.
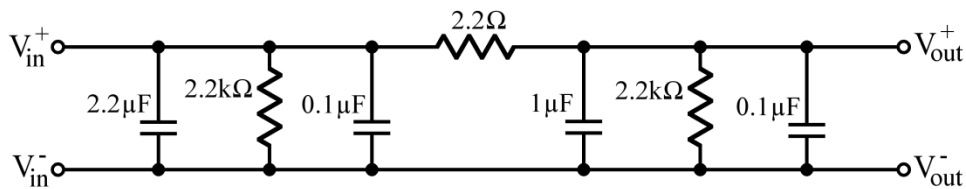
Figure 27. 5V power supply filter diagram.

With the power supply filter in place, the next step was the measurement signals. The first being the load cell. Voltage outputs from strain gauges are very low so they must be amplified for best results. This is typically done in two parts. First the strain gauges are built into a Wheatstone bridge to increase the output sensitivity. In this case the chosen load cell line

49

contained a full 4 strain gauge bridge, simplifying the design to require only connecting the two supply and two signal lines to the electrical system. The second component is a signal amplifier, an INA126 op amp was used for this purpose. The circuitry requirements are well detailed in the manufacturer's documentation. Pins 1 and 8 are connected with a resistor which determines the amplification factor. In this case a 383 Ω resistor correlates to a gain of 213. This value was selected based on the rated load cell output of 2 mV/V to bring the amplified output to ± 2.14 V. Centering the output at 2.5 V nominal then provides a reasonable safety factor in the 0-5 V output range of the amplifier circuit. Using the maximum range would provide slightly higher accuracy, but the safety margin is important to protect the equipment and ensure accuracy of the recorded data. If the signal exceeded the op amp output or analog to digital converter input limit unexpectedly, it would be impossible to determine if the cutoff in the data was caused by a plateau in the sample loading or in the data processing and collection system. Several capacitors were also added to the circuit to reduce signal noise. The finalized op amp circuit diagram is shown in Figure 28.

The second measurement requiring circuitry was the resistive linear potentiometer. As the selected potentiometer moves, the resistance between the center supply contact and the two end signal contacts varies from 0 to 3 kΩ. By connecting the 5 V supply to the center contact the output could be read as the voltage across the two output contacts as they dissipate to ground. Resistors, 1 kΩ each, were placed in series between each of the outputs and ground to prevent excessive current flow through the potentiometer. Several capacitors were added to the circuit to reduce signal noise. The finalized potentiometer circuit diagram is shown in Figure 29.
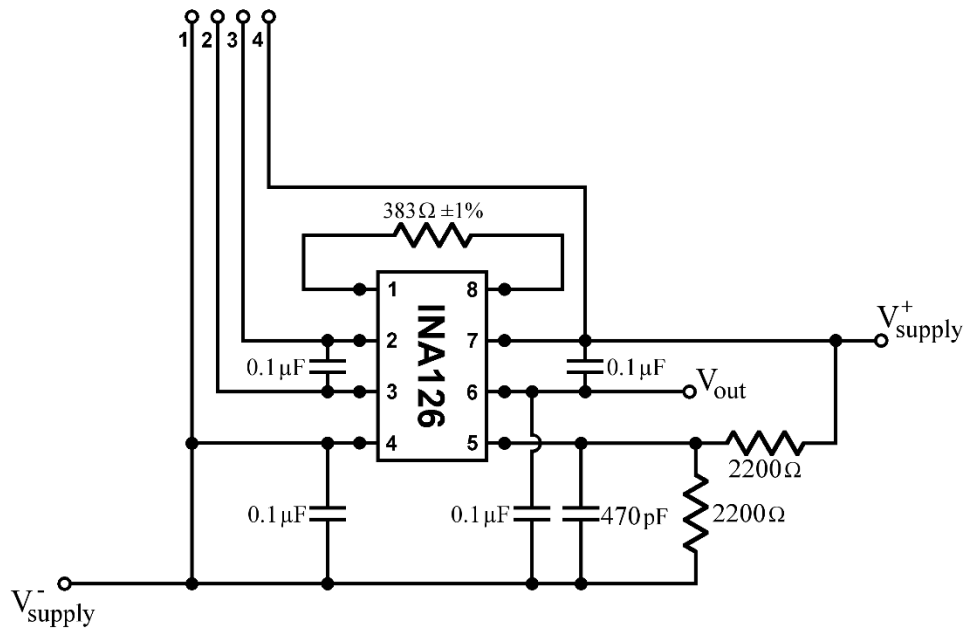
Figure 28. Op amp circuit diagram.
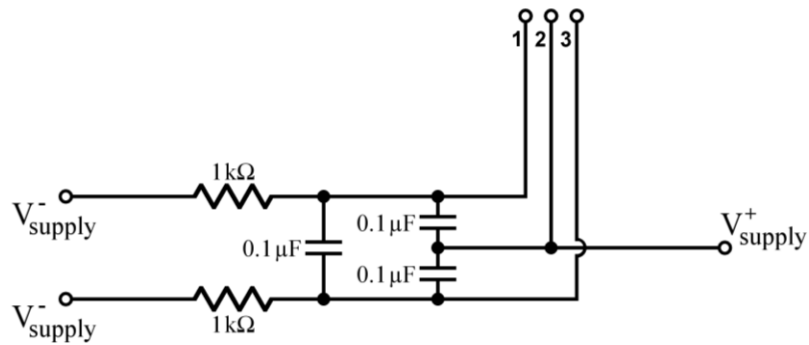
Figure 29. Potentiometer circuit diagram.

The conditioned analog signals were then fed into the DAQ, along with one channel of

identifier info for the load cell, used in the LabVIEW program to set the calibration factors for

the specific load cell currently in the system. Several channels of the DAQ's digital outputs were

used to send control signals out for the motor, one for motor on/off, one for direction, and 6 bits

51

of digital data for the pulse generator to set the stepper frequency. With all of the electronics in place, design moved to final stage, the LabVIEW control program.

2.2. Software Design

The control program is responsible for a significant portion of the load stage functionality. A portion of this effect is due to the limits, both intended and unintended, that the control program imposes on the load stage functionality. The software also affects how users interact with the load stage. The main aspects of the control system design, LabVIEW implementation, and test functionality are discussed in this section.

2.2.1. Control Process

The control process used in this design encompasses the three main components: the physical system, the analog-digital interface, and the control software. The components of the controlled system, i.e. the load stage, and the interface hardware were discussed in detail in the first part of this chapter, section 2.1. Mechanical and Electrical Design. The primary functions of the control process and their interactions with one another are shown in Figure 30. The methods and flow used in the control were influenced by the use of LabVIEW programing environment, the interface hardware, and the intended system functions.
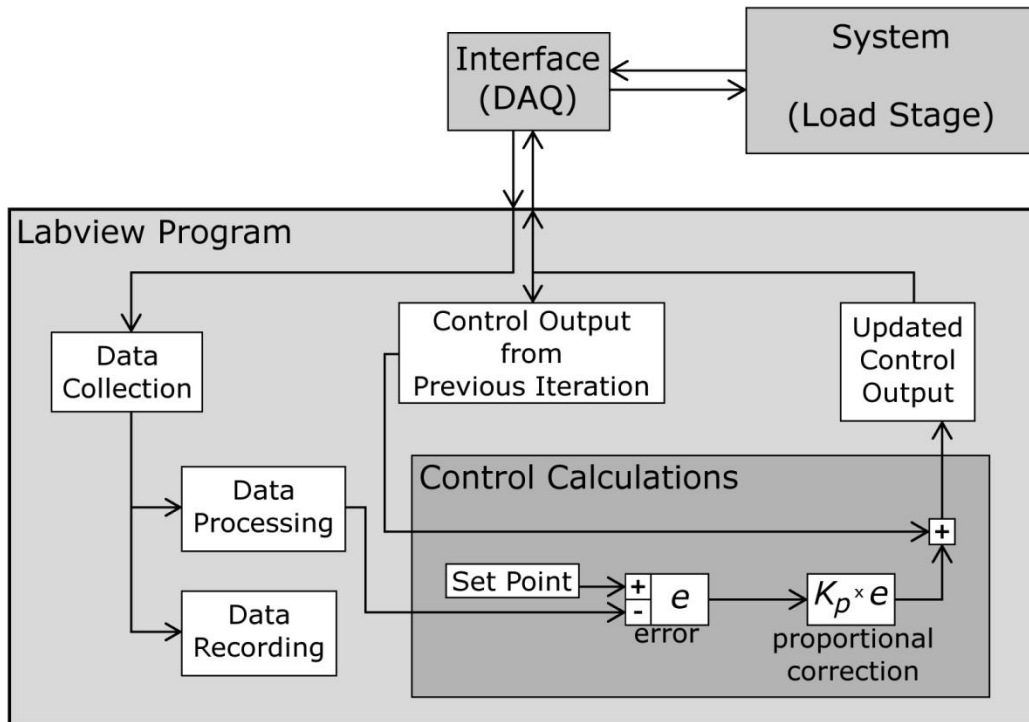
Figure 30. Control process diagram detailing primary functions and their interconnections.

2.2.2. LabVIEW Control Program

2.2.2.1. Core components

A key aspect of any test is the data it generates. This is also important for closed loop control systems. Data, as a generic component, can be viewed in several more specific component aspects dealing with collection, recording, and processing of sensor outputs from the system.

The control program must first acquire the data from the interface, in this case the National Instruments DAQ. This could be done as a continuous point collection, or by collecting data for a short burst of time, depending on the needs and the capabilities of the relevant components. The DAQ is capable of reading up to 10,000 samples per second total across all of its input channels, of which two are used in this system. This provides greater data collection

frequency capability than required for any of the intended test modes. The limiting factor then is shifted to LabVIEW's programing environment and the inability to perform tasks in parallel. This means the data points collected will be limited to single or small groups of data points separated by the unknown time interval required executing all of the other control functions required during testing, before the loop returns to collect data again. The control program then gains a direct trade off relationship between several factors which are all affected by time.

The most direct relationship is the data accuracy. As mentioned in the electronic filtering portion of the design, there is inherent background noise within any electrical system. The time related tradeoffs with data collection come in two parts, both affecting the final layer of data filtering which is implemented within the control program. Ideally a digital filter, such as a Butterworth or High/Low pass method, would be applied to the collected data set. These methods require a significant number of data points to resolve the filtered data however, and the number of required data points increases with higher order, more stable, filter implementation. The LabVIEW implementations of these methods also require data points with a consistent time increment meaning that data from one loop iteration cannot be combined with data from the next and filtered efficiently. To implement this type of method would then require a large set of data points be collected for each loop iteration, thus increasing the execution time of each control loop iteration.

The second, though arguably more important, time based tradeoff is between control execution time and system performance. The longer the control execution time is, the more the system changes before the next measurement and correction cycle. For a low displacement rate test such as a quasi-static tensile test run at 0.001 s^{-1}, three or four control updates per second is satisfactory. Higher displacement rate tests require more control updates per second lest details

become lost due to the relatively low data collection rate. For example, consider a test

monitoring the position at the tip of a beam, measuring its location once per second. In case one

the beam bends continuously under the stress of a slowly increasing load. The interpretation of

the data set, represented in Figure 31A, effectively represents the actual events. Consider a

second case now, where the tip of the beam is vibrating at a frequency of 1 Hz. The data

collected from this case would seem to indicate the beam is stationary rather than indicating its

actual vibration as illustrated in Figure 31B. While this is an exaggerated example, even if the

collection rate were 6 to 8 samples per second, the recorded data would not accurately represent

the vibrations amplitude. Thus, the control execution time determines the resolution of the

collected data, which limits the ability to test higher strain rate events.
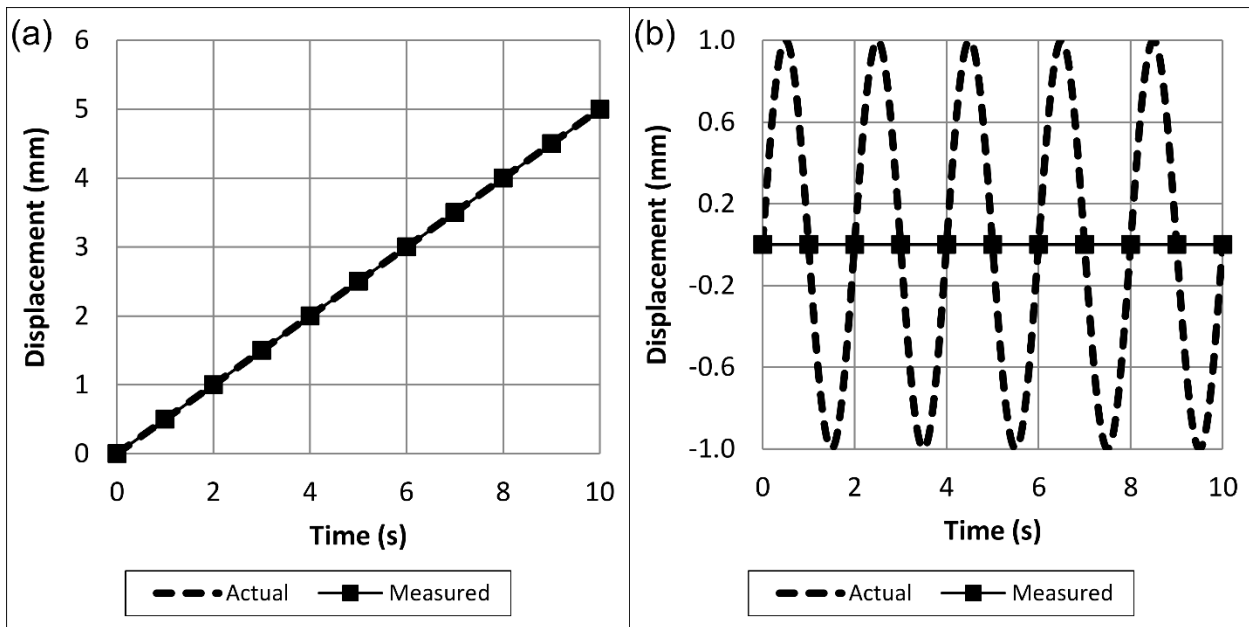
Figure 31. Actual and measured (at 1 second intervals) position at the tip of a theoretical beam under A) a continuous, slowly increasing load, B) a 1 Hz sinusoidal vibration.

Based on the design goals and component limitations, the final level of software filtering

was implemented as a rolling average of the data collected during recent loop iterations. Each

time the program collects data, it collects multiple data points at the maximum collection rate, and averages them. To further smooth the data, the new data point is averaged with the data points from the last several control loop iterations. For higher displacement rate tests, less previous iterations are used, so that the control can remain responsive to the actual operating conditions of the load stage.

Once the data is collected it must be analyzed. This is when the stress, strain and strain rate are calculated from the input force, position, and time. The program shifts the calculation method depending on the type of test being run. Once the data is analyzed the current system state can be compared to the desired state to calculate the current system error. Based on the several factors, including execution time and error fluctuation rate, the control correction was implemented as a proportional only.

Safeguards must also be included in the system. There are multiple routes available, as with most design considerations. For this project the safety and shut off limits are built into the software portion of the control system. This route was chosen for several reasons, primarily because there were no hardware requirements (i.e. additional sensors or electronic circuitry) and software limits are easier to adjust. Space savings, due to the size limitations placed on the load-stage, necessitated the minimization of hardware components incorporated into the load-stage. The dynamic limit adjustment capability held benefit in maintaining the flexibility of the system for different applications as the zero point (or collision point) varies with the alternate mounting assemblies.

The penalty for using software limiters is the risk of a software failure leaving the hardware in an active displacement state. This opens a potential risk for hardware damage through a failure in any of the three system portions, rather than limiting risk to failures in the

load-stage and interface systems. The risks of hardware damage are limited by several factors however. The load cells selected have significant overload protection and most tests are performed with a low enough displacement rate that the test operator would have sufficient time to protect the equipment. Additionally, the stepper motor driver unit is set to minimal current output to minimize vibration, which also limits the maximum torque output of the motor to a range comparable to the safe limits of both the load cell and lead screw operation.

During the programing, testing, and operation of the equipment the software was not responsible for any unintended motion, though a faulty wire in the interface system did cause the motor to engage unintended on occasion before the cause of the problem was identified and corrected.

2.2.2.2. Quasi-static control (tensile, compressive, AFM incremental)

The quasi-static control has one basic goal, to maintain a constant rate of change for the selected parameter. The particular parameter being used will depend upon the type of test being run. The available options are derived from the available sensor data; thus, parameters dependent upon force, time and position are viable. For a tensile or compressive test this sensory data provides the option to control the rate of change in force, stress, position or strain generated within a sample during testing. Control of these parameters facilitates tensile, compression, and bending quasi-static tests to be performed. The addition of an incremental check of the controlled criteria allows for hold points during testing. These hold points are a key component for AFM imaging, during any of the previously mentioned test types, as the images take time to capture. The sensitivity of the AFM to vibration, or any other sample movement or deformation requires that the motor remain stationary during imaging. These interruptions can introduce stress relaxation and other time-based effects into the measured force-displacement data due to the

length of time required to scan an image, thus the control program must account for any changes when resuming displacement. How the sample behaves during imaging pauses can affect the selection of stress or strain as the increment criteria. As AFM imaging hardware and controls improve the time required, and the resulting effects on the material will be reduced.

2.2.2.3. Dynamic control

The dynamic control process required for cyclic testing becomes more involved. This is where the time-based relationships between control execution and observable details come into play. In order to minimize the calculation requirements, the dynamic mode was implemented using the target strain rate control already in place for quasi-static testing, with a few tweaks. The number of previous iterations used in the moving averages was greatly reduced, and the strain rate was used as an absolute value so the longer-term values would not average out to zero around the cycle. Directional reversal at the cycle peak was implemented as a simple cutoff. Once the measurements exceeded the preselected limit (force, stress, strain, etc.) the motor was reversed. This kept the computational time low, but with the unfortunate trade of generating a displacement more akin to a triangular wave than a sinusoidal wave. The only dynamic testing mode developed to this point was for energy dissipation to be calculated over repeated cycles at a constant set amplitude and frequency.

2.2.2.4. User interface (UI)

The user interface is the final component of the control program, connecting the experimenter to the hardware through the software. The UI tools allow the user to set up, execute, and monitor a test from start to finish. Test parameters are setup in the bottom left. Once the parameters are set, and the system is in order the test can begin. The buttons in the upper left start the test which begins data recording and locks the setup parameters. Displacement is

initiated independently of the test execution, allowing the user to verify any necessary

components before initial displacement and to resume motion after an imaging pause interval.

The indicators in the top center light up when the program interrupts motion to indicate why the

test was paused or stopped, such as when the next imaging condition is met. The full UI screen

with components for test operation, required inputs, optional inputs, and measurement displays is

shown below in Figure 32, with a detailed view of the test parameters input window in Figure

33.
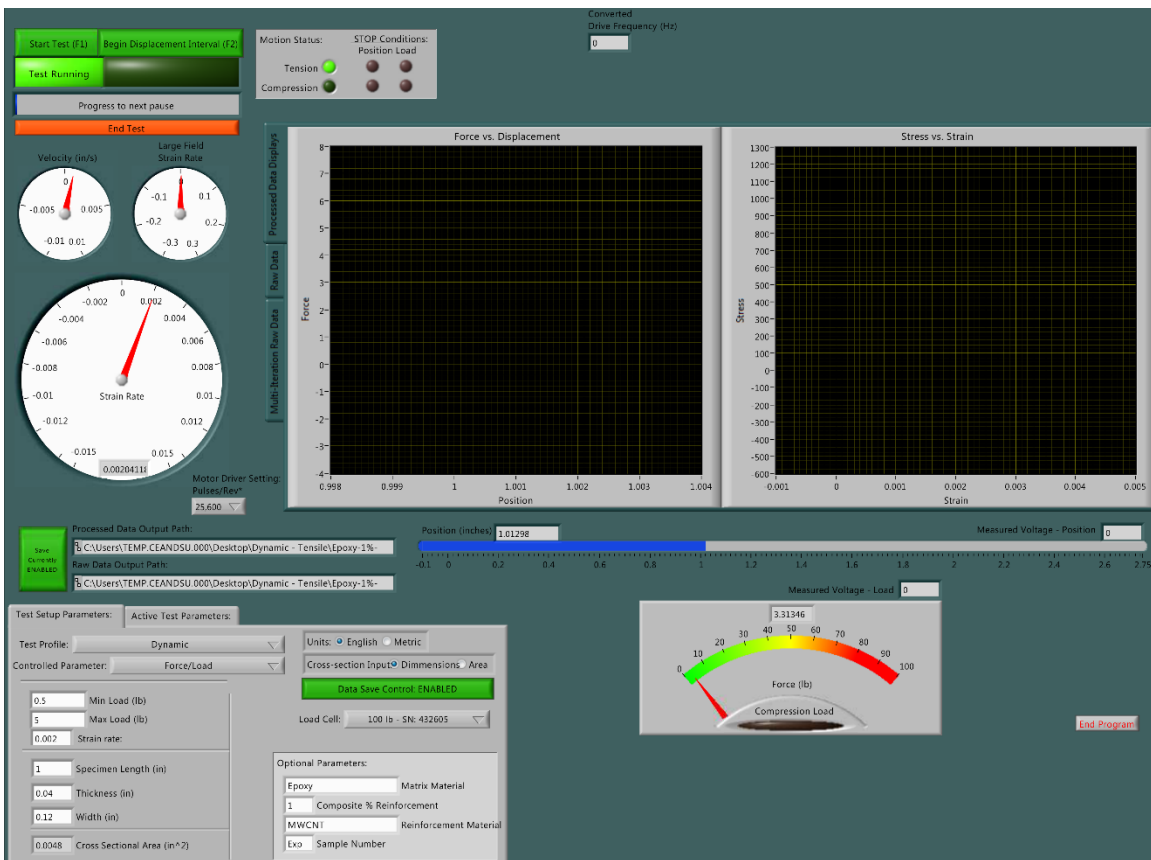
Figure 32. LabVIEW test setup and monitoring interface

Figure 33. LabVIEW UI input box

3. NANOSCALE STRUCTURAL AND MECHANICAL CHARACTERIZATION OF MWCNT-REINFORCED POLYMER COMPOSITES[3]

3.1. Introduction

Polymers have gained widespread use through their myriad properties and manufacturability. One of the challenging areas for polymers though is their low toughness [6] due to their tendency to be strong and brittle, or weak but highly deformable, thus leaving them unable to absorb appreciable energy during failure. The combination of the existing usage with specific improvement targets for expanded use makes polymers a prime candidate for composite matrices [17, 25-29]. Existing research also indicates that polymer composites with nanofillers show superior performance versus microfillers [29, 37]. CNTs are of particular interest as a reinforcement option for these composites due to their remarkable mechanical properties. CNTs are shown actually and theoretically to have tensile strengths up to 8.7×10^6 psi (60 GPa) [32], substantially stronger than steel with approximately one sixth the density.

Combining CNTs in a polymer matrix has the potential to yield a significant theoretical gain in strength over the neat polymer. Moreover, experimental data also shows enhanced damping characteristics present in CNT-Polymer composites [17]. However, the resulting composites do not demonstrate strength gains on par with the theoretical limits [22]. Therefore, it

---

3 The material in this chapter was co-authored by Wyatt Leininger, Dr. Xinnan Wang, Dr. Annie Tangpong, and Marshal McNea. Wyatt Leininger had primary responsibility for load stage design and build, sample preparation, and experimental data collection from testing and imaging. Wyatt Leininger was the primary developer of the conclusions that are advanced here. Wyatt Leininger also drafted and revised all versions of this chapter. Dr. Wang and Dr. Tangpong provided guidance and support during design and experimentation, proofread, and checked math and logic of conclusions. Marshal McNea supported sample preparation, load stage build, and proofreading. The majority of this chapter, by the listed authors, was originally published by ASME in the Journal of Engineering Materials [67] and is reused here with permission.

is important to understand the structure and mechanical characteristics present in the specimens for achieving better modeling accuracy and further refinement of the composites.

Traditional test methods including tensile, impact, and bending tests provide overall performance data for the bulk materials. Conversely, tests have also been performed to characterize properties of individual CNTs [32]. These methods all provide significant data to the understanding of the material properties, but with little detail into the complex structural mechanisms of nanocomposites. Nanomechanical characterization of polymer-CNT composites has also been investigated via nanoindentation and nanoscratch testing [27] yielding surface hardness, scratch resistance, and localized elastic modulus of the composite.

To learn about the structure's deformation under constant loading condition, the fracture mechanics, and other mechanical characteristics of any nanocomposite, it is highly desirable to "see" the deformation behavior. Imaging of bulk test specimens using optical microscopy, scanning electron microscopy (SEM), or atomic force microscopy (AFM) before and after mechanical testing provides significant insights into what the materials look like, and what features are created when they break. Analysis of this forensic data can, to an extent, hint at what happened during failure. However, to really understand how these materials behave, what structural changes occur during elastic/plastic deformation, when and where failures initiate and how they propagate, the sample needs to be observed during the loading process. The *in situ* use of microscale loading and various imaging systems have been employed to study materials including silicon [99] and polyimide films [100], predominantly for microelectromechanical systems (MEMS). Taking into account the difficulty in manipulating and testing micro/nano samples [101, 102], and the intended scale of material application, it is effective here to use larger specimens [103]. Toward this goal, a micro/nano tensile load stage has been built for use

62

with an AFM. This integration allows the observation of micro/nano structures before, during,

and after loading, as well as obtaining the stress-strain characteristics of the nanocomposite

material; in addition, it allows the correlation of the *in situ* observed structural and mechanical

characteristics with the bulk properties. This setup facilitates *in situ* observation of the material

specimens incrementally throughout the load application.

3.2. Experimental Procedures

3.2.1. Sample Preparation

Samples were prepared by casting polymer preparations in a two-part silicone mold. The

shaped side of the mold is illustrated in Figure 34. The other half of the mold was formed against

a piece of high quality flat glass to provide a smooth surface for sample surface imaging. Figure

35 shows the detailed dimensions of a dog-bone sample.
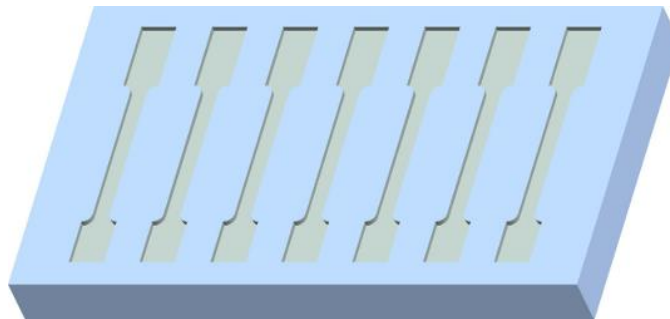
Figure 34. Schematic of the shaped side sample mold
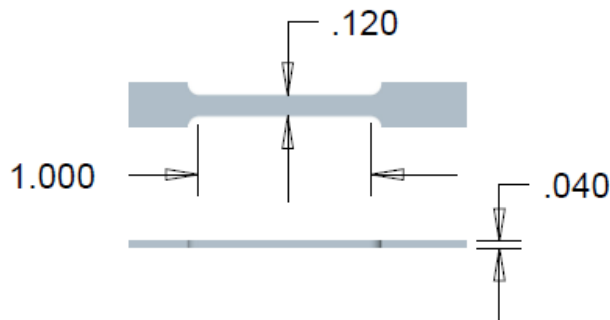
Figure 35. Critical sample dimensions (unit: in.)

The epoxy matrix used was a two-part mixture from Leco Co. with a resin to hardener volume ratio of 6.3:1. The mixture was weighed and stirred manually, and then placed in a vacuum chamber for ten minutes to remove the majority of trapped bubbles. For each batch of the epoxy mixed, one mold was filled with neat epoxy as the control sample, and another portion of the batch was manually mixed with varying weight percentages of MWCNTs (Outer diameter: 50-80 nm, Inner diameter: 5-10 nm, Length: 10-20 μm, Purity:>95%, Specific surface area: 60 m^2/g, Bulk density: 0.18 g/cm^3, and True density: ~2.1 g/cm^3, Cheap Tubes, Inc.) [36].

3.2.2. Testing Methods

The experiments were performed using an AFM (Veeco, Dimension 3100) combined with the tensile load stage, as shown in Figure 36. For these experiments, the ends of the dog-bone sample (see Figure 35) were firmly clamped. A small indicator mark was made on each sample to facilitate consistent tracking of the surface features being imaged with the AFM CCD camera. A load cell of 100 lbs (444.8 N) capacity with a minimum load sensitivity of 0.06 lbs (0.26 N) was selected for this test. A constant strain rate of 0.001 was maintained until sample failure and tensile test data was recorded continuously throughout the test.
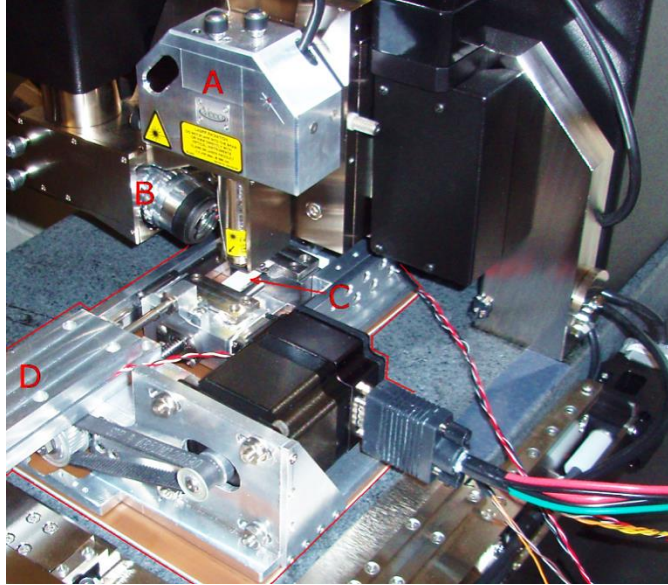
Figure 36. The micro/nano tensile load stage mounted on the AFM. A: AFM scanner, B: AFM CCD camera, C: test specimen, D: micro/nano tensile load stage.

3.3. Modeling theory

Many modeling methods exist for estimating the elastic modulus of nanocomposite [105]. The two adopted models for this study are the semi-empirical Halpin-Tsai model and the analytical Hui-Shia models (as a simplification of the Mori-Tanaka), which are commonly used in existing literature [38, 106]. The primary factor in this selection is these two models require the knowledge of only one supplementary parameter, which is the elastic modulus of the fiber (E_f), while other models require additional parameters such as the shear modulus for the Hashin-Shtrikman model or significantly more computations such as the less simplified Mori-Tanaka solutions [105].

3.3.1. Halpin-Tsai Model

The Halpin-Tsai model [57, 58] predicts the properties of a composite with randomly oriented fiber reinforcement by treating it as the mathematical equivalent of a laminate of the same components with aligned fibers, where the percentage of fibers refers to the percentage of

total fibers with the same orientation. By using this simplification, the elastic modulus of the laminate can be estimated as

$$E_c = E_m \frac{1 + \xi \eta V_f}{1 - \eta V_f} \tag{10}$$

where E_c is the estimated elastic modulus of the laminate, or the composite, E_m is the elastic modulus of the matrix, V_f represents the volume fraction of the fiber, and η is defined as

$$\eta = \frac{(E_f/E_m) - 1}{(E_f/E_m) + \xi} \tag{11}$$

where E_f is the elastic modulus of the fiber. The shape parameter, ξ, varies according to the loading direction and filler geometry. For the direction aligned with the fiber reinforcement, ξ is:

$$\xi = 2\frac{l}{d} \tag{12}$$

where l is the fiber length and d is the fiber diameter. For the transverse direction, where the fiber aspect ratio effect is weak, the effective $l/d = 1$. The same relationships expressed in Eqs. (4) and (5) can be used to find the in-plane shear modulus while setting $\xi = 1$.

The recombination of laminate layer elastic modulus estimates, such as those calculated with the Halpin-Tsai model, into an approximation for a randomly aligned fiber reinforced composite simplifies to [38]

$$E_c = 0.184 E_{11} + 0.816 E_{22} \tag{13}$$

66

where E_{11} is the longitudinal modulus of the composite and E_{22} is the transverse modulus of the composite, relative to the alignment of the fibers within the composite as shown in Figure 37. This derivation can be implemented for any composite elastic modulus model based on the aligned fiber laminate principle.
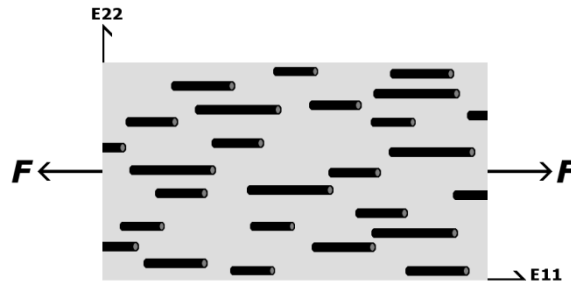
Figure 37. Schematic representation of the load (F), elastic moduli E_{11} and E_{22} orientations.

3.3.2. Hui-Shia Model

This method simplifies the Tandon and Weng [59] solution derived via the Mori and Tanaka mean field theory [60], and Eshelby's tensor [61] for the average stress in an ellipsoidal inclusion. This model uses the basis that for a given applied stress, the resultant stress within the composite's constituents deviates from the average. In turn, for the bulk material to satisfy the equilibrium condition of its current state requires that the stress variations within the reinforcement balance out on the larger scale [59]. By modeling a single ellipsoidal inclusion within an infinite matrix material, the effect of the stress disturbances in and around the inclusion can be calculated. The model can then be expanded to solve for a composite composed of uniformly aligned inclusions, provided that the volume density of the inclusions is low enough so that the disturbance of each inclusion does not interact with the any others.

In further work based on these principles, Hui and Shia [62] showed that for most cases the Poisson's ratio of the matrix and fiber had a negligible effect on predictions when compared

67

with the exact Tandon-Weng solutions. The negligible impact of the Poisson's ratio allowed Hui-Shia to use a value of $v= \frac{1}{2}$ to reduce the number of necessary calculations. This model considers the behavior of a composite with uniformly aligned fibers.

The simplification results of the elastic moduli in the longitudinal and transverse directions are [62]

$$E_{11} = \frac{E_m}{1 - \dfrac{V_f}{\gamma}} \tag{14}$$

$$E_{22} = \frac{E_m}{1 - \dfrac{V_f}{4}\left[\dfrac{1}{\gamma} + \dfrac{3}{\gamma + \Lambda}\right]} \tag{15}$$

where

$$\gamma = V_f + \frac{E_m}{E_f - E_m} + 3(1 - V_f)\left[\frac{(1 - g)\alpha^2 - \dfrac{g}{2}}{\alpha^2 - 1}\right] \tag{16}$$

$$\Lambda = (1 - V_f)\left[\frac{3(\alpha^2 + 0.25)g - 2\alpha^2}{\alpha^2 - 1}\right] \tag{17}$$

$$g = \frac{\alpha}{(\alpha^2 - 1)^{\frac{3}{2}}}\left[\alpha(\alpha^2 - 1)^{\frac{1}{2}} - cosh^{-1}\alpha\right] \qquad \alpha \geq 1 \tag{18}$$

and $\alpha = l/d$ is the fiber aspect ratio and g is a geometry-dependent factor of the inclusion. There are additional conditions which become relevant if the ratio of the elastic moduli of the

composite components is large relative to the aspect ratio of the fibers, or if the equation is applied to platelet-type reinforcement, in which cases a different calculation for g is required.

The elastic moduli given by Eqs. (14) and (15) can also be used to estimate a composite with randomly aligned fibers via Eq. (13).

3.3.3. Model Comparison

Both models require the same known parameters, while other models typically require more. This makes their estimates directly comparable as there is no additional error introduced by material or measurement fluctuation in unshared properties.

The most notable difference between the Halpin-Tsai and Hui-Shia models is the calculated composite modulus as shown below in Figure 38. Both models provide similar estimates for low aspect ratio, less than 15, fibers. For higher aspect ratios the Hui-Shia model increases at a higher rate, then flattens out near the theoretical maximum of an infinite length fiber. The Halpin-Tsai model shows a slower increase with fiber aspect ratio, thus providing the more conservative estimate of the two models.

The Halpin-Tsai model is a simplified form of Hill's generalized self-consistent model. Halpin-Tsai introduced engineering approximations and rearranged the equations from the their original form as the exact theory of elasticity to a general form suitable for design predictions [58]. The shape parameter, ξ, was further developed with experimental comparison to correlate the known parameters of a matrix and fiber, and to simplify estimation of the resulting composite properties. Hui-Shia was derived from the mathematical model of an elliptical inclusion within a uniform matrix material. This method assumes the inclusions, or fibers in this application, are far enough apart that their stress fields do not interact. Background research did not provide any guidelines on when a reinforcement may become too closely packed, thereby

69
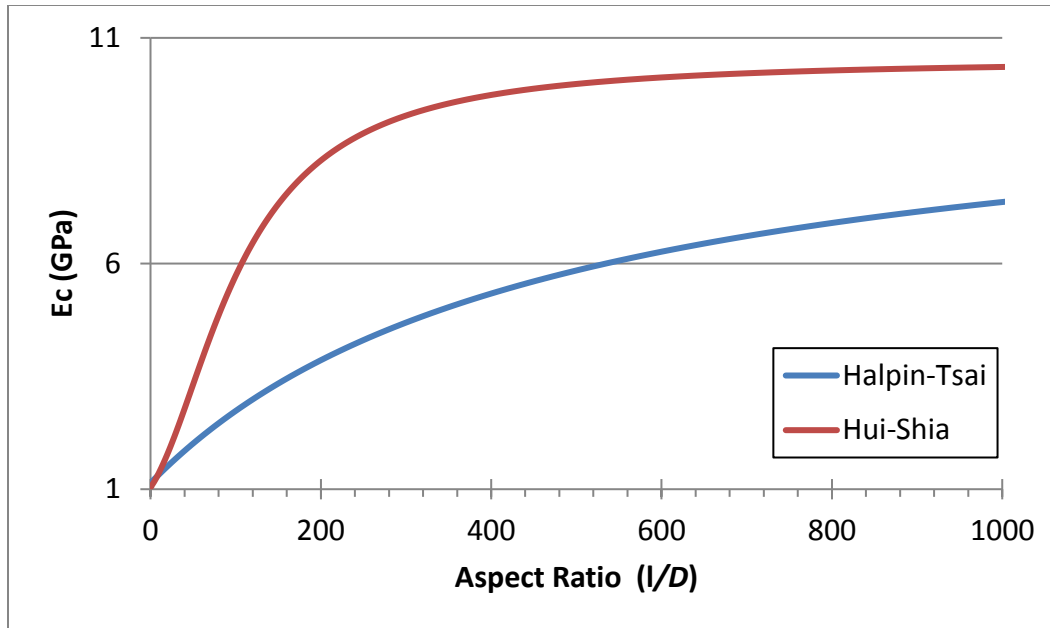
Figure 38. Composite elastic modulus values for Halpin-Tsai and Hui-Shia models vs. fiber aspect ratio, where: Em = 1 GPa, Ef = 1000 GPa, vf = 5%

causing error in the estimates from this model. Additionally, the assumption that the Poisson's ratio of the fiber and matrix where equal was used to simplify the Hui-Shia from the general form developed by Mori-Tanaka. The assumption was made after investigation showed that variation of the constituent's Poisson's ratios had little effect on the model estimates. While both models are a simplified form of their origin models, one used experimental correlations while the other used mathematical sensitivity to guide the process.

3.4. Results and Discussion

3.4.1. Sample Properties

Figure 39 shows an SEM image of a representative MWCNT of about 80 nm in diameter on the surface of a test specimen. From the samples tested under continuous strain, the elastic moduli of the neat epoxy and the MWCNT-reinforced composite were calculated. The modulus of each material was the average slope, obtained from curve fitting, of the linear portion of the

stress-strain data illustrated in Figure 40, and the results were 101 ksi (697 MPa) for the epoxy

and124 ksi (859 MPa) for the MWCNT composite.

For the modeling calculations, a value of 132 Mpsi (910 GPa) was used for the elastic

modulus of the MWCNTs [9]. The MWCNTs' volume and aspect ratio calculations were based

on the manufacturer's reported density of 2.1 g/cm^3, average diameter of 65 nm, and average

length of 15 μm. Using the elastic modulus of the epoxy samples in the Halpin-Tsai and Hui-

Shia models as E_m, the low and high range estimates of the composite's elastic modulus (E_c)

were determined. The elastic moduli predicted by the Haplin-Tsai model were 173 ksi

(1.19 GPa) and 7.86 Msi (54.2 GPa) respectively in the transverse (E_{22}) and aligned (E_{11})

directions. While the estimates from the Hui-Shia model were130 ksi (899 MPa) and859 ksi

(5.93 GPa) respectively for the transverse (E_{22}) and aligned (E_{11}) directions.

Figure 39. SEM image of a representative MWCNT on the surface of a test specimen.
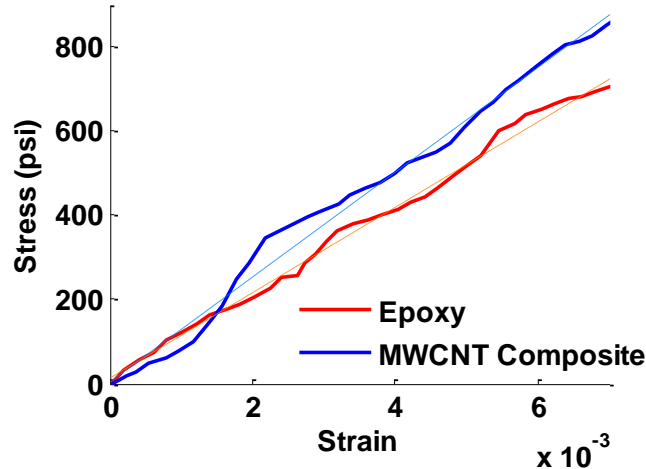
Figure 40. Representative stress-strain curves of epoxy and 1 wt.% MWCNT composite samples, with the linear curve fitting of elastic modulus. Tests were performed at a continuous strain rate of 0.001 s^{-1}.

Based on Eq.(3), the elastic modulus of a composite with randomly oriented reinforcements will be between the E_{11} and E_{22} estimates of an aligned fiber model. The fact that E_{22} estimates from both models exceeded the experimental results indicates the likelihood that additional mechanics may be affecting the mechanical properties of the composite.

The effective volume of the reinforcement differing from the actual volume may be one of the factors contributing to this discrepancy. There are several factors that can affect the effectiveness of the reinforcement by degrading the transfer of force to the fibers, including fiber-matrix interface strength, fiber dispersion, and transference of load within the reinforcement fiber. The influence of transfer between layers of a MWCNT was examined due to their use as the reinforcement fiber.

3.4.2. Effective Fiber Length

The effective fiber length concept [38] is useful for characterizing the experimental elastic modulus versus the theoretical maximum elastic modulus of the composite and is included to help refine the comparison of the elastic modulus estimates with the experimental

72

results. This concept takes into account the maximum tensile load that a fiber can sustain,

$F = A\sigma_f$, where A is the cross-sectional area of the fiber, and σ_f is the tensile strength of the fiber.

Since the load within the tube must accumulate starting from both ends to maintain equilibrium,

the maximum load will be at the half-length within a uniformly bonded straight fiber [38]. The

critical length l_c of the fiber-matrix interface required to transfer this load becomes [38]

$$l_c = \frac{\sigma_f d_f}{2\tau} \tag{19}$$

where d_f is the fiber diameter and τ is the interfacial shear stress within the composite. Assuming

there are no voids in the matrix, the actual load transferred will be limited by the stress and strain

characteristics of the matrix. This maximum transferable stress is formulated as [38]

$$\sigma_m = E_f \varepsilon_{fiber} \leq E_f \frac{\sigma_m}{E_m} \tag{20}$$

with ε_{fiber} and σ_m representing the strain of the fiber and tensile strength of the matrix

respectively. For situations where the shear transfer between the matrix and the fiber is low, the

critical length required to load the fiber effectively becomes very long.

An examination of the correlation between interfacial shear strength and the resulting

critical length for required to transfer 500 psi (3.44 MPa) is illustrated below in Figure 41. A

stress of 500 psi was chosen as an approximate median value from elastic region the

experimental data shown previously in above Figure. The examination is based on a fiber

diameter (d_f) of 65 nm, typical of the MWCNTs used in this research. This indicates that a fiber

with aspect ratio of one would require an interfacial shear strength of approximately 246 psi

(1.7 MPa) to be fully effective. As the interfacial shear strength drops the critical length

increases quickly, displaying a strong correlation between ISS and a composites ability to

transfer stress into its fiber components. This effectively illustrates the significance of ISS on the reinforcement effects of nanoscale reinforcement as well as the importance of fiber aspect ratio.

In the case of MWCNT, as used in this study, the shear transfer to the outer layer may be strong, but the inner layers are limited by their interfaces with the surrounding CNT layers. The interaction between MWCNT layers is predominated by van der Waals forces. Any defects within the layers also have the potential to contribute to additional shear transfer, though it has been observed that nanotube layers exhibit a resistance to induced defects [39]. The interlayer shear stresses have been measured as low as 7.25 psi (50 kPa), and are thus commonly considered not to share any tension loading between layers [33, 39, 40]. MWCNTs are even being pursued as low friction nanoscale bearings [43] to further illustrate the absence of significant load transfer between layers.
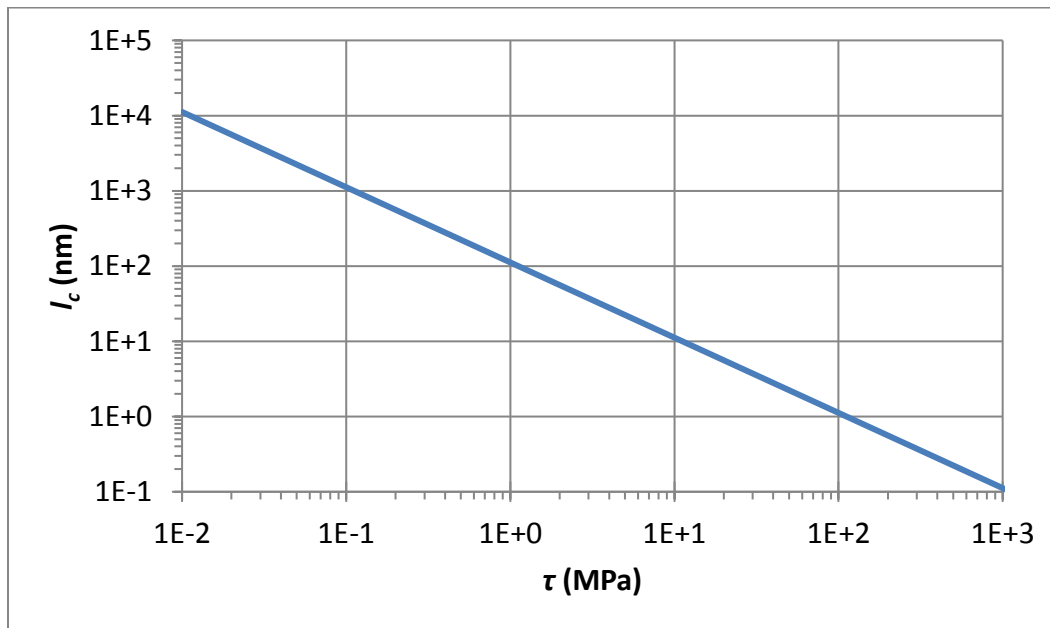
Figure 41. Relationship between interfacial shear strength (τ) and critical length (l_c).

Since the load transfer between layers in an MWCNT is very low, the critical length for the inner layers has to be much higher than that of the outer layer. As a result, the outer layer is

74

the only volume contribution of the fiber that can be expected to share significant load with the matrix. The work by Li and Chou [33] asserted that the inner layers of an MWCNT might only be deformed by direct load application.

The thickness of one CNT layer (t), an average outer tube diameter (D) of 65 nm, and the average tube length (l) of 15 μm were used to calculate the volume of a representative outer layer as $V_o = \pi Dlt$. The thickness of a graphene sheet, 0.34 nm, which is comparable to the inter-wall distance of an MWCNT [32, 34], was used for t. For a complete tube the volume was calculated using $V_T = {}^1/_4\ [\pi(D^2\text{-}d^2)l]$ where d is the average inner diameter of 7.5 nm. Combining V_o/V_T the volume fraction of bonded outer-layer CNT is found to be 2.1% of the total MWCNT volume and a new reinforcement volume fraction $V_{fo} = V_f V_o/V_T$ can be calculated. Using the outer layer volume fraction V_{fo} in the Hui-Shia model yielded longitudinal and transverse elastic moduli of 103 ksi (710 GPa) and 101.5 ksi (700 MPa) respectively for the composite, which are both effectively the same as the neat epoxy modulus of 101 ksi (697 MPa). However, using V_{fo} in the Halpin-Tsai model, the transverse and aligned elastic modulus estimates became 102 ksi (705 MPa) and 242 ksi (1.67 GPa). The experimental results of 124 ksi (859 MPa) fall between these updated model estimates of E_{11} and E_{22} for the epoxy-MWCNT composite. The evaluation of Eq. (3) yields an estimated elastic modulus of 128 ksi (882 MPa) for a composite with randomly aligned fibers, which is within 3% of our experimental results. The correlation of this estimate with the experimental results indicates that the load transfer to the inner layers of the MWCNTs is indeed negligible. Table 1 summarizes the relevant results discussed above.

Table 1. Summary of the experimental results and the refined Halpin-Tsai estimate using only the volume of the load bearing outer layer of the MWCNTs.

	Experimental		Halpin-Tsai Model
	Epoxy	1 wt.% MWCNT composite	Outer Layers Estimate
Elastic Modulus	101 ksi (697 MPa)	124 ksi (859 MPa)	128 ksi (882 MPa)

3.4.3. Deformation and Crack Patterns

Figure 42 shows a series of AFM images captured during testing, with loads applied in the y direction as indicated by the origin in the upper left corner of the figure. The strain progresses from zero in part (a) to 0.008 in part (c), just prior to failure at an overall strain of 0.0085. The AFM images provide nanoscale details of the surface of the tested sample including one of the MWCNT reinforcements highlighted as area 1 of the three images in Figure 42. The most noticeable observation of the MWCNT with increasing strain is the bending of the portion of area 1 near the top of each image. Additionally, the angle of the lower section of the MWCNT, relative to the specimen, shifts by approximately 1.1° clockwise between (a) and (c). For area 2, the outer border remains at a fixed position relative to the image frame, while the inner box tracks a surface feature as it moves down the image during loading, illustrating the overall deformation of the matrix during testing. Using points away from the MWCNT, the point-to-point strain measurements along the y-axis of the images in Figure 42 yielded a result of approximately 0.004 between images (a) and (b), and 0.006-0.01 between (a) and (c).The correlation of the point to point strain observations with the bulk material strain of 0.0035 from

(a) to (b), and 0.008 from (a) to (c) indicates nanoscale deformation of the matrix material consistent with the bulk material when not affected by the reinforcement. Therefore, the reorientation and deformation of nanoscale reinforcements within a composite, as well as the localized matrix strain, can be observed with this system.
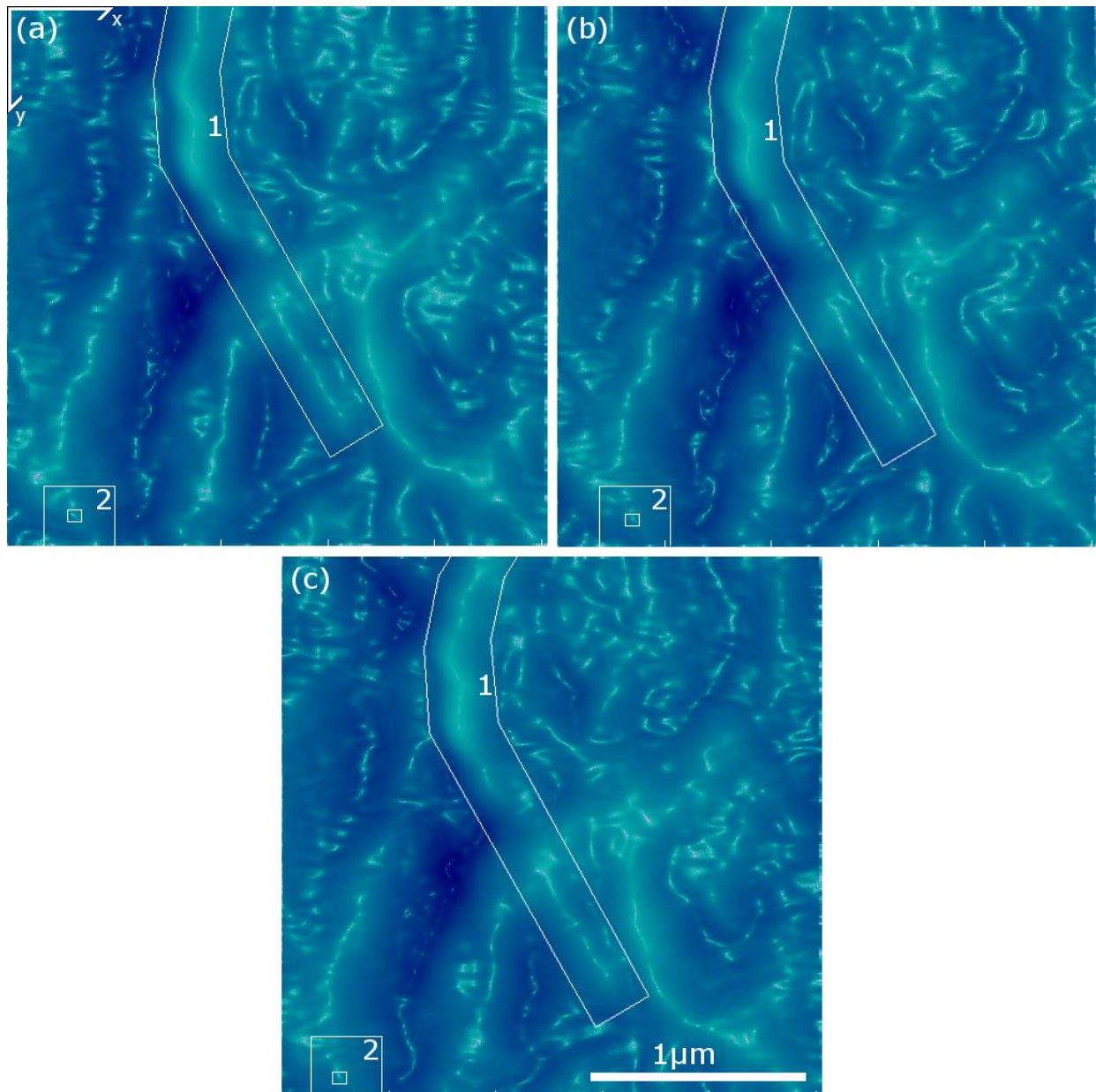
Figure 42. AFM amplitude images of MWCNT composite sample at varying degrees of deformation. The origin in the upper left represents the features used to reference images at each applied strain interval.(a) strain: 0, (b) strain: 0.0035 and (c) strain: 0.008.

Figure 43 shows a post failure view of the crack propagation through a neat epoxy sample (a), and through an MWCNT reinforced sample (b). The images show smooth crack propagation across the neat sample, while the crack path was rougher on the MWCNT reinforced sample, indicating a change in the crack propagation mechanism between the neat and composite samples. Figure 44 shows two AFM images of an induced crack within a composite sample, with Figure 44(a) being shortly after the crack initiation and (b) illustrating the same location after further crack propagation. As shown in Figure 44(a), the initial crack progressed to the highlighted section, though after further crack progression as seen in Figure 44(b), the crack path has deviated around the features that ended the initial crack propagation. The fact that the crack in the reinforced sample took a path around this structure could be an indication that a sufficient reinforcement effect altered the crack propagation pattern. This alteration in the crack path would result in increased energy required for crack growth, thus toughening the composite.
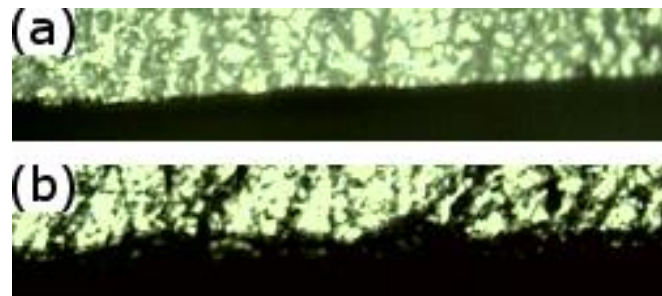
Figure 43. Post fracture paths of (a) a neat epoxy sample, and (b) an MWCNT-epoxy sample captured by the AFM CCD camera with a magnification of 800X.
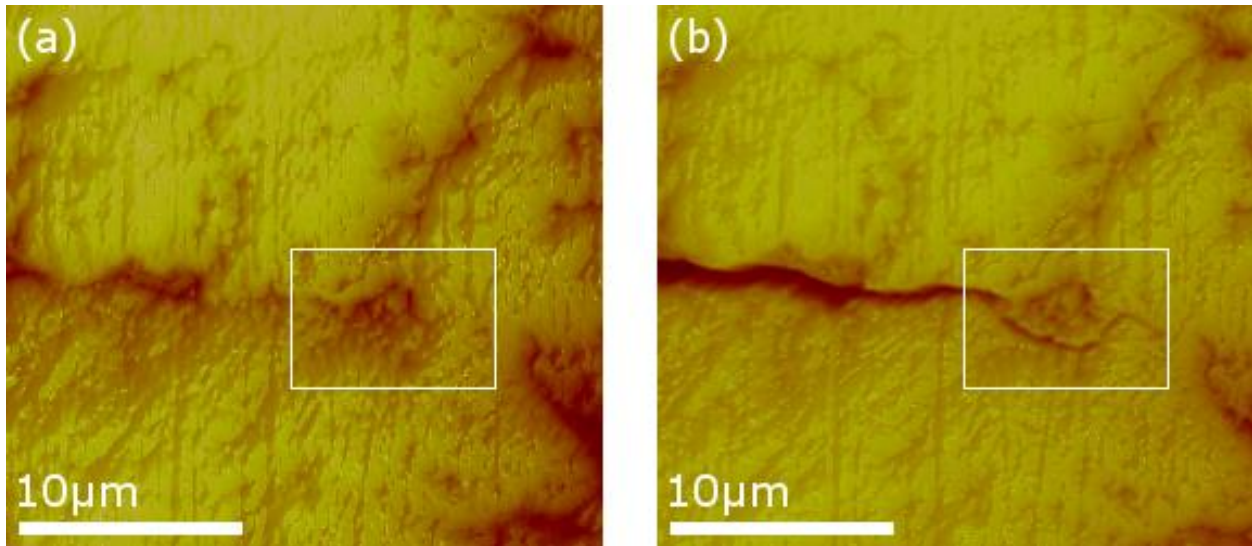
Figure 44. (a): A newly initiated crack within the sample, ending within the highlighted region indicated. (b): Crack progression from (a) after strain increase, showing a deviation around features present at the end of the crack in (a).

3.5. Conclusion

The micro/nano characterization of an MWCNT-polymer composite was investigated using an AFM and an in-housed designed micro/nano tensile load stage. The nanocomposite's deformation and MWCNT reorientation were observed on the surface and the values of strain were calculated from the images, which were in agreement with the bulk strain measurements. The elastic modulus of the epoxy-MWCNT composite was discussed in conjunction with the load transfer ability between layers of an MWCNT. Results show that the elastic modulus of the MWCNT reinforced nanocomposite increased by 23% compared to that of the pure epoxy. The Halpin-Tsai and Hui-Shia models were used to estimate the nanocomposite's elastic modulus, and the Halpin-Tsai results were found to correlate well with the experimental results when only the load bearing outer layer of the MWCNT was considered, while the Hui-Shia results failed to match the experimental values. The adjustment to use only the MWCNT outer layers as a correction factor in the models was based on the correlation between ISS and critical length. Due to the low ISS between tube layers of the MWCNT the critical length of the inner layers was

79

substantially higher than the outer layer, indicating they made up a negligible portion of the reinforcement load carrying capacity. The deviation of the Hui-Shia model estimates from the experimental results could be due in part to the non-uniform distribution of the reinforcement fibers in the tested specimens, as insufficient fiber spacing violates a primary assumption of this model that the stress fields of each inclusion is independent. Furthermore, the load stage/AFM combination proved able to capture the deformation changes occurring on the sample, even for small strain increments, as well as the propagation of cracks during loading. Based on the collected data and correlations observed with the existing model, it is concluded that the designed equipment is suitable for *in situ* observation of micro/nano structural mechanics while also capturing bulk tensile and compressive properties including ultimate tensile strength, strain at failure, and strain rate sensitivity effects.

4. EFFECTS OF MWCNT REINFORCEMENT ON QUASI-STATIC AND DYNAMIC TENSILE PROPERTIES OF EPOXY[4]

4.1. Introduction

Structural damping has applications across many engineering fields such as protecting the components of a helicopter from rotor vibrations [8], isolating the motion of a vehicle from the road contours [9], reducing environmental noise [5], or minimizing crash impact [6]. In large stationary structures such as buildings and towers [11], cost and overall performance are the concerns for damping implementation, and thus dedicated damping systems, such as tuned mass dampers [10], will likely remain dominant in these areas. However, the more compact or mobile the product, such as a hard disk drive [7], the more factors such as size and weight matter. Among the commonly used current damping treatments is the application of viscoelastic polymer tape to the existing system components [13]. Though this method provides functional damping characteristics, it also increases the weight and volume of the system. Additionally, the viscoelastic tapes are prone to de-bonding [14]. When damping is incorporated by adding components such as shock absorbers, rubber grommets or viscoelastic tape, the total complexity, mass and volume of the system increases relative to a product where the structural components already provide the damping. These characteristics complicate the structure and increase the

---

[4] The material in this chapter was co-authored by Wyatt Leininger, Dr. Annie Tangpong, and Dr. Xinnan Wang. Wyatt Leininger had primary responsibility for sample preparation, and experimental data collection from testing and imaging. Wyatt Leininger was the primary developer of the conclusions that are advanced here. Wyatt Leininger also drafted and revised all versions of this chapter. Dr. Wang and Dr. Tangpong provided guidance and support during experimentation, proofread, and checked math and logic of conclusions. Portions of this chapter, by the listed authors, were originally published by SAGE in the Journal of Composite Materials [107] and are reused here per SAGE's thesis policy.

maintenance requirements of the system. Thus, simplification of a system via inclusion of damping within the primary component materials is highly desirable across a wide range of applications.

Composites offer a route for system simplification because of their ability to tune the final material properties, similar to the alteration of metals via alloying. Due to their high manufacturability, range of available properties and widespread use, polymers make excellent choices for composite matrices. Composites with nanoreinforcements have been found to outperform their counterparts made with micro or larger scale reinforcements [29, 37]. Since the ideal solution is to incorporate the system damping requirements into the structural components with limited or no weight or volumetric penalties, the filler material should have a higher strength to weight ratio than the matrix. Typical solid polymer densities range from 1 to 2 g/cm^3 [30], while the upper limit of solid material density is above 20 g/cm^3 for some metals [31]. If the low density of the polymer is to be maintained by a composite structure, however, constraints are imposed on the reinforcement selections. Nanoreinforced composites could include 10 wt.% fillers or more, though 1-3 wt.% is a typical range [16]. Within the typical range of reinforcement content, the effect of filler density on the composite density will be limited. For example, an estimate made with rule of mixtures using 3 wt.% reinforcement indicates the density of the reinforcement could be 4.3 times greater than that of the matrix while limiting the increase in the density of the final product to less than 10%. Taken together, these factors indicate that nanoreinforcements may hold a solution for combining the desired functions into a single composite material.

Research has shown that CNT reinforced polymer composites exhibit improved energy dissipation when compared to their neat polymer counterparts [17, 18]. The ability to improve

damping, combined with their high tensile strength and elastic modulus, up to 60 GPa (8.7 Mpsi) and 910 GPa (132 Mpsi), respectively [32], makes CNTs a desirable reinforcement as they have the potential to increase the overall structural performance. Experimental evidence indicates that the stick-slip mechanism [20, 68, 69] along the CNT-matrix interface is responsible for the internal energy dissipation present in the material. Composite mechanics are affected by a number of properties including the fiber aspect ratio and CNT dispersion. Chen *et al.* [72] found in their theoretical analysis of spherical particle composites that there was a critical particle diameter with a peak energy dissipation where the dominant factor changed. The critical point occurred when the increased stress required for interfacial slip outpaced the increase in particle surface area, as both factors were proportional to the reduction in particle size. Additionally, as the stress transfer at the interface increased, the critical diameter for peak damping decreased. It is possible to transfer more stress across an interface along the length of a high aspect ratio particle [38], such as a CNT, making it easier to reach the interfacial slip stress and increase the composite's internal energy dissipation.

The use of these CNT-polymer composites materials for inclusive structural damping requires a comprehensive study of the given material, since the mechanical properties directly affect the intrinsic damping performance, particularly at lower strain amplitudes. The goal of this research was to further investigate the correlation between the mechanical property varying effect from the different reinforcement loading level and dynamic mechanical properties of CNT-polymer composites through quasi-static and dynamic mechanical tests. The elastic modulus, toughness, loss modulus, and glass transition temperature of neat epoxy with composites of 0.2 wt.%, 0.6 wt.% and 1 wt.% MWCNTs are measured using an in-house designed load stage and a DMA.

4.2. Experimental Procedures

4.2.1. Sample Preparation

The epoxy used was a slow cure two-part laminating formulation from Illstreet Composites with a 2:1 ratio by volume of resin to hardener. The MWCNTs used were obtained from Cheap Tubes, Inc. (Manufacturer reported properties: Outer diameter: 50-80 nm, Inner diameter: 5-10 nm, Length: 10-20 μm, Purity: >95%, Specific surface area: 60 m^2/g, Bulk density: 0.18 g/cm^3, and True density: ~2.1 g/cm^3) [36].

The composite samples were prepared by thoroughly stirring the as received MWCNTs into the epoxy resin, then suspending the sealed container in an ultrasonic bath. Ultrasonication was performed with a bath temperature of 35 °C for 45 minutes. The elevated ultrasonic bath temperature was used due to the relatively high viscosity of the epoxy resin. For the composite and neat samples, the hardener was added, stirred and placed in the ultrasonic bath for 10 minutes on the degas setting to remove bubbles incorporated during mixing. The final mixture was then poured into two-part silicone molds to cure. Nominal sample dimensions are shown in Figure 1. Samples were allowed to set for a minimum of 5 days to ensure complete curing before testing.
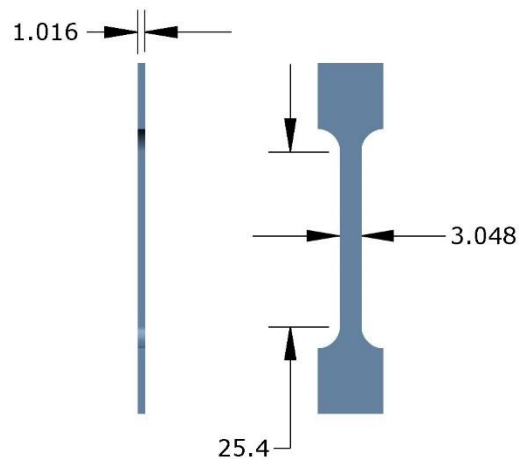
Figure 45. Material test sample geometry with key dimensions. (units: inches).

4.2.2. Quasi-Static Tensile Testing

Using an in-house designed load stage [67], quasi-static tensile tests were performed on ten samples of each type, neat, 0.2, 0.6 and 1 wt.% MWCNTs, with a strain rate of 0.001 s^{-1} at room temperature. The tests were performed using a 445 N (100 lb) load cell with a minimum sensitivity of 0.26 N (0.06 lb). The position measurement provides a minimum sensitivity of 1.3 μm (5x10^{-5} in). All samples were strained to failure.

4.2.3. Dynamic Mechanical Analysis

The DMA tests were performed in tensile mode on a DMA Q800 manufactured by TA Instruments. All tests were run with air atmosphere. The temperature for isothermal test was standardized at 30 °C; slightly above the maximum observed room temperature to maintain consistency.

To characterize the damping properties, such as loss modulus of the materials, each sample was run through a two-pass frequency sweep after mounting to stabilize the temperature and response with respect to time. The stabilization time was required to minimize inclusion of the changes in measured storage and loss moduli observed at the beginning of DMA testing. The changes were induced by the initial loading stresses and cyclic break in of the material [74]. Samples were then run through three successive constant frequency and variable force sweeps starting from 0.5 N and increasing to 8.5 N drive force amplitude at both 7.5 Hz and 50 Hz. 7.5 Hz was selected due to the irreproducibility of measurements taken at lower frequencies, and 50 Hz was selected arbitrarily. For both frequencies, test results were averaged across three stress sweeps per sample and three samples per material set. The range of the drive force amplitudes produced stress amplitudes from 0.1 MPa to 2.4 MPa, and generated material strains from 0.01% to 0.2%.

Thermal dependency information, including T_g, for the materials was gathered by running the samples run though a temperature sweep from 30 °C to 150 °C. The heating rate was 5 °C/min with constant displacement amplitude of 5 μm and frequency of 10 Hz.

4.3.   Results and Discussion

4.3.1.   Quasi-Static Tensile Properties

Figure 46 shows a typical quasi-static tensile stress-strain curve, from which key mechanical properties, such as the elastic modulus (E), toughness (u_t), ultimate tensile strength (UTS), and failure strain (ε_f) were calculated and plotted in Figure 47. The percent change of the reinforced sample properties relative to the neat epoxy properties is summarized in Figure 48. The results are discussed in the following subsections and summarized in Table 2.
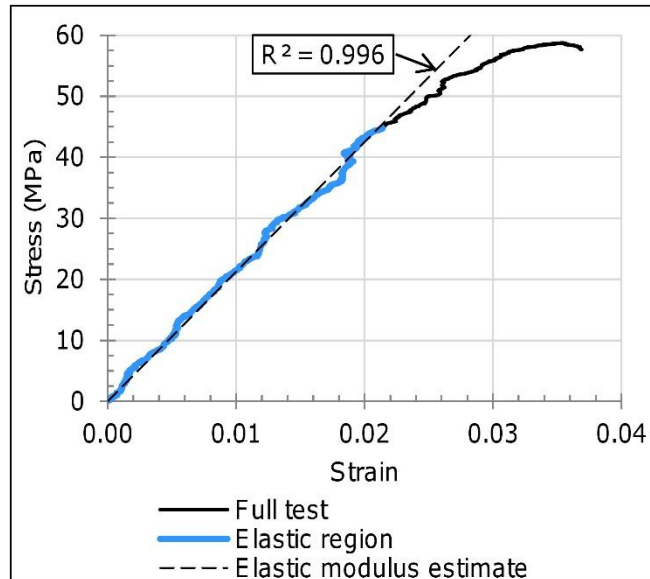
Figure 46. Stress-strain curve from a 1 wt.% MWCNT sample with highlighted region showing the data points used in the linear regression of the elastic modulus estimate.

4.3.1.1. Elastic modulus

The elastic modulus was obtained from the linear segment of the stress-strain curves for each sample as shown in Figure 2. The neat epoxy samples yielded an average elastic modulus of 1.99 GPa (290 ksi). The elastic modulus exhibited a positive correlation with increasing MWCNT content in the sample, resulting in 2.05 GPa, 2.11 GPa, and 2.2 GPa for the 0.2 wt.%, 0.6 wt.%, and 1 wt.% MWCNT materials, respectively. The standard deviation of the elastic
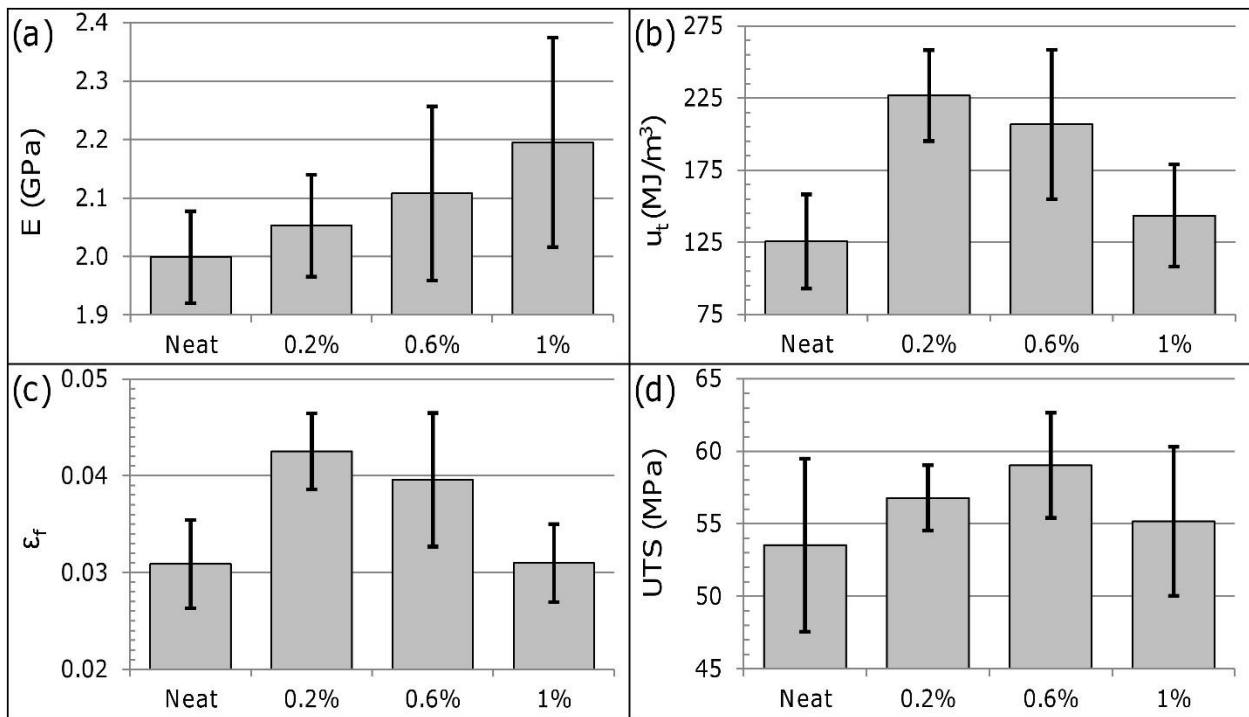
Figure 47. Average values with standard deviations for: (a) elastic modulus, (b) fracture toughness, (c) strain at failure, (d) ultimate tensile strength.
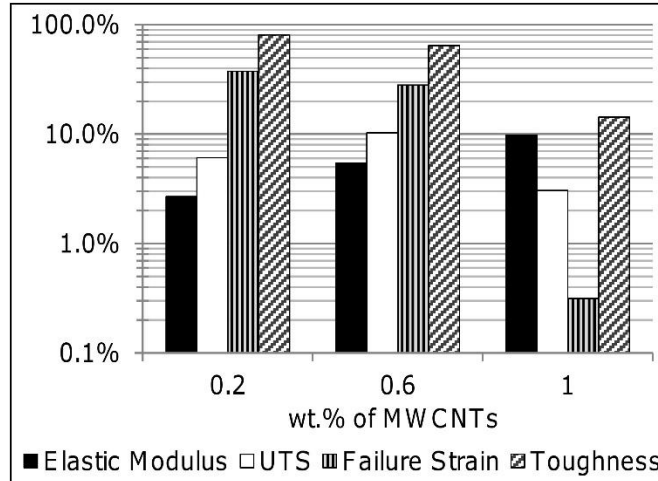
Figure 48. Percentage change in tensile properties for each MWCNT-reinforced sample set compared to neat epoxy.

modulus results also increased with MWCNT content from slightly below 4% for the neat

samples to 8.2% for the 1 wt.% MWCNT samples. The correlation between property variability

and reinforcement content indicates a reduced material uniformity, such as filler dispersion,

related to the change in reinforcement levels. The variations in dispersion as can be seen in

Figure 49 by comparing the even color distribution within the 0.2 wt.% material with the dark

clumps of MWCNTs within the 1 wt.% specimen.

Table 2. Summary of quasi-static tensile test results.

Material		Neat	0.2%	0.6%	1%
Elastic Modulus	E (GPa)	2.00	2.05	2.11	2.20
	STDV (GPa) / %	0.08 / 3.94%	0.09 / 4.24%	0.15 / 7.06%	0.18 / 8.17%
	% increase vs. neat	-	2.7%	5.5%	9.8%
Strain at Failure	ε_f ($^{mm}/_{mm}$)	0.0309	0.0425	0.0396	0.0310
	STDV ($^{mm}/_{mm}$) / %	.0046 / 14.8%	.0039 / 9.3%	.0069 / 17.5%	.0040 / 13%
	% increase vs. neat	-	37.7%	28.2%	0.3%
Ultimate Tensile Strength	UTS (MPa)	53.5	56.8	59.0	55.2
	STDV (MPa) / %	6.0 / 11.1%	2.3 / 4%	3.6/6.1%	5.1 / 9.3%
	% increase vs. neat	-	6.1%	10.3%	3.1%
Toughness	u_t (MJ/m³)	125.6	226.7	206.7	143.6
	STDV (MJ/m³) / %	32.6 / 26%	31.5 / 13.9%	51.8 / 25%	35.4 / 24.7%
	% increase vs. neat	-	80.6%	64.6%	14.3%
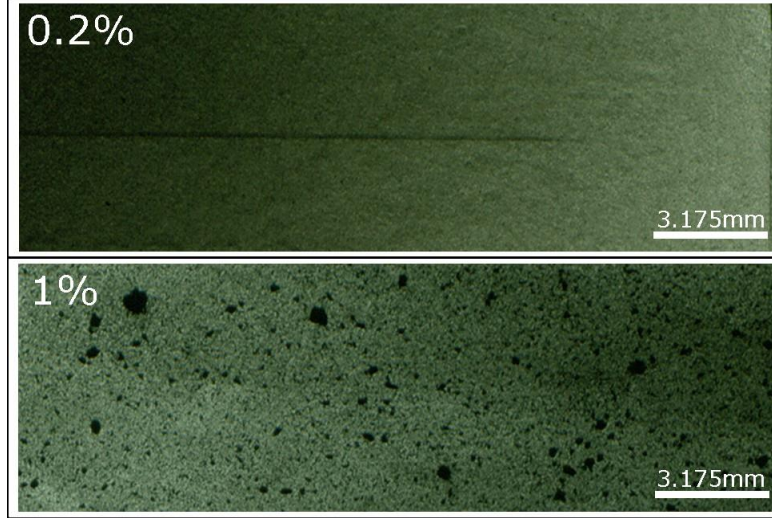
Figure 49. Image of thin specimens from the 0.2 wt.% (top) and 1 wt.% (bottom) MWSNT epoxy materials showing the clumping of the MWCNTs at increased concentration.

The addition of the MWCNTs increases the elastic modulus from 2.7% in the 0.2 wt.% MWCNT set to over 9.8% in the 1 wt.% composite. As shown in Figure 6, the relationship between elastic modulus and wt.% MWCNTs content is linear and is estimated by

$$E = 19.44x + 1.999 \tag{21}$$

where E is in GPa and x is the wt.% MWCNTs.

The elastic moduli of the composites are estimated using the Halpin-Tsai model [57, 58].

$$E_{xx} = E_m \frac{1 + \xi_{xx} \eta_{xx} V_f}{1 - \eta_{xx} V_f} \tag{22}$$

$$\eta_{xx} = \frac{(E_f/E_m) - 1}{(E_f/E_m) + \xi_{xx}} \tag{23}$$

$$\xi_{11} = 2\frac{l}{d} \qquad \xi_{22} = 2 \tag{24}$$

$$E_c = 0.184E_{11} + 0.816E_{22} \tag{25}$$

where E_c is the elastic modulus estimate of the composite, E_{11} and E_{22} are the aligned and transverse elastic moduli, respectively, of an aligned fiber composite of the same materials, E_m and E_f are the elastic moduli of the matrix and filler, respectively, V_f is the volume fraction of the filler, l is the length of the filler and d is the outer diameter of the filler. Using 910 GPa (132 Msi) as the elastic modulus of the MWCNTs, the model calculations estimated an elastic modulus improvement approximately twice that of the experimental results. Using only the volume of the outer layer of the MWCNTs as the filler volume [67] in the model also yielded an elastic modulus which was not comparable to the experimental results. The resulting elastic modulus estimates from this method where negligibly higher than measurements of the neat epoxy and well short of the experimental increases seen in the reinforced samples. One possible explanation is that the original MWCNT length changed during sample preparation. Research shows that CNT breakage during processing [52] is a possibility, and an expected occurrence during ultrasonication [46, 47, 53]. The aspect ratio of the MWCNTs used in the Halpin-Tsai model would be approximately 60 to yield estimates similar to the experimental elastic moduli. To achieve this aspect ratio, assuming a constant MWCNT diameter, the average MWCNT length post fabrication would be 3.9 μm, approximately 25% of the original 15 μm average length. Another possible explanation is that the elastic modulus used for the MWCNTs does not match their actual properties as it is shown that MWCNT properties are particularly dependent on manufacturing processes [35]. Maintaining the original CNT dimensions and using an MWCNT elastic modulus reduced by one quarter, to 227 GPa (33 Msi) also yielded Halpin-Tsai model estimates comparable to the experimental results.
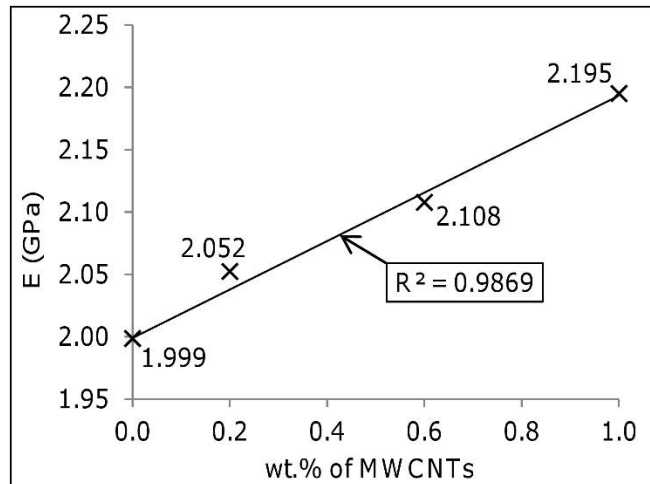
Figure 50. Linearity of the relationship between the elastic modulus and the wt.% MWCNTs.

4.3.1.2. Ultimate tensile strength

The ultimate tensile strength of the neat sample set was 53.5 MPa (7.77 ksi) with a standard deviation of 5.96 MPa (0.86 ksi), just over 11% variation. For the 0.2 wt.% set there was the expected increase in UTS with the addition of reinforcement, bringing this set to 56.8 MPa (8.24 ksi). Additionally, there is a noticeable drop in the standard deviation of the UTS, from 5.96 MPa (0.86 ksi) for the neat samples to 2.52 MPa (0.37 ksi) for this set, bringing the variation to less than 4%. The UTS then increases to 59 MPa (8.56 ksi), but falls to 55.2 MPa (8.01 ksi) for the 0.6 wt.% and 1 wt.% samples sets respectively. The standard deviation increases to 6.2% and 9.3% for these samples sets.

The distinct drop in UTS variation between the first two sets with the addition of minimal reinforcement strongly suggests that the reinforcement reduces the effects of minor flaws within the samples. The high variation of the neat sample set also highlights precisely how susceptible unreinforced epoxy is to crack propagation. The successive increase in variation with increases in MWCNT content, above the 0.2 wt.% used in the second set, are also likely due to the increasing difficulty of dispersing the reinforcement into the epoxy.

91

4.3.1.3. Strain at failure

The average strain at failure (ε_f) for the neat samples was 3.09%, with a standard deviation of 0.45%. Visual inspection of the failed samples showed negligible deformation as shown in Figure 51A, which is consistent with the shape of the stress-strain curves for the set. The samples show the greatest increase in ε_f with the addition of minimal reinforcement. The result is an ε_f of 4.25% for the 0.2 wt.% samples while maintaining a similar standard deviation of 0.39%. The fractured sample shown in Figure 51B, however, shows a significant difference: prior to failure, there is noticeable deformation as evidenced by the shear slip lines visible around the failure point which resulted in small, but measurable, cross-sectional area reductions for the 0.2 wt.% samples set.

Further increases in the MWCNT content reduce the ε_f to 3.96% and 3.1% for the 0.6 wt.% and 1 wt.% samples sets, respectively. The standard deviation for the 1 wt.% samples remained similar with a value of 0.40%, while the 0.6 wt.% set produced a standard deviation of 0.69%. Inspection of the 0.6 wt.% samples revealed a behavioral split as only part of the sample set exhibited visible slip lines after failure. This variation in plastic deformation pre-failure would account for the increased variation within this sample set. The 1 wt.% samples uniformly demonstrated no visible plastic deformation post failure, comparable with the neat samples.
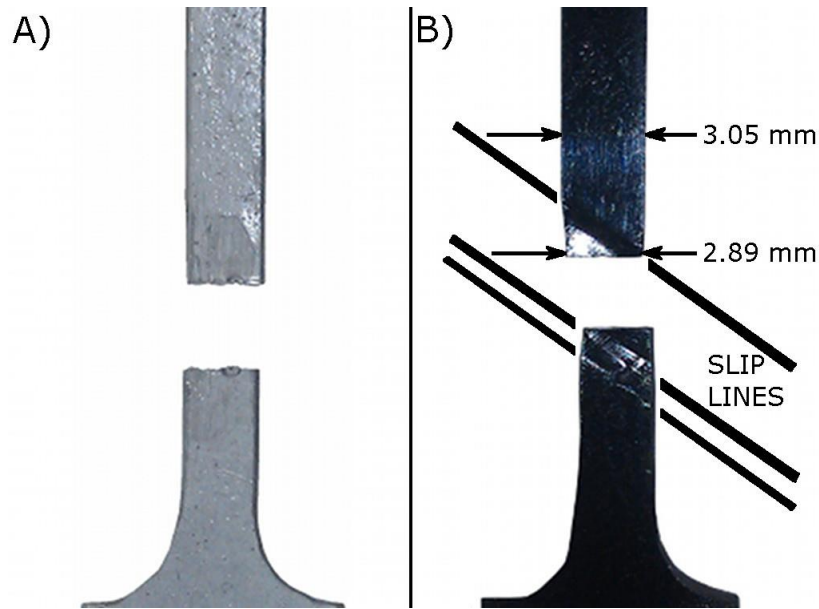
Figure 51. (a) Neat sample post fracture and (b) 0.2 wt.% MWCNT sample post fracture. Note the plastic deformation and width reduction around the fracture on the reinforced sample (b).

4.3.1.4. Toughness

The lowest modulus of toughness (u_t) is seen in the neat epoxy, as expected based on it also having the lowest UTS and ε_f. Average u_t of the neat sample set is 125.6 MJ/m^3 with a standard deviation of 32.7 MJ/m^3, which is a variation of approximately 26%.

With the addition of MWCNT reinforcement there is a substantial initial increase in u_t for the 0.2 wt.% set yielding 226.8 MJ/m^3, an 81% increase over the neat epoxy. The u_t follows a trend similar to the failure strain, since the variation in ε_f between sample sets is generally greater than the UTS variation. The resulting u_t for the 0.6 and 1 wt.% MWCNT samples is 206.8 MJ/m^3 and 143.6 MJ/m^3, respectively. With the exception of the 0.6 wt.% set, which produced a standard deviation of 51.8 MJ/m^3, the standard deviation for u_t remained in the 30-35 MJ/m^3 range. Conversely, looking at the standard deviation as a percentage of the u_t then the 0.2 wt.% set is the exception with a value of approximately 14% while the other material sets stayed in the 24-26% range.

4.3.1.5. Statistical analysis

Confidence intervals were calculated for all of the experimental parameters to estimate the reliability of the sample set. The calculations used the average and standard deviation values found previously combined with the number of samples and values from a standard T score table. The resulting intervals with the population mean are shown below in Figure 52.

Of the experimental parameters shown, the elastic modulus has narrowest confidence interval based on percent variation, thus the highest reliability. The 95% confidence interval for the elastic modulus was found to be ±2.6% for the neat epoxy, and increased with increased MWCNT content to 5±.2% for the 1 wt.% MWCNT reinforced epoxy. This is significant as the high value of the neat epoxy range is lower than the low value of the 1 wt.%, thereby indicating with 95% confidence that a new set of samples would show the same trend that the composite elastic modulus increases with MWCNT content.

The confidence intervals for stress had a slightly larger range. The narrowest 95% confidence interval for the ultimate tensile strength was found to be ±3.3% for the 0.2 wt.% MWCNT-epoxy, followed by the 0.6 wt.% samples with ±4.4%, the Neat samples with ±8.6%, and the widest interval of ±9.8% for the 1 wt.% MWCNT reinforced epoxy. While the intervals are wider than those of the neat epoxy, one can see from Figure 52(d) that the increased UTS seen with increasing MWNCT content from 0 to 0.6 wt.% remains a likely outcome, while the drop off seen in the 1 wt.% samples was less certain as indicated by the increased range of the confidence interval.

The percent property variation for strain at failure and fracture toughness are higher than those discussed above, ranging from 8.5% to 40.6%. These intervals alternately provide greater value as visual indicators in graphs (b) and (c) found in Figure 52. Looking at the range bars

94

representing the confidence intervals for both of these parameters shows that a different sample set is still likely to produce the same basic outcome with the 0.2 wt.% MWCNT reinforced samples showing a significant increase over the neat epoxy, with benefits dropping off as MWCNT content increases further.
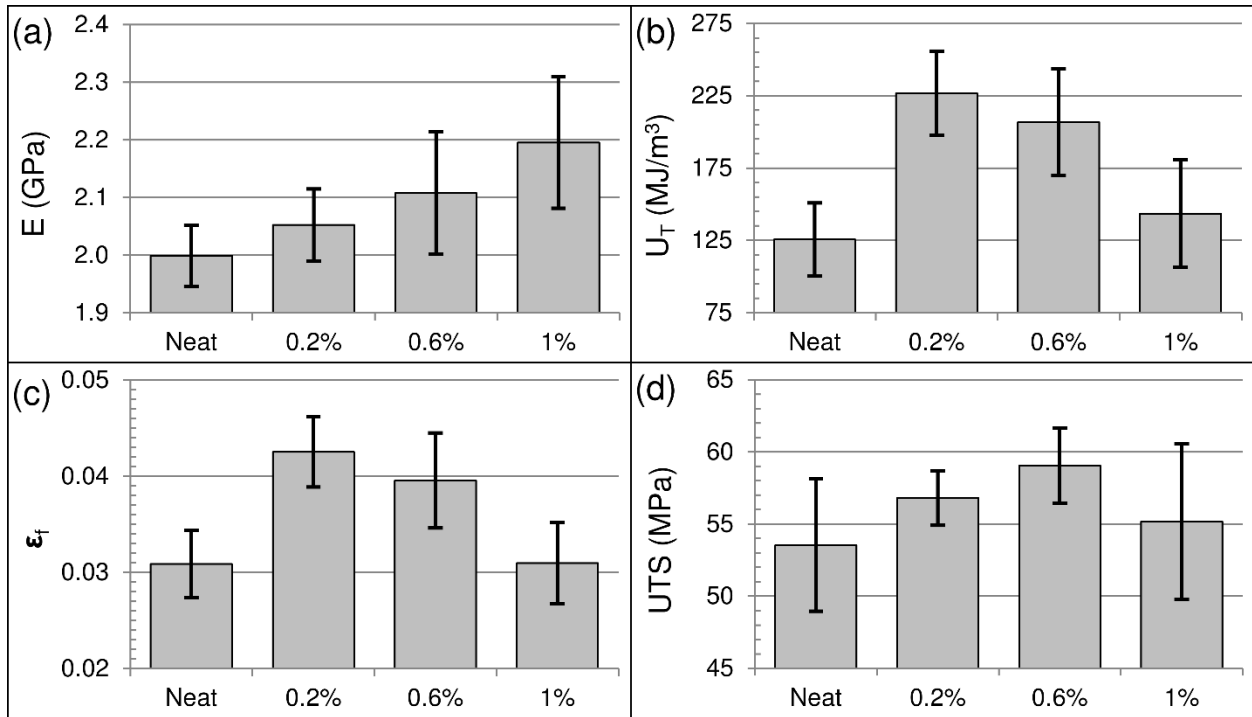
Figure 52. Average values with 95% confidence interval for: (a) elastic modulus, (b) fracture toughness, (c) strain at failure, (d) ultimate tensile strength.

4.3.2. DMA Properties

4.3.2.1. Thermal dependency

The DMA thermal sweep tests performed with constant displacement amplitude indicated a constant loss factor, $\tan(\delta)$, with respect to temperature when temperature is within 30-50 ˚C as illustrated by Figure 53. Preliminary tests (not shown here) indicated the constant range extended to at least 10 ˚C. The thermally independent region indicates that results obtained at room

temperature, 25-30 ˚C, will be comparable because this range is significantly below 50 ˚C where the material properties becomes thermally dependent.
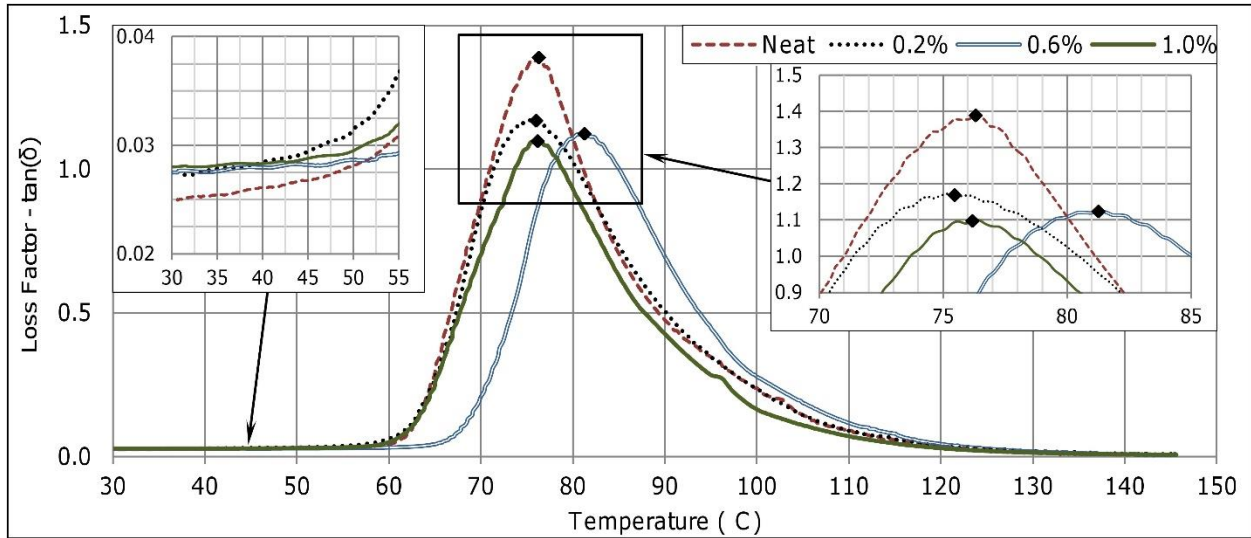
Figure 53. Loss factor (tan δ) vs. temperature of a representative sample for each material. The marked points indicate loss factor peaks used to determine T_g.

The glass transition temperature, T_g, of the sample materials is obtained from the peak of the loss factor versus temperature curve [83, 84]. Of the samples tested, the T_g peaks for each material set were consistently in a 0.5 ˚C range with a peak loss factor variation less than 5%. Overall, the addition of the MWCNTs showed a negligible effect on T_g, with the neat, 0.2 wt.% and 1 wt.% materials all having a transition temperature of approximately 76 ˚C, except the 0.6 wt.% material which yielded a T_g five degrees higher at 81 ˚C. All of the 0.6 wt.% samples where from the same batch and provided near identical thermal dependency curves. The thermal dependency curves for the 0.2 wt.% samples included one outlier with a T_g of approximately 85 °C. All of the other samples tested for the neat, 0.2 wt.%, and 1 wt.% materials had a T_g of approximately 76 ˚C. The most likely explanation for the increased transition temperature of the 0.6 wt.% set would be a slight increase in epoxy cross linking, perhaps due to a variation in environmental conditions during curing or storage [108]. Repetition of the experiment set with

96

samples made in multiple batches would minimize the effect of such variables. Being that the

thermal sweep was a destructive test, it was performed after all of the other testing was

completed. Overall the change in cross linking would have to be small though, as the other

properties of the sample set were not shifted away from the group as evidenced by the previously

discussed quasi-static test results. This is further supported as the single 0.2 wt.% thermal

transition outlier sample did not show as an outlier in any of the other DMA testing it was

included in.

Figure 54 shows the relationship between storage modulus and temperature across the

complete test range. Storage modulus was affected by temperature below 50 °C. All of the

materials had lost approximately 10% of their storage modulus at 55 ˚C, and all but the 0.6 wt.%

had material lost 90% at 70 ˚C. The 0.6 wt.% set lost 90% of its storage modulus at 75 ˚C,

shifted 5 ˚C higher than the others as was its peak loss factor.
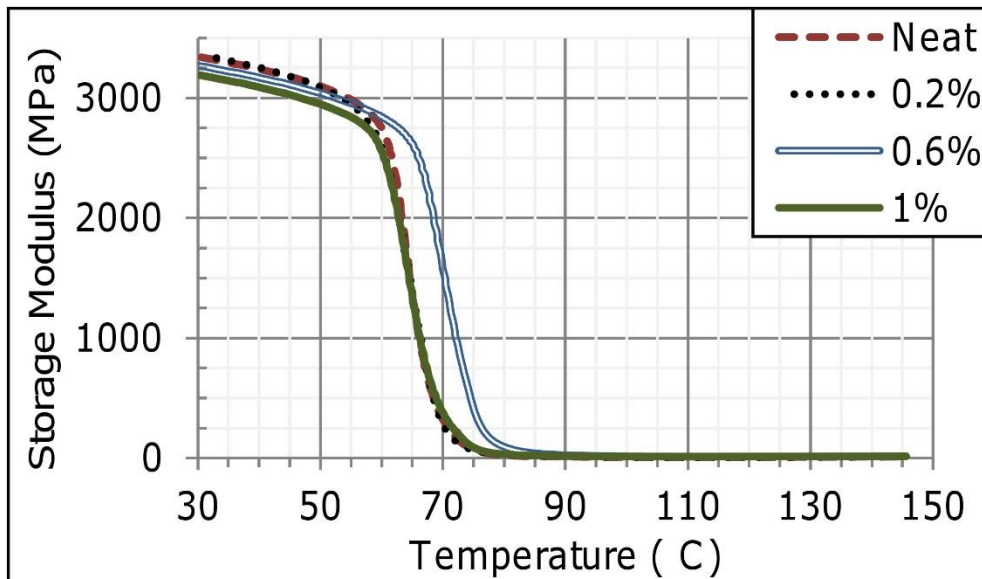
Figure 54. Storage modulus vs. temperature for the representative samples of each material.

4.3.2.2. Damping properties

Figure 55 shows the resulting loss modulus versus the stress amplitude. The neat samples showed the lowest loss modulus at both tested frequencies. Addition of MWCNT reinforcement to the epoxy produced a general increase in loss modulus, with the 1 wt.% MWCNT composite exhibiting the highest loss modulus for a given stress at either frequency. At 7.5 Hz, the 1 wt.% MWCNT composite yielded a 10-12% increase over the neat epoxy, and a 15-20% increase at 50 Hz. Both of the intermediate reinforcement levels also show an increase relative to the neat epoxy; however, the 0.2 wt.% set generally outperformed the 0.6 wt.% set by a small margin, roughly 3-4% relative to the neat epoxy. This percentage change due to MWCNT addition is likely affected by a number of factors including decreases in MWCNT aspect ratio [14] during fabrication, particle dispersion, and the reduced surface area to weight ratio of multi-walled versus single or double walled CNTs [45].
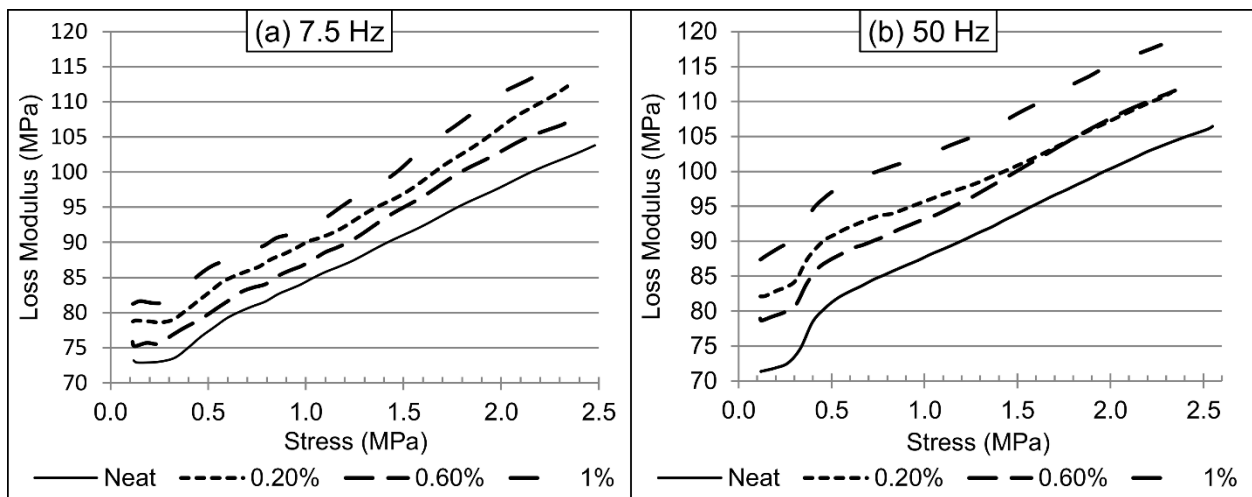
Figure 55. Loss modulus vs. stress at: (a) 7.5 Hz and (b) 50 Hz.

In the 7.5 Hz tests, the samples demonstrated a constant loss modulus at low stress amplitudes, followed by an increasing region starting around 0.3 MPa. The rate of increase then dropped off slightly past the 0.6 MPa stress level. For the 50 Hz stress ramp, the samples

98

demonstrated an approximately constant increase in loss modulus relative to peak vibrational stress except for a section of faster increase between 0.3 and 0.5 MPa.

At sufficiently low stresses and strain rates (low frequencies) the CNT-polymer interface is effectively solid, so the two components move as one. Due to variations in the interfacial bonding along a given CNT, from one CNT to the next, and variations in CNT orientation, interfacial slip will not activate uniformly for all interfaces at a given bulk material stress level [71]. Based on this variation, there will be a range between which most of the interfaces will transition from stick to slip mechanics. Since the primary mode of energy dissipation within CNT-polymer composites is theorized to be slip along the composite interface, an increase is expected in the rate of change of the loss modulus within the transitional range. The presence of a change in the stress-loss modulus relationship between 0.3 and 0.5 MPa at both test frequencies fits with the expectation of an activation range for the stick-slip damping mechanism within the composite. However, the neat epoxy response mirrors that of the MWCNT reinforced composites through the specified stress range. This indicates that the observed bump is most likely due to a mechanism within the epoxy itself, rather than activation of the composite interface slip.

4.4. Conclusions

The addition of MWCNTs showed a consistent increase in both quasi-static and damping properties when compared to the base epoxy. The most significant increases were observed in strain at failure and toughness for the 0.2 wt.% and 0.6 wt.% MWCNT composites, yielding improvements of 28-80% over the neat epoxy.

The elastic modulus of the tested materials was found to increase in a near linear manner, R^2 fit of 0.987, with respect to weight the percentage of MWCNT reinforcement in the

99

composite. Statistical analysis of the sample set also indicates the results are reliable with an approximately 5% or less margin of error. For the Halpin-Tsai model, it was found that a reduced MWCNT aspect ratio based on a nanotube length approximately 25% of the prefabrication length would match the experimental elastic moduli. A reduced elastic modulus value for the MWCNTs yielded a similar effect.

The change in loss modulus was found to be proportional to MWCNT content during DMA testing with a maximum increase of 20% for the 1 wt.% composite with respect to neat epoxy at 50 Hz. The improvement was limited by reinforcement dispersion and surface area. Combined with the length reduction supported by the Halpin-Tsai comparisons, a model capable of prediction of CNT-polymer damping would have to take into account nanotube breakage as a result of manufacturing and dispersion processes. The material strain induced by the vibration must be considered as well due to its effect on the stick-slip energy dissipation. The peak strain amplitude of vibration in these tests is relatively low; however, part of the goal of effective damping in a system is to limit strain deformation.

4.5.   Viability of Damping Investigation Through Load Stage Dynamic Testing

4.5.1.   Proof of Concept

The load stage and DMA platforms both provide important data about the properties of a material, some unique and some overlapping. For example, the load stage design is not viable for thermal profiling such as the thermal sweep tests used to determine glass transition temperature of the sample. Conversely, a sample mounted in the DMA will never be viable for imaging with an AFM. Cyclic loading tests for investigation of dynamic material properties, such as damping, are a strength of DMA equipment. Adding dynamic capability to the load stage platform would provide several benefits not available through DMA. The first benefit of the load stage platform

is sample imaging. While AFM imaging is not presently fast enough to image a sample during a

dynamic event and tracking a specific feature for imaging would be extremely difficult, static

imaging at intervals throughout the testing is a viable. Previous research as shown that the

properties of MWCNT reinforced composites change as the number of dynamic cycles

increases [49, 50]. Some before and after images show changes in orientation and

dispersion [72]. Knowing how these changes progressed during the test, as well as observations

under load conditions at intervals throughout the test duration would help understand the

mechanics and the rate of change during a full cycle set. The load stage also offers substantially

higher force for testing (max force: Q800 DMA - 3.6 lb (16 N), load stage - 100 lb). The higher

load allows for higher stress and testing of larger samples. To further investigate these potential

benefits a dynamic control program was prototyped, refined, and run on several samples for

evaluation.

Once a basic cyclic test profile was implemented, it was run on a 1 wt.% MWCNT-epoxy

test sample. Initial investigation showed the test profile generating a triangular displacement

pattern. Force-displacement plots showed a hysteresis loop, though this was much clearer at

higher force-displacement amplitudes. Numeric integration of several cycles of the force-

displacement data was used to calculate the energy loss, enclosed area of the stress-strain loop,

and thus a damping factor for the initial sample. The relationship between these parameters is:

$$2\zeta = tan(\delta) = \frac{D}{2\sigma_0\varepsilon_0} \tag{26}$$

where ζ is the damping ratio, tan(δ) represents the loss factor based on the phase shift (ϕ)

between the stress and strain response in DMA testing, D is the energy dissipated during one

loading cycle, σ_0 is the max stress of the cycle, and ε_0 is the max strain of a cycle. This

formulation assumes that the cyclic load is fully reversing, so the stress and strain of the cycle are centered about zero. Thus, the two in the denominator accounts for a full cycle where the absolute value of the minimum stress/strain equals their maximum values.
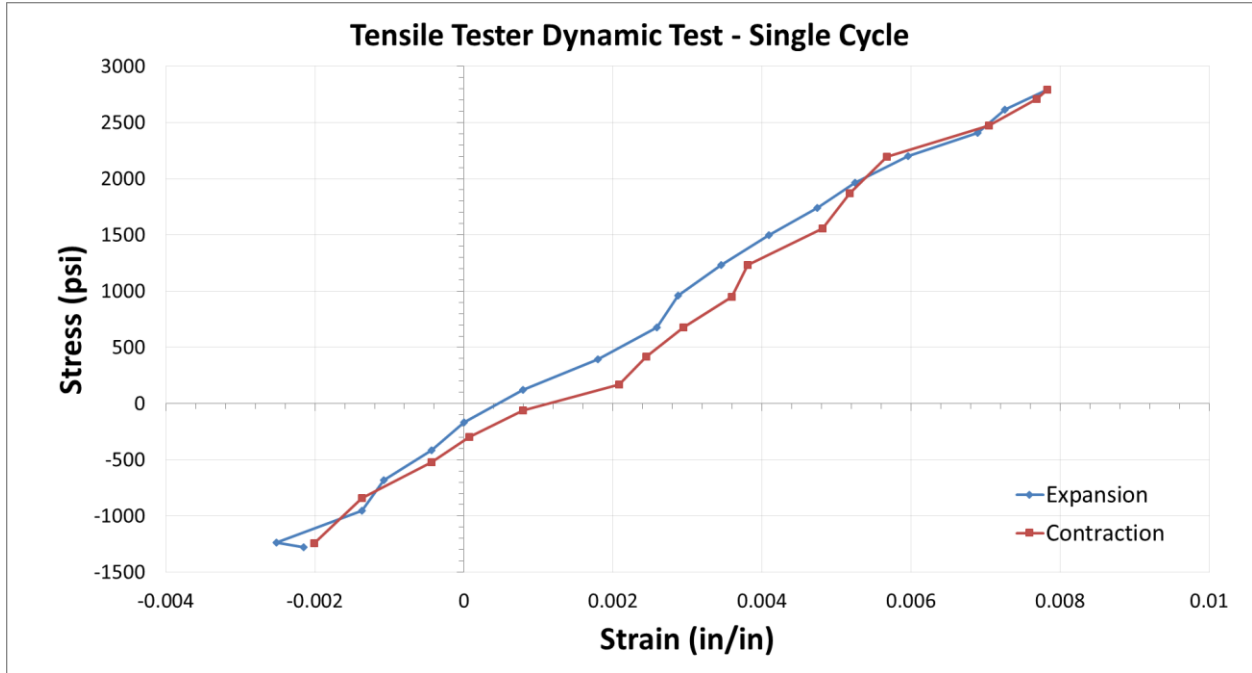
Figure 56. Hysterisis loop visible in 1 wt.% MWCNT reinforced epoxy sample under cyclic loading at 0.75 Hz.

Analysis of the data shown in Figure 56 resulted in a damping ratio (ζ) of 0.0149 based on the formulation of (26). The stress/strain cycle is not fully reversing however, so an alteration of the formula is proposed as:

$$2\zeta = \frac{D}{(\sigma_{max} - \sigma_{min})(\varepsilon_{max} - \varepsilon_{min})} \tag{27}$$

to account for the exact amplitude of the cycle. Based on this alteration the damping ratio increases slightly to 0.0154. The nearest DMA result point for comparison was at 0.8 Hz, a max stress of 500 psi, and a min stress of ~0, resulted in a damping ratio of 0.0123. Given the higher stress of the load stage proof of concept, the higher loss factor is the expected result as more of

the MWCNT-epoxy interfaces reach the required stress to activate the stick-slip energy

dissipation mechanic during the loading cycle. This was deemed sufficient for proof of concept.

4.5.2. Load Stage Dynamic Testing

The next step was to refine the control program. The specific refinement targets were

increase the cycle consistency and accuracy (the same force/displacement amplitude every cycle

and matching the specified target), increase the frequency range, and to improve control over the

cycle parameters (set min/max stress or displacement).

Refining how many data points where collected per control cycle and disabling some

non-vital features in the LabVIEW control program significantly improved the consistency of the

cycle amplitudes and contributed a minor improvement in the max frequency. Setup parameters

for min/max cycle points where added to provide greater control over test conditions. Additional

tuning of the control program did not yield any discernable improvement beyond this point, so

the investigation moved to the testing stage.

Using the refined control program several tests where run for the four MWCNT

reinforcement levels: neat, 0.2, 0.6, and 1 wt.%. The test data was analyzed and is summarized

above in Table 3. The damping ratios from the load stage dynamic testing follow the same

pattern as found during DMA testing and discussed previously in section 4.3.2.2. The neat epoxy

samples demonstrated the lowest damping ratio. From there the damping ratio generally

Table 3. Load stage dynamic test results.

Material Reinforcement %			Neat	0.2%	0.6%	1%
Load Stage testing	Damping ratio		.004	0.012	0.0110	0.0195
	Stress (psi)	max	2089	1125	1325	2350
		min	-1450	-557	-507	-315
	Frequency (Hz.)		.75	1.20	1.17	0.81

increased with MWCNT content. The 0.2 wt.% MWCNT-epoxy tests show an increased

damping ratio of 300%. The increase grows to 488% for the 1 wt.% reinforced material. The

0.6 wt.% group demonstrated an increased damping ratio of 275% versus the neat epoxy, slightly

lower than the 0.2 wt.% samples but consistent with earlier results. As discussed previously, the

likely cause of this deviation in the 0.6 wt.% sample set is uneven reinforcement dispersion.

While the damping ratio followed the same pattern as the DMA results, the demonstrated

increase was much higher. This fits with expectations though, as the damping effect of the slip

portion of the stick-slip mechanic does not activate until sufficient stress is present to overcome

the stick of the ISS. The low force of the DMA testing shows some of the potential benefit by

achieving activation stress for some of the interfaces. Higher frequencies also generate higher

dynamic stress relative to the applied load. This can be seen by the increased difference between

neat and MWCNT reinforced sample loss ratios found during the 50 DMA With the higher force

capability of the load stage, higher stresses are generated. The increased amplitude of the load

cycle more than makes up for the reduced frequency of the load stage testing. The effect being

that more of the stick-slip interfaces are activated resulting in an increased damping ratio for the

test case.

To make the comparison between the load stage and DMA stronger would require higher

frequency capabilities of the load stage. To compensate for the higher force capabilities of the

load stage, a set of reduced cross section samples run in the DMA would provide comparable

stress levels. This is complicated, however, as the smaller samples are more susceptible to

variation caused by defects and other molding inconsistencies, as well as being harder to process,

handle, mount, and inspect without damaging them. An alternate method of molding these

samples would likely be required to prevent damaging the samples during the mold fill, cure, and extraction processes.

Overall these findings indicate the load stage dynamic testing is a viable testing method for damping investigation providing increased loading capabilities versus typical DMA equipment. The ability to perform nanoscale imaging and quasi-static testing at desired intervals further enhances the systems investigative potential in the areas of MWCNT orientation and dispersion changes over time during dynamic testing.

5. CONCLUSIONS AND FUTURE WORK

5.1. Conclusions

In this project a load-stage was designed for use either independently or in conjunction with an AFM. Once the load-stage was operational tensile tests were performed on epoxy samples, both neat and MWCNT reinforced, using quasi-static, dynamic and AFM imaging modes.

The functional evaluation of the load-stage indicates that it is suitable for bulk property analysis. The tests covered here were performed on tensile samples and provided significant data for mechanical characterization. Analysis of the sample data showed property improvement across the board for MWCNT reinforced materials in quasi-static modes. The most significant improvement was seen in the failure strain which increased 28-80%, with the largest gains resulting from the highest reinforcement content. A linear relationship between reinforcement wt.% and elastic modulus was also observed. The maximum elastic modulus increase, 9.8%, was seen in the 1 wt.% MWCNT material. Statistical analysis of the sample sets indicates a margin of error, a 95% confidence interval, ranging from 2.6% to 5.2% for the elastic modulus. This indicates the findings are significant as the correlation of increasing elastic modulus with increasing MWCNT content holds true across the margin of error range.

AFM images captured of *in-situ* samples also yielded valuable observations. Analysis of images taken as the strain increment increased showed the matrix strain, when measured at a sufficient distance from an MWCNT, was comparable to the load-stage bulk strain measurement. The alignment and waviness of an embedded MWCNT also showed effects correlated to the material strain. The fiber was shown to rotate, approximately 1.1° for the example given in Figure 42 (Chapter 3, p77), and straighten as the bulk material strain increased. Image analysis,

both optical and AFM, of notched samples showed the effects of crack propagation differed between reinforced and neat epoxy. Cracks were observed deviating around reinforcing components within the MWCNT samples, compared to the relatively smooth failure surface observed post failure on the neat epoxy specimens. This resulted in significantly slower crack growth within the reinforced samples allowing for *in-situ* AFM imaging, while propagation of the cracks within neat samples were catastrophic once propagation was archived.

The dynamic testing evaluation of the load-stage was found lacking. The overall sampling rate was found to be too slow for anything faster than 1 Hz. This left no direct avenue for comparison of the load-stage dynamic results with DMA as the tests run on the DMA did not produce stable results below approximately 7.5 Hz.

The DMA tests indicated that the damping improvement imparted by the MWCNT content of the epoxy was 20% or less. Additionally, the MWCNT content was found to have no effect on the glass transition temperature of the epoxy.

5.2. Future Work

A more in depth dynamic analysis is the primary goal going forward. Additional DMA testing in a higher deformation mode, such as single or double cantilever bending, should be investigated.

Dynamic comparison of load stage results with the DMA will require a more involved process. The concept was demonstrated with the machine's current state, but higher frequencies are required. Mechanically, the system can create significantly faster cycle times, eventually limited either by the motors torque or maximum RPM capabilities, depending on the cycle amplitude. The challenge is in the controls. As the control program is now, it cannot run fast enough to operate a test above 1 Hz. This leaves three options: rewrite the LabVIEW control

program to minimize execution time, make changes to the electronic hardware and update the LabVIEW program, or build a dedicated electronics solution and program the controls into an embedded microcontroller. Each of these routes has its pros and cons.

A standalone LabVIEW control rewrite is likely the cheapest, even counting labor time. The penalty comes in the maximum performance benefit and skill required. The program rewrite would require someone of moderate or higher skill in LabVIEW. There are methods available which should allow tasks to run in parallel, though they are complex. This would allow data collection, data storage, and control calculations to run simultaneously, albeit on data from different time steps. In the end, however, this route is still limited due to execution time of the slowest process step. The likely result would be a dynamic test peak frequency of 10 Hz with a triangular profile. The data collection would also retain its time variant spacing preventing use of higher quality filters.

The second option would be to offload some of the calculations to hardware components. One option being that in dynamic testing mode the direction and stepping speed be governed by a sine generation function within the microcontroller. The LabVIEW control could then be used to send less frequent updates to the microcontroller's function. This method would allow for a sinusoidal displacement profile which reduces the acceleration (or torque) demands placed upon the motor when attempting to generate a high frequency triangular cycle. The end result will still have the limits of LabVIEW however, leaving it capable of perhaps 20 Hz maximum frequency, though the outcome of this route is the hardest to estimate.

The final option is to build a dedicated system. This is the ideal solution for someone with sufficient electrical engineering skill. By combining the analog to digital conversion, primary data storage, and a microcontroller driven control program, the system should be able to

reach the component limits, such as motor speed/torque, which should be 50+ Hz. The

limitations to this method become user interface and system accessibility, as well as an increased

difficulty in updating the program functionality, though interpreting a complex LabVIEW

program is likely a comparable difficulty. There would also likely be the greatest additional cost

associated with this option due to electronic components, board layout and assembly time, and a

complete control program rewrite. An interface with LabVIEW or a PC in general would

alleviate the user interface difficulties, though it would add further to the time requirement of the

project.

REFERENCES

[1] Eleftheriou, E., 2012, "Nanopositioning for storage applications," Annual Reviews in Control, 36(2), pp. 244-254.

[2] Thompson, S. M., 2008, "The Discovery, Development and Future of GMR: The Nobel Prize 2007," Journal of Physics D-Applied Physics, 41(9), p. 20.

[3] Bez, R., Camerlenghi, E., Modelli, A., and Visconti, A., 2003, "Introduction to Flash memory," Proceedings of the Ieee, 91(4), pp. 489-502.

[4] Mayo, J. S., 1981, "The Power Of Microelectronics," Technology Review, 83, pp. 46-54.

[5] Zhang, J. H., Wang, L. F., and Zhao, Y. F., 2012, "Fabrication of novel hindered phenol/phenol resin/nitrile butadiene rubber hybrids and their long-period damping properties," Polymer Composites, 33(12), pp. 2125-2133.

[6] Sun, L. Y., Gibson, R. F., Gordaninejad, F., and Suhr, J., 2009, "Energy Absorption Capability Of Nanocomposites: A Review," Composites Science and Technology, 69(14), pp. 2392-2409.

[7] Yap, F. F., Harmoko, H., Liu, M., and Vahdati, N., 2007, "Modeling of Hard Disk Drives for Shock and Vibration Analysis - Consideration of Nonlinearities and Discontinuities," Nonlinear Dynamics, 50(3), pp. 717-731.

[8] Brackbill, C. R., Lesieutre, G. A., Smith, E. C., and Ruhl, L. E., 2000, "Characterization and Modeling of the Low Strain Amplitude and frequency dependent behavior of elastomeric Damper Materials," Journal of the American Helicopter Society, 45(1), pp. 34-42.

[9] Lindler, J. E., Choi, Y. T., and Wereley, N. M., 2003, "Double Adjustable Shock Absorbers Utilizing Electrorheological and Magnetorheological Fluids," International Journal of Vehicle Design, 33(1-3), pp. 189-206.

[10] Eason, R. P., Sun, C., Dick, A. J., and Nagarajaiah, S., 2013, "Attenuation of a Linear Oscillator Using a Nonlinear and a Semi-Active Tuned Mass Damper in Series," Journal of Sound and Vibration, 332(1), pp. 154-166.

[11] Ghaemmaghami, A., Kianoush, R., and Yuan, X. X., 2013, "Numerical Modeling of Dynamic Behavior of Annular Tuned Liquid Dampers for Applications in Wind Towers," Computer-Aided Civil and Infrastructure Engineering, 28(1), pp. 38-51.

[12] Tait, M. J., Isyumov, N., and Damatty, A. A. E., 2008, "Performance of Tuned Liquid Dampers," Journal of Engineering Mechanics, 134(5), pp. 417-427.

[13] Kosmatka, J., and Liguore, S., 1993, "Review of Methods for Analyzing Constrained-Layer Damped Structures," Journal of Aerospace Engineering, 6(3), pp. 268-283.

[14] Suhr, J., and Koratkar, N. A., 2008, "Energy dissipation in carbon nanotube composites: a review," Journal of Materials Science, 43(13), pp. 4370-4382.

[15] Suhr, J., Koratkar, N., Keblinski, P., and Ajayan, P., 2005, "Viscoelasticity in carbon nanotube composites," Nature Materials, 4(2), pp. 134-137.

[16] Ajayan, P. M., Suhr, J., and Koratkar, N., 2006, "Utilizing interfaces in carbon nanotube reinforced polymer composites for structural damping," Journal of Materials Science, 41(23), pp. 7824-7829.

[17] Zhou, X., Shin, E., Wang, K. W., and Bakis, C. E., 2004, "Interfacial damping characteristics of carbon nanotube-based composites," Composites Science and Technology, 64(15), pp. 2425-2437.

110

[18] Koratkar, N. A., Suhr, J., Joshi, A., Kane, R. S., Schadler, L. S., Ajayan, P. M., and Bartolucci, S., 2005, "Characterizing energy dissipation in single-walled carbon nanotube polycarbonate composites," Applied Physics Letters, 87(6).

[19] Koratkar, N., Wei, B. Q., and Ajayan, P. M., 2002, "Carbon nanotube films for damping applications," Advanced Materials, 14(13-14), pp. 997-+.

[20] Rajoria, H., and Jalili, N., 2005, "Passive vibration damping enhancement using carbon nanotube-epoxy reinforced composites," Composites Science and Technology, 65(14), pp. 2079-2093.

[21] Arockiasamy, A., Park, S. J., and German, R. M., 2010, "Viscoelastic behaviour of porous sintered steels compact," Powder Metallurgy, 53(2), pp. 107-111.

[22] Mamedov, A. A., Kotov, N. A., Prato, M., Guldi, D. M., Wicksted, J. P., and Hirsch, A., 2002, "Molecular design of strong single-wall carbon nanotube/polyelectrolyte multilayer composites," Nature Materials, 1(3), pp. 190-194.

[23] Odegard, G. M., Gates, T. S., Wise, K. E., Park, C., and Siochi, E. J., 2003, "Constitutive modeling of nanotube-reinforced polymer composites," Composites Science and Technology, 63(11), pp. 1671-1687.

[24] Andrews, R., and Weisenberger, M. C., 2004, "Carbon nanotube polymer composites," Current Opinion in Solid State & Materials Science, 8(1), pp. 31-37.

[25] Baskaran, R., Sarojadevi, M., and Vijayakumar, C. T., 2011, "Unsaturated polyester nanocomposites filled with nano alumina," Journal of Materials Science, 46(14), pp. 4864-4871.

[26] Bledzki, A. K., and Gassan, J., 1999, "Composites reinforced with cellulose based fibres," Progress in Polymer Science, 24(2), pp. 221-274.

[27] Li, X. D., Gao, H. S., Scrivens, W. A., Fei, D. L., Xu, X. Y., Sutton, M. A., Reynolds, A. P., and Myrick, M. L., 2004, "Nanomechanical characterization of single-walled carbon nanotube reinforced epoxy composites," Nanotechnology, 15(11), pp. 1416-1423.

[28] Strong, L. E., and West, J. L., 2011, "Thermally responsive polymer-nanoparticle composites for biomedical applications," Wiley Interdisciplinary Reviews-Nanomedicine and Nanobiotechnology, 3(3), pp. 307-317.

[29] Li, L., Zou, H. K., Shao, L., Wang, G. Q., and Chen, J. F., 2005, "Study on mechanical property of epoxy composite filled with nano-sized calcium carbonate particles," Journal of Materials Science, 40(5), pp. 1297-1299.

[30] Dostal, C. A., and Reinhart, T. J., 1987, Engineered materials handbook, ASM International.

[31] Davis, J. R., 1998, Metals handbook, ASM International.

[32] Ruoff, R. S., Qian, D., and Liu, W. K., 2003, "Mechanical properties of carbon nanotubes: theoretical predictions and experimental measurements," Comptes Rendus Physique, 4(9), pp. 993-1008.

[33] Li, C. Y., and Chou, T. W., 2003, "Elastic moduli of multi-walled carbon nanotubes and the effect of van der Waals forces," Composites Science and Technology, 63(11), pp. 1517-1524.

[34] Lu, J. P., 1997, "Elastic properties of carbon nanotubes and nanoropes," Physical Review Letters, 79(7), pp. 1297-1300.

[35] Coleman, J. N., Khan, U., Blau, W. J., and Gun'ko, Y. K., 2006, "Small but strong: A review of the mechanical properties of carbon nanotube-polymer composites," Carbon, 44(9), pp. 1624-1652.

[36] Cheap Tubes, Inc., 2012, "www.cheaptubesinc.com/MWNTs.htm."

[37] Sumita, M., Tsukumo, Y., Miyasaka, K., and Ishikawa, K., 1983, "Tensile Yield Stress of Polypropylene Composites Filled With Ultrafine Particles," Journal of Materials Science, 18(6), pp. 1758-1764.

[38] Li, X. D., Gao, H. S., Scrivens, W. A., Fei, D. L., Xu, X. Y., Sutton, M. A., Reynolds, A. P., and Myrick, M. L., 2007, "Reinforcing mechanisms of Single-Walled Carbon Nanotube-Reinforced Polymer Composites," Journal of Nanoscience and Nanotechnology, 7(7), pp. 2309-2317.

[39] Kis, A., Jensen, K., Aloni, S., Mickelson, W., and Zettl, A., 2006, "Interlayer Forces and Ultralow Sliding Friction in Multiwalled Carbon Nanotubes," Physical Review Letters, 97(2), p. 4.

[40] Huhtala, M., Krasheninnikov, A. V., Aittoniemi, J., Stuart, S. J., Nordlund, K., and Kaski, K., 2004, "Improved Mechanical Load Transfer Between Shells of Multiwalled Carbon Nanotubes," Physical Review B, 70(4), p. 8.

[41] Shen, G. A., Namilae, S., and Chandra, N., 2006, "Load transfer issues in the tensile and compressive behavior of multiwall carbon nanotubes," Materials Science and Engineering a-Structural Materials Properties Microstructure and Processing, 429(1-2), pp. 66-73.

[42] Bhushan, B., and Ling, X., 2008, "Adhesion and friction between individual carbon nanotubes measured using force-versus-distance curves in atomic force microscopy," Physical Review B, 78(4), p. 9.

[43] Cumings, J., and Zettl, A., 2000, "Low-Friction Nanoscale Linear Bearing Realized From Multiwall Carbon Nanotubes," Science, 289(5479), pp. 602-604.

[44] Lourie, O., Cox, D. M., and Wagner, H. D., 1998, "Buckling and collapse of embedded carbon nanotubes," Physical Review Letters, 81(8), pp. 1638-1641.

[45] Cadek, M., Coleman, J. N., Ryan, K. P., Nicolosi, V., Bister, G., Fonseca, A., Nagy, J. B., Szostak, K., Beguin, F., and Blau, W. J., 2004, "Reinforcement of polymers with carbon nanotubes: The role of nanotube surface area," Nano Letters, 4(2), pp. 353-356.

[46] Hilding, J., Grulke, E. A., Zhang, Z. G., and Lockwood, F., 2003, "Dispersion of carbon nanotubes in liquids," Journal of Dispersion Science and Technology, 24(1), pp. 1-41.

[47] Huang, Y. Y., and Terentjev, E. M., 2012, "Dispersion of Carbon Nanotubes: Mixing, Sonication, Stabilization, and Composite Properties," Polymers, 4(1), pp. 275-295.

[48] Socher, R., Krause, B., Müller, M. T., Boldt, R., and Pötschke, P., 2012, "The influence of matrix viscosity on MWCNT dispersion and electrical properties in different thermoplastic nanocomposites," Polymer, 53(2), pp. 495–504.

[49] Coleman, J. N., Cadek, M., Blake, R., Nicolosi, V., Ryan, K. P., Belton, C., Fonseca, A., Nagy, J. B., Gun'ko, Y. K., and Blau, W. J., 2004, "High-Performance Nanotube-Reinforced Plastics: Understanding the Mechanism of Strength Increase," Advanced Functional Materials, 14(8), pp. 791-798.

[50] Vaisman, L., Wagner, H. D., and Marom, G., 2006, "The role of surfactants in dispersion of carbon nanotubes," Advances in Colloid and Interface Science, 128, pp. 37-46.

[51] Suhr, J., Schadler, L., and Koratkar, N., 2005, "Characterization of mechanical properties of multiwalled nanotube polymer composites."

[52] Krause, B., Bolcit, R., and Potschke, P., 2011, "A method for determination of length distributions of multiwalled carbon nanotubes before and after melt processing," Carbon, 49(4), pp. 1243-1247.

[53] Pagani, G., Green, M. J., Poulin, P., and Pasquali, M., 2012, "Competing mechanisms and scaling laws for carbon nanotube scission by ultrasonication," Proceedings of the National Academy of Sciences, 109(29), pp. 11599-11604.

[54] Cadek, M., Coleman, J. N., Barron, V., Hedicke, K., and Blau, W. J., 2002, "Morphological and mechanical properties of carbon-nanotube-reinforced semicrystalline and amorphous polymer composites," Applied Physics Letters, 81(27), pp. 5123-5125.

[55] Cox, H. L., 1952, "The Elasticity and Strength of Paper and Other Fibrous Materials," British Journal of Applied Physics, 3(MAR), pp. 72-79.

[56] Kelly, A., and Tyson, W. R., 1965, "Tensile Properties of Fibre-Reinforced Metals - Copper/Tungsten and Copper/Molybdenum," Journal of the Mechanics and Physics of Solids, 13(6), pp. 329-&.

[57] Halpin, J. C., 1969, "Stiffness and Expansion Estimates for Oriented Short Fiber Composites," Journal of Composite Materials, 3, pp. 732-&.

[58] Halpin, J. C., and Kardos, J. L., 1976, "Halpin-Tsai Equations - Review," Polymer Engineering and Science, 16(5), pp. 344-352.

[59] Tandon, G. P., and Weng, G. J., 1984, "The Effect of Aspect Ratio of Inclusions on the Elastic Properties of Unidirectionally Aligned Composites," Polymer Composites, 5(4), pp. 327-333.

[60] Mori, T., and Tanaka, K., 1973, "Average Stress in Matrix and Average Elastic Energy of Materials With Misfitting Inclusions," Acta Metallurgica, 21(5), pp. 571-574.

[61] Eshelby, J. D., 1957, "The Determination of the Elastic Field of an Ellipsoidal Inclusion, and Related Problems," Proceedings of the Royal Society of London. Series A. Mathematical and Physical Sciences, 241(1226), pp. 376-396.

[62] Hui, C. Y., and Shia, D., 1998, "Simple formulae for the effective moduli of unidirectional aligned composites," Polymer Engineering and Science, 38(5), pp. 774-782.

[63] Hill, R., 1963, "Elastic Properties Of Reinforced Solids - Some Theoretical Principles," Journal of the Mechanics and Physics of Solids, 11(5), pp. 357-372.

[64] Hill, R., 1964, "Theory Of Mechanical Properties Of Fibre-Strengthened Materials .1. Elastic Behaviour," Journal of the Mechanics and Physics of Solids, 12(4), pp. 199-212.

[65] Hermans, J., "The elastic properties of Fiber Reinforced Materials when the Fibers are Aligned," Proc. Proc. K. Ned. Akad. Wet. B, pp. 1-9.

[66] Kerner, E. H., 1956, "The Elastic and Thermo-Elastic Properties of Composite Media," Proceedings of the Physical Society of London Section B, 69(8), pp. 808-813.

[67] Leininger, W., Wang, X. N., Tangpong, X. W., and McNea, M., 2012, "Nanoscale Structural and Mechanical Characterization of MWCNT-Reinforced Polymer Composites," Journal of Engineering Materials and Technology-Transactions of the Asme, 134(2).

[68] Liu, A. L., Huang, J. H., Wang, K. W., and Bakis, C. E., 2006, "Effects of interfacial friction on the damping characteristics of composites containing randomly oriented carbon nanotube ropes," Journal of Intelligent Material Systems and Structures, 17(3), pp. 217-229.

[69] Lin, R. M., and Lu, C., 2010, "Modeling of Interfacial Friction Damping of Carbon Nanotube-Based Nanocomposites," Mechanical Systems and Signal Processing, 24(8), pp. 2996-3012.

[70] Savvas, D. N., Papadopoulos, V., and Papadrakakis, M., 2012, "The Effect of Interfacial Shear Strength on Damping Behavior of Carbon Nanotube Reinforced Composites," International Journal of Solids and Structures, 49(26), pp. 3823-3837.

[71] Holscher, H., Schwarz, U. D., Zworner, O., and Wiesendanger, R., 1998, "Consequences of the Stick-Slip Movement for the Scanning Force Microscopy Imaging of Graphite," Physical Review B, 57(4), pp. 2477-2481.

[72] Chen, J. K., Huang, Z. P., and Zhu, J., 2007, "Size Effect of Particles on the Damage Dissipation in Nanocomposites," Composites Science and Technology, 67(14), pp. 2990-2996.

[73] Bhushan, B., Ling, X., Jungen, A., and Hierold, C., 2008, "Adhesion and friction of a multiwalled carbon nanotube sliding against single-walled carbon nanotube," Physical Review B, 77(16), p. 12.

[74] Xu, M., Futaba, D. N., Yamada, T., Yumura, M., and Hata, K., 2010, "Carbon Nanotubes with Temperature-Invariant Viscoelasticity from-196 degrees to 1000 degrees C," Science, 330(6009), pp. 1364-1368.

[75] Cook, R. D., 2007, Concepts and Applications of Finite Element Analysis, 4TH ED, Wiley India Pvt. Limited.

[76] Chang, T. E., Jensen, L. R., Kisliuk, A., Pipes, R. B., Pyrz, R., and Sokolov, A. P., 2005, "Microscopic Mechanism of Reinforcement in Single-Wall Carbon Nanotube/Polypropylene Nanocomposite," Polymer, 46(2), pp. 439-444.

[77] Murayama, T., 1978, Dynamic Mechanical Analysis of Polymeric Material, Elsevier Scientific Publishing Company.

[78] Groves, S. E., Sanchez, R. J., Lyon, R. E., and Brown, A. E., 1993, "High Strain Rate Effects for Composite Materials," ASTM Special Technical Publication, 1206, pp. 162-162.

[79] Naik, N. K., Yernamma, P., Thoram, N. M., Gadipatri, R., and Kavala, V. R., 2010, "High Strain Rate Tensile Behavior of Woven Fabric E-Glass/Epoxy Composite," Polymer Testing, 29(1), pp. 14-22.

[80] Itabashi, M., and Kawata, K., 2000, "Carbon Content Effect on High-Strain-Rate Tensile Properties for Carbon Steels," International Journal of Impact Engineering, 24(2), pp. 117-131.

[81] Suresh, S., 1998, Fatigue of Materials, Cambridge University Press.

[82] Inman, D. J., 2006, Vibration with Control, Wiley.

[83] Wang, Y. B., Huang, Z. X., Du, M., and Zhang, L. M., 2007, "Experimental Investigation on the Damping Behaviors of Epoxies with Different Epoxy Value," Polymer-Plastics Technology and Engineering, 46(10-12), pp. 973-977.

[84] Shi, X. Y., Bi, W. N., and Zhao, S. G., 2012, "DMA analysis of the damping of ethylene-vinyl acetate/acrylonitrile butadiene rubber blends," Journal of Applied Polymer Science, 124(3), pp. 2234-2239.

[85] Lahelin, M., Aaltio, I., Heczko, O., Soderberg, O., Ge, Y., Lofgren, B., Hannula, S. P., and Seppala, J., 2009, "DMA testing of Ni-Mn-Ga/polymer composites," Composites Part a-Applied Science and Manufacturing, 40(2), pp. 125-129.

[86] Raghavan, J., Bartkiewicz, T., Boyko, S., Kupriyanov, M., Rajapakse, N., and Yu, B., 2010, "Damping, Tensile, and Impact Properties of Superelastic Shape Memory Alloy (SMA) Fiber-Reinforced Polymer Composites," Composites Part B-Engineering, 41(3), pp. 214-222.

[87] Hu, X. S., He, X. D., Zheng, M. Y., and Wu, K., 2010, "Effect of small tensile deformation on damping capacities of Mg-1%Al alloy," Transactions of Nonferrous Metals Society of China, 20, pp. S444-S447.

[88] Sung, Y. T., Kum, C. K., Lee, H. S., Byon, N. S., Yoon, H. G., and Kim, W. N., 2005, "Dynamic mechanical and morphological properties of polycarbonate/multi-walled carbon nanotube composites," Polymer, 46(15), pp. 5656-5661.

[89] Bashaiwoldu, A. B., Podczeck, F., and Newton, J. M., 2004, "Application of dynamic mechanical analysis (DMA) to determine the mechanical properties of pellets," International Journal of Pharmaceutics, 269(2), pp. 329-342.

[90] Cooper, C. A., Cohen, S. R., Barber, A. H., and Wagner, H. D., 2002, "Detachment of nanotubes from a polymer matrix," Applied Physics Letters, 81(20), pp. 3873-3875.

[91] Salandrino, A., and Engheta, N., 2006, "Far-field subdiffraction optical microscopy using metamaterial crystals: Theory and simulations," Physical Review B, 74(7), p. 075103.

[92] Ayatollahi, M. R., Shadlou, S., and Shokrieh, M. M., 2011, "Fracture toughness of epoxy/multi-walled carbon nanotube nano-composites under bending and shear loading conditions," Materials & Design, 32(4), pp. 2115-2124.

[93] Lee, T., 2011, "Improvement of viscoelastic damping in nickel aluminum bronze by indium-tin," Metals and Materials International, 17(3), pp. 425-430.

[94] Zhao, P., Wang, K., Yang, H., Zhang, Q., Du, R. N., and Fu, Q., 2007, "Excellent tensile ductility in highly oriented injection-molded bars of polypropylene/carbon nanotubes composites," Polymer, 48(19), pp. 5688-5695.

[95] Hillenbrand, R., 2004, "Towards phonon photonics: scattering-type near-field optical microscopy reveals phonon-enhanced near-field interaction," Ultramicroscopy, 100(3-4), pp. 421-427.

[96] Cadek, M., Murphy, R., McCarthy, B., Drury, A., Lahr, B., Barklie, R. C., Panhuis, M., Coleman, J. N., and Blau, W. J., 2002, "Optimisation of the arc-discharge production of multi-walled carbon nanotubes," Carbon, 40(6), pp. 923-928.

[97] Giessibl, F. J., 2003, "Advances in atomic force microscopy," Reviews of modern physics, 75(3), p. 949.

[98] Hibbeler, R. C., 1997, Mechanics of Materials, Prentice Hall, New Jersey.

[99] Chasiotis, I., and Knauss, W. G., 2002, "A new microtensile tester for the study of MEMS materials with the aid of atomic force microscopy," Experimental Mechanics, 42(1), pp. 51-57.

[100] Lang, U., Suss, T., Wojtas, N., and Dual, J., 2010, "Novel Method for Analyzing Crack Growth in Polymeric Microtensile Specimens by In Situ Atomic Force Microscopy," Experimental Mechanics, 50(4), pp. 463-472.

[101] Jin, Q. H., Li, T., Zhou, P., and Wang, Y. L., 2009, "Mechanical Researches on Young's Modulus of SCS Nanostructures," Journal of Nanomaterials, p. 6.

[102] Gianola, D. S., and Eberl, C., 2009, "Micro- and nanoscale tensile testing of materials," Jom, 61(3), pp. 24-35.

[103] Bamberg, E., Grippo, C. P., Wanakamol, P., Slocum, A. H., Boyce, M. C., and Thomas, E. L., 2006, "A tensile test device for in situ atomic force microscope mechanical testing," Precision Engineering-Journal of the International Societies for Precision Engineering and Nanotechnology, 30(1), pp. 71-84.

[104] THK, "General Catalog: Ball Screw, 2017, "https://tech.thk.com/en/products/pdf_download.php?file=511E_15_BallScrew.pdf.

[105] Hu, H., Onyebueke, L., and Abatan, A., 2010, "Characterizing and Modeling Mechanical Properties of Nanocomposites-Review and Evaluation," Journal of Minerals and Materials Characterization and Engineering, 9(4), p. 45.

[106] Putz, K. W., Mitchell, C. A., Krishnamoorti, R., and Green, P. F., 2004, "Elastic modulus of single-walled carbon nanotube/poly(methyl methacrylate) nanocomposites," Journal of Polymer Science Part B-Polymer Physics, 42(12), pp. 2286-2293.

[107] Leininger, W., Wang, X., and Tangpong, X., 2014, "Effects of MWCNT reinforcement on quasi-static and dynamic tensile properties of epoxy," Journal of Composite Materials, 48(17), pp. 2049-2057.

[108] Frigione, M., Lettieri, M., and Mecchi, A. M., 2006, "Environmental effects on epoxy adhesives employed for restoration of historical buildings," Journal of Materials in Civil Engineering, 18(5), pp. 715-722.

APPENDIX A. LSM250 SERIES LOAD CELL
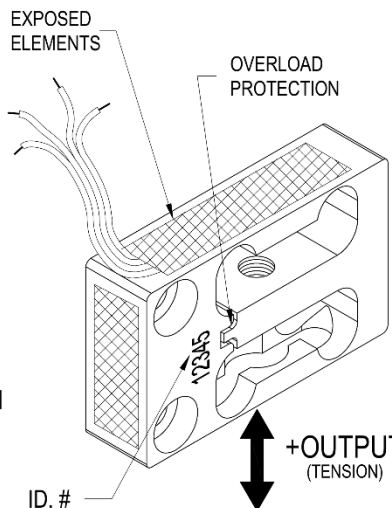
FUTEK MODEL LSM250 (L2331)

Drawing Number: FI1039
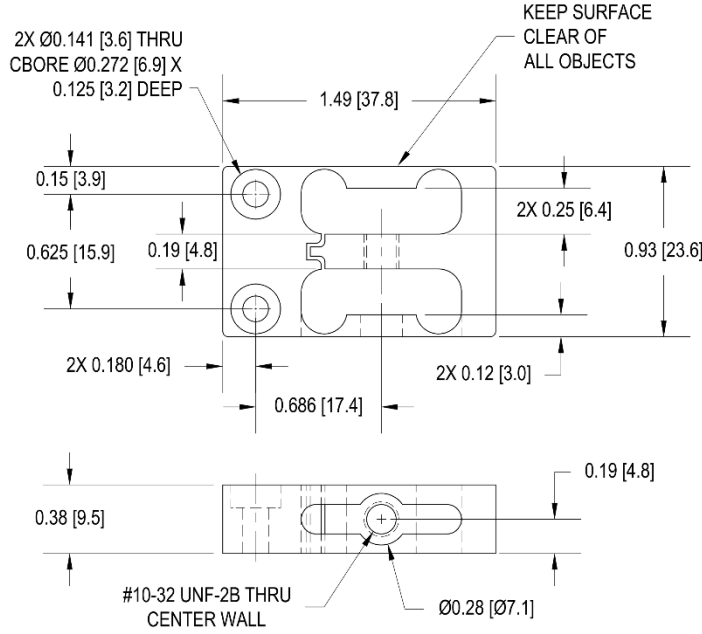
INCH [mm] | **R.O.= Rated Output**

WIRING CODE (WC2)			
+Excitation	-Excitation	+Signal	-Signal
GREEN	BLACK	WHITE	RED

COLOR CODE FOR THIS SENSOR IS NOT FUTEK STANDARD

PARALLELOGRAM LOAD CELL WITH OVERLOAD PROTECTION (OEM TYPE)

EXPOSED ELEMENTS

OVERLOAD PROTECTION

2X Ø0.141 [3.6] THRU
CBORE Ø0.272 [6.9] X
0.125 [3.2] DEEP

KEEP SURFACE CLEAR OF ALL OBJECTS

1.49 [37.8]

0.15 [3.9]

2X 0.25 [6.4]

0.625 [15.9]   0.19 [4.8]

0.93 [23.6]

2X 0.180 [4.6]

2X 0.12 [3.0]

0.686 [17.4]

+OUTPUT (TENSION)

ID. #

0.19 [4.8]

0.38 [9.5]

#10-32 UNF-2B THRU CENTER WALL

Ø0.28 [Ø7.1]

NOTE:

** HANDLE WITH CARE, ALWAYS MONITOR OUTPUT DURING INSTALLATION. **

	CAPACITY	
Stock #	lb	N
FSH00011	1/4	1.1
FSH00012	1/2	2.2
FSH00013	1	4.5

FOR HIGHER CAPACITIES REFER TO MODEL LSM300 (L2330)

SPECIFICATIONS:

RATED OUTPUT	2 mV/V nom.
SAFE OVERLOAD	50 lb
ZERO BALANCE	±3% of R.O.
EXCITATION (VDC OR VAC)	18 MAX
BRIDGE RESISTANCE	1000 Ω nom.
NONLINEARITY	±0.05% of R.O. IMPROVED ACCURACY
HYSTERESIS	±0.05% of R.O. } AVAILABLE CONTACT
NONREPEATABILITY	±0.05% of R.O. } FACTORY
CREEP	±0.05% of LOAD.
TEMP. SHIFT ZERO	±0.005% of R.O./°F [0.01% of R.O./°C]
TEMP. SHIFT SPAN	±0.005% of LOAD/°F [0.01% of LOAD/°C]
COMPENSATED TEMP.	60 to 160 °F [15 to 72 °C]
OPERATING TEMP.	-60 to 200 °F [-50 to 93 °C]
WEIGHT	1 oz [28 g]
MATERIAL	ALUMINUM
NOM. DEFLECTION	0.004 [0.10]
CABLE: #29 AWG, 4 Conductor, Spiral Teflon Cable 6 [0.3 m] Long	
ACCESSORIES AND RELATED INSTRUMENTS AVAILABLE	
CALIBRATION (STD)	2 pt. TENSION; 150KΩ SHUNT CAL. VALUE
CALIBRATION (AVAILABLE)	2 pt. COMPRESSION
CALIBRATION TEST EXCITATION	10 VDC

FUTEK
ADVANCED SENSOR TECHNOLOGY, INC.

10 THOMAS
IRVINE, CA 92618 USA
1-800-23-FUTEK (38835)

INTERNET:
http://www.futek.com

APPENDIX B. LSM300 SERIES LOAD CELL

FUTEK MODEL LSM300 (L2330)

Drawing Number: FI1038-B

INCH [mm] | R.O.= Rated Output

WIRING CODE (WC2)

+Excitation	-Excitation	+Signal	-Signal
GREEN	BLACK	WHITE	RED

COLOR CODE FOR THIS SENSOR IS NOT FUTEK STANDARD

PARALLELOGRAM LOAD CELL W/ OVERLOAD PROTECTION (OEM TYPE)

VALOX COVER

+OUTPUT (TENSION)

OVERLOAD PROTECTION

ID. #

2X ØA THRU. CBORE ØB X 0.22 [5.6] DEEP

1.8 [45.7]
1.74 [44.2]
0.37 [9.5]
0.22 [5.7]
0.25 [6.4]
1.27 [32.3]
1.4 [34.8]
0.686 [17.4]
0.32 [8.2]
0.625 [15.9]
0.25 [6.3]

Ø0.281 [Ø7.1] THRU BOTH WALLS THREAD UNF-2B THRU CENTER

0.50 [12.7]

FOR LOWER CAPACITIES REFER TO MODEL LSM250 (L2331)

Stock #	CAPACITY lb	CAPACITY N	THREAD	A	B	NOM. DEFLECTION	SAFE OVERLOAD (lb)
FSH00001	2.2	9.8				-	250
FSH00002	5	22.2					250
FSH00004	10	44.5					250
FSH00005	25	111	#10-32	0.14 [3.6]	0.25 [6.4]	-	250
FSH00006	50	222					250
FSH00007	100	445					250
FSH00008	200	890					400*
FSH00009	500	2224	1/4-28	0.21 [5.3]	0.34 [5.6]	-	1000*

* IF ADDITIONAL PINS ARE USED

SPECIFICATIONS:

RATED OUTPUT	2 mV/V nom.
SAFE OVERLOAD (2.2 - 100 lb)	250 lb
SAFE OVERLOAD (200 - 500 lb)	200% of R.O.
ZERO BALANCE	±3% of R.O.
EXCITATION (VDC OR VAC)	18 MAX
BRIDGE RESISTANCE	1000 Ω nom.
NONLINEARITY (2.2 - 100 lb)	±0.02% of R.O.
HYSTERESIS (2.2 - 100 lb)	±0.02% of R.O.
NONLINEARITY (200 - 500 lb)	±0.06% of R.O.
HYSTERESIS (200 - 500 lb)	±0.06% of R.O.
NONREPEATABILITY	±0.02% of R.O.
CREEP	±0.025% of LOAD.
TEMP. SHIFT ZERO	±0.005% of R.O./°F [0.01% of R.O./°C]
TEMP. SHIFT SPAN	±0.005% of LOAD/°F [0.01% of LOAD/°C]
COMPENSATED TEMP.	60 to 160°F [15 to 72°C]
OPERATING TEMP.	-60 to 200°F [-50 to 93°C]
WEIGHT	1 to 3 oz [28 to 85 g]
MATERIAL	ALUMINUM (2.2 to 100 lb) 17-4PH S.S. (200-500 lb)
CABLE: #29 AWG, 4 Conductor, Spiral Teflon Cable 6 in. [152.4 mm] Long	
ACCESSORIES AND RELATED INSTRUMENTS AVAILABLE	
CALIBRATION (STD)	2 pt. TENSION; 150KΩ SHUNT CAL. VALUE
CALIBRATION (AVAILABLE)	2 pt. COMPRESSION
CALIBRATION TEST EXCITATION	10 VDC

ADDITIONAL HOLE LOCATIONS 200-500 lb ONLY

Ø 0.095 [2.41] / 0.093 [2.36]

0.237 [6.02] TYP.

YXXXXX

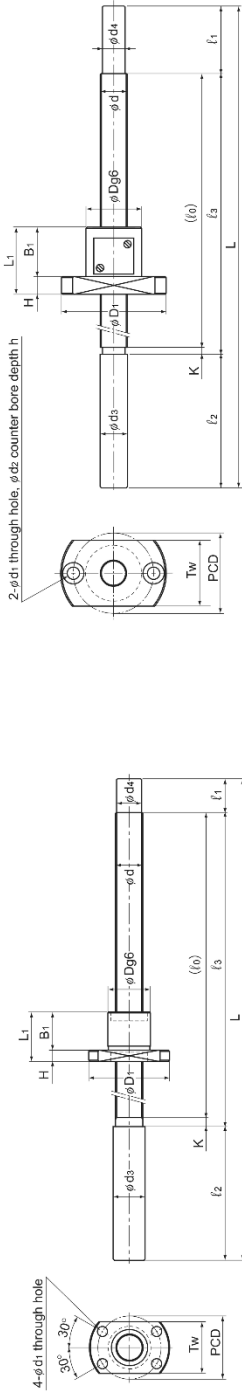## FUTEK

ADVANCED SENSOR TECHNOLOGY, INC.

This drawing is submitted solely for the information and exclusive use of the original addressee. It is not to be divulged in whole or in part, by any firm or individual without written permission from FUTEK

10 THOMAS
IRVINE, CA 92618 USA
1-800-23-FUTEK (38835)

INTERNET:
http://www.futek.com

APPENDIX C. THK LEAD SCREW MECHANICAL DRAWINGS

Unfinished Shaft Ends

Ball Screw

Model MDK

Model MBF

2-øNd1 through hole, ød2 counter bore depth h

Unit: mm

Model No.	Ball screw specifications							Nut				Dimensions							Standard-stock symbol	Screw shaft dimensions									Nut mass	Shaft mass
	Screw shaft outer diameter	Lead	Ball center-to-center diameter	Thread minor diameter	No. of loaded circuits	Basic load rating		Outer diameter	Flange diameter	Overall length	H	B₁	PCD	d₁	d₂	h	Tw		Overall length								K		
	d	Ph	dp	dc	Rows × turns	Ca kN	C₀a kN	D	D₁	L₁									L	ℓ₀	ℓ₁	ℓ₂	ℓ₃	d₃	d₄			kg	kg/m
MDK 0801-3	8	1	8.2	7.3	3×1	0.64	1.4	13	26	15	4	11	20	3.4	—	—	17	A	130	67	15	45	70	10.2	7.3	3	0.02	0.29
																			160	97	15	45	100	10.2	7.3	3	0.02	0.29
																			190	127	15	45	130	10.2	7.3	3	0.02	0.29
																			240	177	15	45	180	10.2	7.3	3	0.02	0.29
MDK 0802-3	8	2	8.3	7	3×1	1.4	2.3	15	28	22	5	17	22	3.4	—	—	19	A	140	76	15	45	80	10.2	7	4	0.04	0.27
																			170	106	15	45	110	10.2	7	4	0.04	0.27
																			200	136	15	45	140	10.2	7	4	0.04	0.27
																			250	186	15	45	190	10.2	7	4	0.04	0.27
MBF 0802-3.7	8	2	8.3	6.4	1×3.7	2.5	4.2	20	40	28	6	22	30	4.5	8	4	24	A	168	85	25	55	88	8.3	6.2	3	0.1	0.19
																			193	110	25	55	113	8.3	6.2	3	0.1	0.19
																			218	135	25	55	138	8.3	6.2	3	0.1	0.19

Note) Model MDK 0801 is not provided with a labyrinth seal.

Model number coding

MBF0802-3.7 RR GT +218L C5 A

- Model number
- Seal symbol (*1)
- Overall screw shaft length (in mm)
- Symbol for clearance in the axial direction (*2)
- Accuracy symbol (*3)
- Symbol for standard-stock type (A: with unfinished shaft ends)

(*1) See A15-162. (*2) See A15-25. (*3) See A15-18.
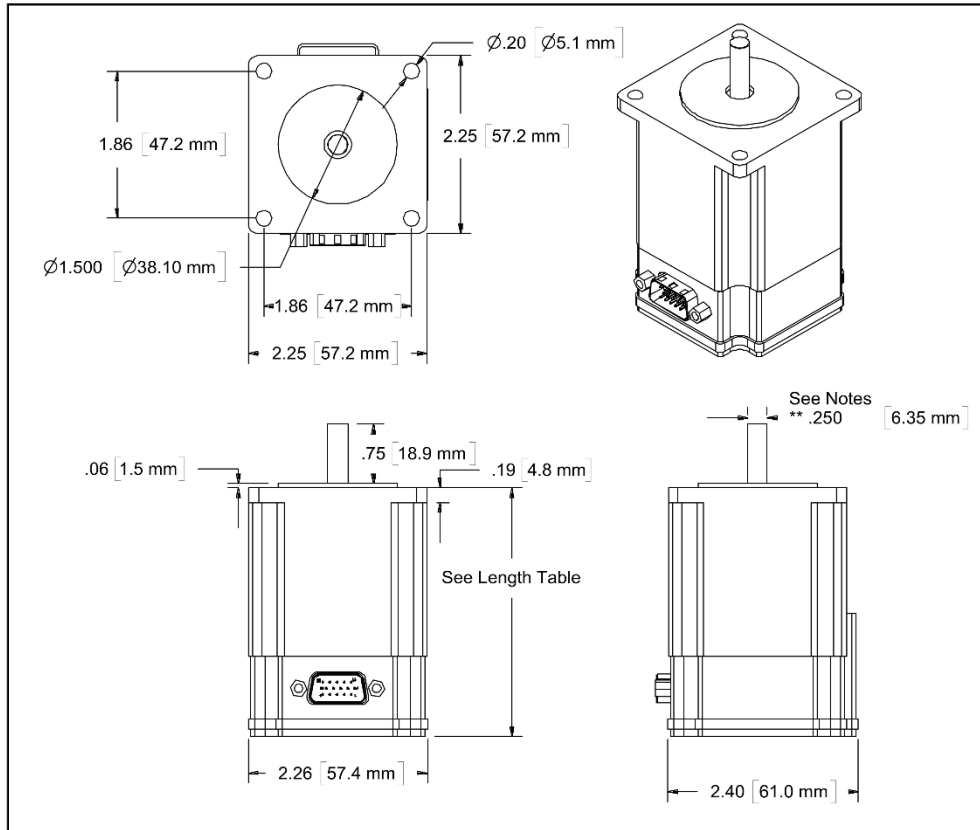
4-øNd1 through hole
30° 30°
Tw
PCD

119

APPENDIX D. MOTOR DATA SHEET

QuickSilver Controls, Inc.

Mechanical Specifications

Standard

Motor Series	Length	Shaft diameter	Notes **
23L-1	2.7 [68 mm]	.250 [6.35 mm]	Shaft has .020 [.5 mm] flat
23K-3	3.2 [81 mm]	.250 [6.35 mm]	Shaft has .020 flat
23L-3	3.2 [81 mm]	.250 [6.35 mm]	Shaft has .020 flat
23H-5	4 [101 mm]	.250 [6.35 mm]	
23H-3	3.2 [80 mm]	.250 [6.35 mm]	* Special order item
23-5	4.1 [103 mm]	.250 [6.35 mm]	* Special order item
23-3	3.2 [80 mm]	.250 [6.35 mm]	* Special order item
23T-7	5.1 [129 mm]	.3125 [7.94 mm]	* Special order item
23H-1	2.7 [68 mm]	.250 [6.35 mm]	* Special order item

APPENDIX E. LINEAR POTENTIOMETER

600 SERIES LINEAR MOTION POSITION TRANSDUCER

#28 AWG TEFLON INSULATED 12 INCHES (305) MIN. LENGTH

#10-32 UNF-2A

.62 (16) DIA

.187 (4.76) DIA

.75 (19)

1.00 (25) RETRACTED

EXTENDED

A

B
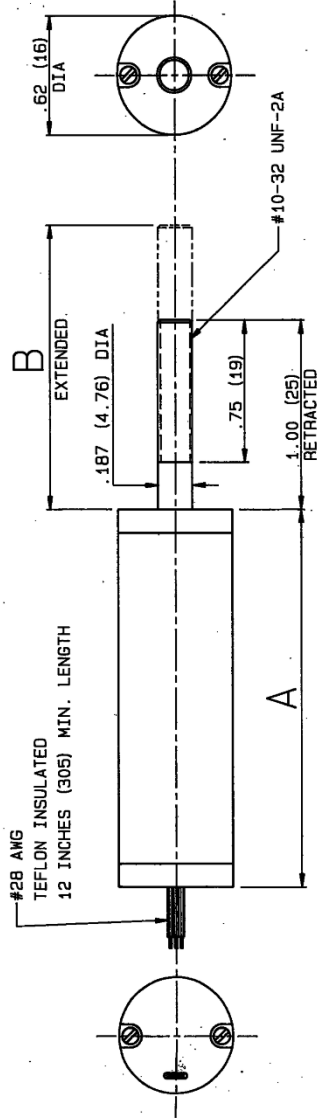
NOTES:
1. DIMENSIONS ARE IN INCHES (mm). TOLERANCE: ±.03 (±.8).
2. AVAILABLE IN DUAL CONFIGURATION.
3. MOST SPECIFICATIONS MAY BE ALTERED TO MEET SPECIFIC REQUIREMENTS.
4. OTHER TRAVELS AVAILABLE.

ELECTRICAL SPECIFICATIONS
ELECTRICAL TRAVEL	SEE TABLE
RESISTANCE RANGE	SEE TABLE
RESISTANCE TOLERANCE	±20%
INDEPENDENT LINEARITY	SEE TABLE
POWER RATING @ 70°C	0.25 WATTS
PER INCH OF ELECTRICAL TRAVEL DERATED TO 0 WATTS @ 125°C	
OUTPUT SMOOTHNESS	0.1%
RESOLUTION	INFINITE
INSULATION RESISTANCE @ 500 VDC	1000 MEGOHMS
DIELECTRIC STRENGTH	500 VRMS
TEMPERATURE RANGE	-55° TO +125°C

MECHANICAL SPECIFICATIONS
MECHANICAL TRAVEL	ELECTRICAL TRAVEL +0.1 INCH MIN.
ACTUATION FORCE	2 OZ. MAX.
REPEATABILITY	WITHIN .0005 IN.
LIFE	10 x 10⁶ CYCLES

SCHEMATIC
BLACK — RED — EXTENDED — WHITE

MODEL	RESISTANCE KΩ	LINEARITY ±%	ELECTRICAL TRAVEL [4]	A DIMENSIONS	B
612	12.0	0.08	12.00 (305)	13.50 (343)	13.10 (333)
610	10.0	0.09	10.00 (254)	11.50 (292)	11.10 (282)
606	6.0	0.12	6.00 (152)	7.50 (190)	7.10 (180)
604	4.0	0.15	4.00 (102)	5.50 (140)	5.10 (129)
603	3.0	0.25	3.00 (76)	4.50 (114)	4.10 (104)
602	2.0	0.35	2.00 (51)	3.50 (89)	3.10 (79)
601	1.0	0.70	1.00 (25)	2.50 (57)	2.10 (53)

DUNCAN electronics, inc.
COSTA MESA, CALIFORNIA
DWG. NAME OUTLINE 600 SERIES
DWG. NO. 600-50
REL. DATE 4-26-88
REV. C
PAGE 1 OF 1